Measurements of b-baryon properties at LHCb

THÈSE N^O 6147 (2014)

PRÉSENTÉE LE 2 MAI 2014
À LA FACULTÉ DES SCIENCES DE BASE
LABORATOIRE DE PHYSIQUE DES HAUTES ÉNERGIES 2
PROGRAMME DOCTORAL EN PHYSIQUE

ÉCOLE POLYTECHNIQUE FÉDÉRALE DE LAUSANNE

POUR L'OBTENTION DU GRADE DE DOCTEUR ÈS SCIENCES

PAR

Raphael MÄRKI

acceptée sur proposition du jury:

Prof. M. Q. Tran, président du jury
Prof. O. Schneider, directeur de thèse
Dr W. Hulsbergen, rapporteur
Dr U. Langenegger, rapporteur
Dr D. Tonelli, rapporteur

EPFL

ÉCOLE POLYTECHNIQUE
FÉDÉRALE DE LAUSANNE

Suisse
2014

To God, who so loved the world that he gave his one and only Son, that whoever believes in him shall not perish but have eternal life.

And we know that in all things God works for the good of those who love him, who have been called according to his purpose.
— The Holy Bible, Romans 8:28

Acknowledgements

Abstract

The LHCb experiment located at the Large Hadron Collider at CERN collected its first data from proton-proton collisions between December 2009 and December 2012.

Based on data recorded in 2010, several software alignments of the LHCb tracking stations are performed. The procedure includes vertex and mass constraints from the $D^0 \to K^+\pi^-$ decay. A precision of 15 μm is achieved and the alignment constants were used for high-precision measurements at LHCb with 2010 data. In addition the results of the alignments helped to improve the understanding of the procedure.

Exploiting the data set recorded during the year 2011, the masses of the weakly-decaying Λ_b^0, Ξ_b^- and Ω_b^- baryons are measured:

$$
\begin{aligned}
M(\Lambda_b^0) &= 5619.53 \pm 0.13 \text{ (stat)} \pm 0.45 \text{ (syst) } \text{MeV/c}^2, \\
M(\Xi_b^-) &= 5795.8 \pm 0.9 \text{ (stat)} \pm 0.4 \text{ (syst) } \text{MeV/c}^2, \\
M(\Omega_b^-) &= 6046.0 \pm 2.2 \text{ (stat)} \pm 0.5 \text{ (syst) } \text{MeV/c}^2.
\end{aligned}
$$

The first (second) quoted uncertainty is statistical (systematic). These mass measurements are the most precise to date. Furthermore, the Ω_b^- mass measurement allowed to settle the discrepancy between the results of the CDF and D0 experiments, which disagree by more than six standard deviations. The Ω_b^- mass measurement presented here is in agreement with the CDF measurement and in disagreement with the D0 one.

A preliminary search for the neutral Ξ_b^0 baryon is also presented. A statistically significant signal is observed when both data sets from 2011 and 2012 are combined. Using this same data set, the lifetimes of the Ξ_b^- and Ω_b^- baryons are measured:

$$
\begin{aligned}
\tau(\Xi_b^-) &= 1.55^{+0.10}_{-0.09} \text{ (stat)} \pm 0.03 \text{ (syst) ps}, \\
\tau(\Omega_b^-) &= 1.54^{+0.26}_{-0.21} \text{ (stat)} \pm 0.05 \text{ (syst) ps}.
\end{aligned}
$$

These are the most precise lifetime measurements of these b baryons to date. All b-baryon property measurements presented here provide a unique and valuable input for models in quantum chromodynamics at low energies.

Zusammenfassung

Das LHCb Experiment am Grossen Hadronen-Speicherring am CERN hat zwischen Dezember 2009 und Dezember 2012 seine ersten Daten von Proton-Proton Kollisionen aufgenommen.

Mit den im Jahr 2010 aufgezeichneten Daten wurden mehrere Programmausrichtungen der Spurendetektoren durchgeführt. Die Prozedur beinhaltet Vertex- und Massenzwangsbedingungen vom $D^0 \rightarrow K^+ \pi^-$ Zerfall. Als Resultat wurde die damalige Ausrichtungsprozedur verbessert und eine Präzision von 15 μm erreicht. Die erhaltenen Ausrichtungskonstanten wurden für Präzisionsmessungen basierend auf den Datensatz von 2010 verwendet.

Mit den Daten aus 2011 wurden die Massen der durch die schwache Wechselwirkung zerfallenden Λ_b^0, Ξ_b^- und Ω_b^- Baryonen gemessen:

$$
\begin{aligned}
M(\Lambda_b^0) &= 5619.53 \pm 0.13 \text{ (stat)} \pm 0.45 \text{ (syst) MeV/c}^2, \\
M(\Xi_b^-) &= 5795.8 \pm 0.9 \text{ (stat)} \pm 0.4 \text{ (syst) MeV/c}^2, \\
M(\Omega_b^-) &= 6046.0 \pm 2.2 \text{ (stat)} \pm 0.5 \text{ (syst) MeV/c}^2.
\end{aligned}
$$

Dies sind die derzeit genauesten Messungen. Darüber hinaus hat die Messung der Ω_b^- Masse es ermöglicht die experimentale Uneinigkeit von über sechs Standardabweichungen zwischen den Resultaten der CDF und D0 Experimente zu klären. Der hier präsentierte Wert für die Ω_b^- Masse stimmt mit der CDF Messung überein jedoch nicht mit der D0 Messung.

Es wird ebenfalls eine vorläufige Suche nach dem neutralen Ξ_b^0 Baryon vorgestellt. Ein statistisch aussagekräftiges Signal wird beobachtet wenn beide Datensätze von 2011 und 2012 kombiniert werden. Mit diesem kombinierten Datensatz sind auch die Lebensdauern von Ξ_b^- und Ω_b^- gemessen:

$$
\begin{aligned}
\tau(\Xi_b^-) &= 1.55^{+0.10}_{-0.09} \text{ (stat)} \pm 0.03 \text{ (syst) ps}, \\
\tau(\Omega_b^-) &= 1.54^{+0.26}_{-0.21} \text{ (stat)} \pm 0.05 \text{ (syst) ps}.
\end{aligned}
$$

Dies sind derzeit die genausten Lebensdauermessungen dieser b Baryone. Die hier dargelegten Eigenschaften der b baryonen ergeben einen einzigartigen und wertvollen Beitrag für verschieden Modelle der Quantenchromodynamik im Bereich niegriger Energien.

Résumé

L'expérience LHCb située sur le Grand collisionneur de hadrons au CERN a enregistré ses premières données de collisions proton-proton entre décembre 2009 et décembre 2012.

Sur la base des données enregistrées en 2010, plusieurs alignement informatiques du trajectographe de LHCb ont été réalisés. La procédure inclut des contraintes géométriques et cinématiques de la désintégration $D^0 \to K^+\pi^-$. Une précision de 15 μm a été atteinte et les constantes d'alignement ont été utilisées pour des mesures de haute précision à LHCb avec les données 2010. De plus, les résultats de l'alignement ont permis d'améliorer la compréhension de la procédure elle-même.

En exploitant les données enregistrées pendant l'année 2011, les masses des baryons Λ_b^0, Ξ_b^- et Ω_b^- se désintégrant par la force faible ont été mesurées :

$$
\begin{aligned}
M(\Lambda_b^0) &= 5619.53 \pm 0.13 \text{ (stat)} \pm 0.45 \text{ (syst) MeV/c}^2, \\
M(\Xi_b^-) &= 5795.8 \pm 0.9 \text{ (stat)} \pm 0.4 \text{ (syst) MeV/c}^2, \\
M(\Omega_b^-) &= 6046.0 \pm 2.2 \text{ (stat)} \pm 0.5 \text{ (syst) MeV/c}^2.
\end{aligned}
$$

Ces mesures de masse sont les plus précises à ce jour. La mesure de la masse du baryon Ω_b^- a permis de résoudre le désaccord entre les résultats des expériences CDF et de D0 qui diffèrent par plus de 6 déviations standard. La mesure de la masse du baryon Ω_b^- présentée ici est compatible avec la mesure de CDF et incompatible avec celle de D0.

Une recherche préliminaire du baryon neutre Ξ_b^0 est aussi présentée. Un signal statistiquement significatif est observé quand les données de 2011 et 2012 sont combinées. En utilisant ces mêmes données, les temps de vie des baryons Ξ_b^- et Ω_b^- sont mesurés :

$$
\begin{aligned}
\tau(\Xi_b^-) &= 1.55^{+0.10}_{-0.09} \text{ (stat)} \pm 0.03 \text{ (syst) ps}, \\
\tau(\Omega_b^-) &= 1.54^{+0.26}_{-0.21} \text{ (stat)} \pm 0.05 \text{ (syst) ps}.
\end{aligned}
$$

Ce sont les mesures les plus précises de ces temps de vie à ce jour. Toutes les mesures des propriétés des baryons b présentées ici fournissent des ingrédients uniques et pertinents pour une meilleure compréhension des modèles de chromodynamique quantique à basse énergie.

Mots-clés : **LHCb**, **alignement informatique**, **mesures de masse**, **mesures de temps de vie**, **baryons b**

Contents

List of Figures

List of Tables

1 Introduction

1.1 The Standard Model

The currently most accurate theory describing the fundamental interactions and particles is called the Standard Model [11–13]. It includes the strong, weak and electromagnetic sectors but lacks the description of the gravitational force. The Standard Model has 19 parameters, which are to be determined experimentally. The mathematical framework this theory relies on is Quantum Field Theory (QFT) where the whole description can be derived from a Lagrangian. The total Lagrangian of the Standard Model is the sum of the terms describing each sector.

In the Standard Model there are particles that have either an integer spin value called bosons or a half-integer spin value called fermions. The elementary fermions are the quarks and the leptons. The Standard Model states the existence of three generations of quarks and three generations of leptons. Each quark generation contains two different quarks and each lepton generation contains a charged lepton and an associated neutrino. In addition each quark has an associated anti-particle and exists in three colours. The leptons as well have associated anti-particles but no colour. Thus, without counting the spin projections, a total of 36 different quark states and 12 different lepton states exist in the Standard Model.

There are also twelve vector bosons, carrying the fundamental interactions, and one scalar boson [14–16]. The gluons carry the strong force, the γ boson carries the electromagnetic force, and the W and Z bosons carry the weak force. All bosons with the exception of the charged W are their own anti-particles. Gluons carry a linear combination of colour states composed of always one colour and one anti-colour among the three. Thus they can be described with an $SU(3)$ representation giving eight independent colour states. Including the 13 predicted bosons, the total number of elementary particles in the Standard Model is 61, as summarised in Table 1.1. All of these particles have been observed; the latest observation, the Higgs boson, was announced by the ATLAS and CMS experiments at CERN in July 2012 [17, 18].

Table 1.1: Elementary particles in the Standard Model.

Quarks		
up (u)	strange (s)	bottom (b)
down (d)	charm (c)	top (t)

Leptons		
electron (e)	muon (μ)	tau (τ)
electron neutrino (ν_e)	muon neutrino (ν_μ)	tau neutrino (ν_τ)

Bosons			
gluon (g)	photon (γ)	$W^\pm$ and Z^0	Higgs (H)

1.2 Weakly-decaying b baryons

Quarks, bound by the strong force mediated by gluons, form composite particles called hadrons. Hadrons are found to be colourless combinations of two or three quarks, called mesons and baryons respectively. In this thesis, combinations of three quarks among which at least one is a b, the so-called b baryons, are studied. The total number of predicted b-baryon ground states is 16, listed in Table 1.2.

The decay of the b quark can only happen through the weak force since the quark flavour is conserved by the strong and electromagnetic interactions. Hence the typical lifetime of a b hadron is large compared to strong or electromagnetic decays and is of the order of 1.5 ps. The b baryons (and their quark contents) that are studied hereafter are the Λ_b^0 (udb), Ξ_b^- (dsb), Ξ_b^0 (usb) and Ω_b^- (ssb).

1.2.1 b-baryon mass predictions

b hadrons are described at the fundamental level by Quantum Chromodynamics (QCD). The masses of b baryons are predicted by several different theoretical calculations. One approach consists in comparing the calculation of the b baryon mass with the calculation of the corresponding c baryon mass (the b quark being replaced by the c quark). This technique permits to well predict the mass difference between a b baryon and a similar c baryon. Hence the Λ_b^0 mass is computed based on a precise Λ_c^+ mass measurement, the Ξ_b^- mass based on a precise Ξ_c^+ mass measurement, and so on. The calculation itself has been done using the constituent-quark model (CQM) [19] and a model-independent $1/N_c$ expansion [20] where N_c is the number of quark colours. These calculations produce the predictions with the smallest uncertainties. The CQM-based approach produces a more precise prediction, however it relies on the approximation that the virtual gluons and virtual quarks inside the hadron are constituents of one of the quarks composing the hadron.

Table 1.2: b-baryon ground states predicted by the Standard Model. All of them decay weakly, except the Σ_b states which decay strongly to $\Lambda_b^0 \pi$. A bold font indicates that the state has been experimentally confirmed.

Name	Quark content	Isospin	Spin-parity (J^P)
$\boldsymbol{\Lambda_b^0}$	$\boldsymbol{udb}$	**0**	$\mathbf{1/2^+}$
$\boldsymbol{\Sigma_b^-}$	$\boldsymbol{uub}$	**1**	$\mathbf{1/2^+}$
Σ_b^0	udb	1	$1/2^+$
$\boldsymbol{\Sigma_b^+}$	$\boldsymbol{ddb}$	**1**	$\mathbf{1/2^+}$
$\boldsymbol{\Xi_b^0}$	$\boldsymbol{usb}$	**1/2**	$\mathbf{1/2^+}$
$\boldsymbol{\Xi_b^-}$	$\boldsymbol{dsb}$	**1/2**	$\mathbf{1/2^+}$
Ξ_{cb}^+	ucb	1/2	$1/2^+$
Ξ_{cb}^0	dcb	1/2	$1/2^+$
Ξ_{bb}^0	ubb	1/2	$1/2^+$
Ξ_{bb}^-	dbb	1/2	$1/2^+$
$\boldsymbol{\Omega_b^-}$	$\boldsymbol{ssb}$	**0**	$\mathbf{1/2^+}$
Ω_{cb}^0	scb	0	$1/2^+$
Ω_{ccb}^+	ccb	0	$1/2^+$
Ω_{bb}^-	sbb	0	$1/2^+$
Ω_{cbb}^0	cbb	0	$1/2^+$
Ω_{bbb}^-	bbb	0	$3/2^+$

It is also possible to perform a full calculation of the masses without direct comparison with other experimental mass measurements. Using the CQM in a relativistic environment, the so-called relativistic constituent-quark model (RCQM), it is possible to fully compute the masses from scratch [21]. However, until recently, these calculations had only a limited range of validity in the heavy quark sector. In an effort to create a single framework where all baryon masses and reactions can be computed, an Austrian-Korean group developed a more general RCQM [22]. This theory has a universal aspect, however the precision of the predictions is still low.

Another promising model is the heavy quark effective field theory (HQET) where the heavy baryon is approximated by a two-body system of a heavy quark and a light diquark. Based on HQET and using the QCD sum rule approach, it is possible to predict the heavy-baryon mass spectrum [23]. Performing a calculation using the QCD sum rule without the assumption of the HQET [24] one gets a more independent result, yet it is not as powerful in terms of precision.

A fully different approach is lattice QCD based on simulation [25]. Such calculations need a large amount of computing power but provide an independent method as compared to the ones described above. Nevertheless, today's predictions from lattice QCD computation are as precise as the ones obtained from HQET.

Table 1.3: Mass predictions in MeV/c^2 and their uncertainties for Λ_b^0, Ξ_b^-, Ξ_b^0 and Ω_b^- baryons.

Model	Λ_b^0 mass	Ξ_b^- mass	Ξ_b^0 mass	Ω_b^- mass
CQM [19]	Used as input	$5790 - 5800$	5786.7 ± 3.0	6052.1 ± 5.6
$1/N_c$ expansion [20]	Used as input	Used as input	–	6039.1 ± 8.3
RCQM [21]	5622 ± 100	5812 ± 100	–	6065 ± 100
Universal RCQM [22]*	~ 5650	–	–	~ 6050
HQET+QCD sum rule [23]	5637^{+68}_{-56}	5780^{+73}_{-68}	–	6036 ± 81
QCD sum rule [24]	5690 ± 130	–	5750 ± 130	5890 ± 180
Lattice QCD [25]	$5641 \pm 21^{+15}_{-33}$	$5781 \pm 17^{+17}_{-16}$	–	$6006 \pm 10^{+20}_{-19}$

*Only figures are provided in this publication.

The numerical results of the previously presented approaches are summarised in Table 1.3 for the b baryons studied in this thesis.

1.2.2 b-baryon lifetime predictions

Predictions on the lifetimes of weakly-decaying b baryons are more sparse. Indeed, comparing with lifetimes from b mesons or c baryons does not work as well as for mass calculations. The most recent predictions were made more than 10 years ago and until recently most of them could not yet be tested experimentally.

A powerful way to predict b-baryon lifetimes in QCD is to use Heavy Quark Expansion in which an expansion in powers of $\Lambda_{\mathrm{QCD}}/m_b$ is made where Λ_{QCD} is the scale at which QCD becomes non-perturbative and m_b is the b-quark mass. Such a calculation was performed in 1995 [26] but it appeared that the measured Λ_b^0 lifetime was inexplicably shorter than expected. In this publication appeared as well a first prediction of the ratio between the Ξ_b^- and Λ_b^0 lifetimes, the case of the Ω_b^- lifetime being referred to as "seeming too academic for the moment".

Taking again advantage of the Heavy Quark Expansion framework and using the bag model and the non-relativistic quark model, heavy hadron lifetimes were computed again two years later [27] but the problem with the Λ_b^0 lifetime persisted. However, for the first time two predictions on the values of the Ξ_b^- and Ω_b^- lifetimes were calculated and so far, given the current experimental uncertainties, even these first predictions could not be significantly probed.

A new approach using the HQET attempted to solve the Λ_b^0 lifetime discrepancy [28]. In this last publication the authors give a prediction on the lifetime ratio $\tau(\Xi_b^-)$ over $\tau(B^0)$ and point out the importance of a precise Ω_b^- lifetime measurement to select the best among competing models. Comparing the mentioned theoretical prediction, there is also a disagreement concerning the hierarchy of the lifetimes of the weakly-decaying b baryons.

Table 1.4: Lifetime predictions in ps and their uncertainties for Ξ_b^- and Ω_b^- baryons.

Model	Ξ_b^- lifetime	Ω_b^- lifetime
Heavy Quark Expansion [26]*	≈ 1.57	−
Heavy Quark Expansion + non-relativistic bag model [27]	≈ 1.20	≈ 1.01
HQET [28]*	−	1.67 ± 0.09

*Only ratios are provided in these publications, hence they are combined with the appropriate world averages [1] to obtain the lifetime predictions.

Table 1.4 gives a summary of the theoretical predictions for the lifetimes of the Ξ_b^- and Ω_b^- baryons. It can be seen that the lifetime hierarchy is not the same in all predictions.

1.2.3 Experimental b-baryon spectroscopy results

The first observation of a bottom baryon, through the decay $\Lambda_b^0 \to J/\psi\, \Lambda$, was published by the UA1 experiment at the SPS at CERN in 1991 [29]. The first Λ_b^0 lifetime measurements were also performed at CERN, by the LEP experiments ALEPH and OPAL in 1995 [30, 31], and completed shortly after by Tevatron results and other measurements by LEP experiments.

At around the same time, the LEP experiments DELPHI and ALEPH were the first to measure the average Ξ_b production fraction and lifetime using the partially reconstructed decay b baryon $\to \Xi^- l^- X$ [32,33]. A revised analysis using the complete data set available by DELPHI was published in 2005 [34] and superseded their previous result.

In June 2007, using a large sample of reconstructed $\Lambda_b^0 \to \Lambda_c^+ \pi^-$, CDF observed for the first time the Σ_b and Σ_b^* resonances decaying into $\Lambda_b^0 \pi^\pm$ [35]. Only one month later the Ξ_b^- baryon has been fully reconstructed for the first time by D0 in the decay mode $\Xi_b^- \to J/\psi\, \Xi^-$ [6] and by CDF in the same channel [36]. One year later D0 announced the first observation of the Ω_b^- baryon [9] and CDF performed the same observation as well as new Ξ_b^- measurements shortly after [7]. However, the two Ω_b^- mass measurements performed by CDF and D0 differ at the 6 standard deviations level.

In 2011, CDF published the first Ξ_b^0 observation in the decay mode $\Xi_b^0 \to \Xi_c^+ \pi^-$ and a measurement of the Ξ_b^- mass in the $\Xi_c^0 \pi^-$ decay mode [8]. Another year later three excited b-baryon states were seen for the first time at the LHC: the CMS experiment reported a first observation of the Ξ_b^{*0} baryon [37] and the LHCb experiment observed two excited Λ_b^0 states [38].

More precise mass and width measurements of the Σ_b and Σ_b^* resonances were performed in 2012 by CDF using the full recorded data set [39]. In 2013 the ATLAS collaboration published a Λ_b^0 mass and lifetime measurement of unprecedented accuracy [5]. These results were recently superseded and completed by the current most precise Λ_b^0, Ξ_b^- and Ω_b^- mass and lifetime measurements performed at the LHCb experiment [40, 41] and reported in this thesis.
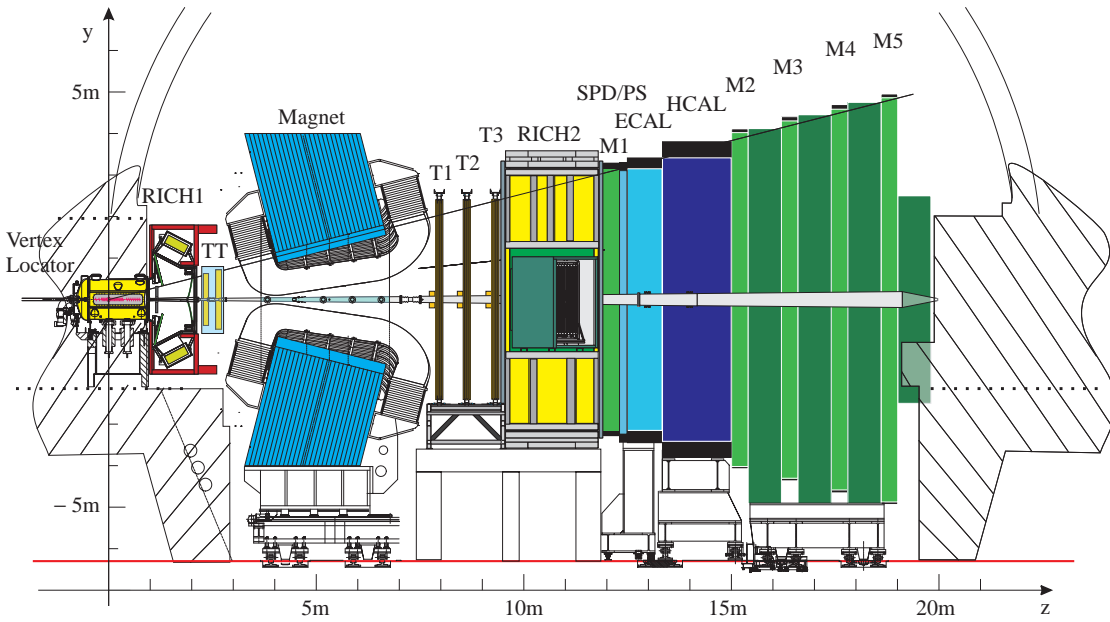
Figure 1.1: The LHCb detector.

In August 2013, new preliminary results from CDF based on the total recorded 9.6 fb^{-1} were shown publicly [42, 43]. However, the precision of these measurements remains below the one achieved at LHCb.

1.3 The LHCb experiment at CERN

The LHCb detector [44] is a single-arm forward spectrometer located on the Large Hadron Collider (LHC) at CERN. It has been designed to study processes in the *c*- and *b*- quark sectors as well as CP violation. The detector, shown in Fig. 1.1, is composed of several layers of sub-detectors each having a specific purpose.

1.3.1 The VErtex LOcator

The *pp* collisions at LHCb happen in the vacuum tank of the VErtex LOcator (VELO) [45] surrounding the interaction point. The VELO is a tracking device based on the silicon microstrip technology. As depicted in Fig. 1.2, its half-circularly shaped sensors are either layers of radial strips (ϕ) or perpendicular ones (R). There are a total of two times 21 layers of R-sensors and as many ϕ-sensors along the beam axis. The particularity of the VELO is that all modules can be moved away from the interaction point. This allows the sensors to be located near the interaction point during data taking and still to be far enough not to be potentially harmed when the beam is unstable during injection, setup and ramping. In the closed position, the
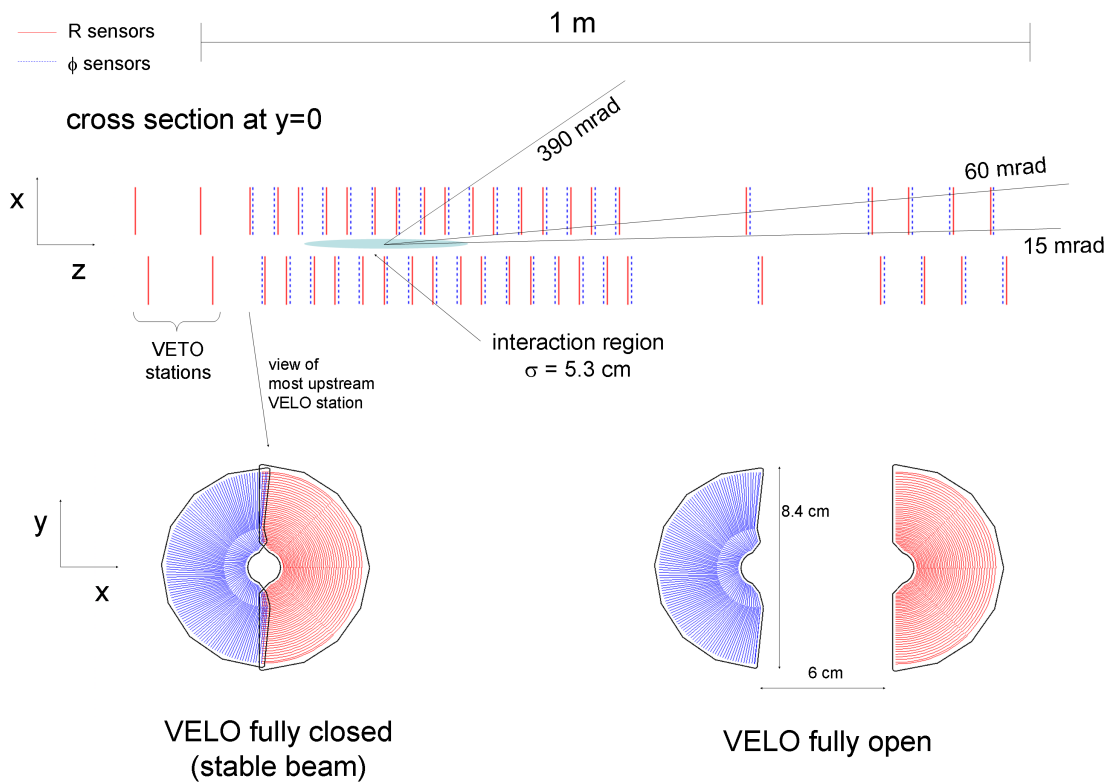
Figure 1.2: The layout of the VELO.

modules are located 7 mm away from the beam line and therefore the first sensor strips are 8.2 mm away from the beam line. This is the shortest distance between the beam and a detector element at any LHC experiment.

1.3.2 The Tracker Turicensis

The Tracker Turicensis (TT) [46] is located between the VELO and the magnet. It consists of two tracking stations, called TTa and TTb, which are each formed of one vertically aligned microstrip plane and one inclined with a stereo angle of 5°. The two stations are separated by a distance of 30 cm. As shown in Fig. 1.3 each of the four planes is divided into two times seven (eight) vertical ladders for TTa (TTb) on the left and right sides and two half-ladders above and below the beam pipe. The long ladders are composed of fourteen microstrip sensors and the half-ladders contain seven sensors each. The colour code in Fig. 1.3 shows how the long ladders are divided into four readout modules of three or four sensors and how the short ladders are divided into three readout modules each of one to four sensors.
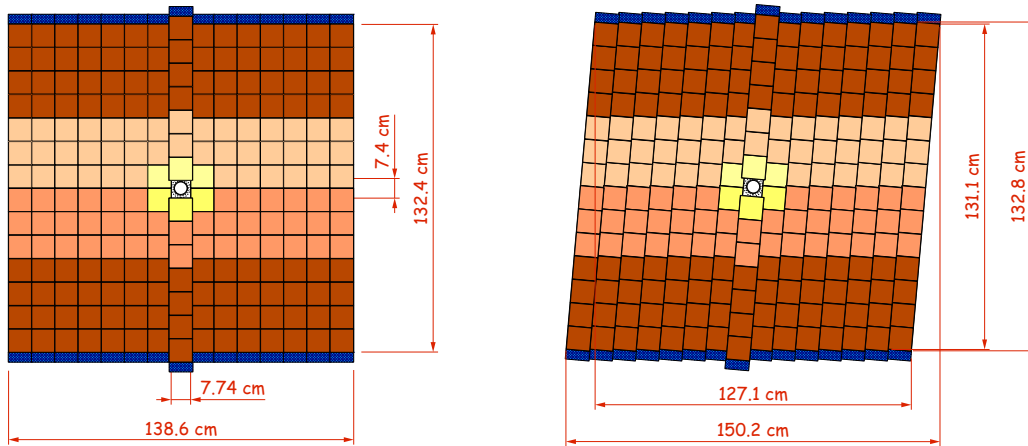
Figure 1.3: The layout of the TTa vertical (left) and stereo (right) detector planes. The colour code shows how the ladders are divided into readout modules. The dark blue ends at the top and the bottom of each ladder represent the structures on which the sensors are mounted.

1.3.3 The magnet

A large dipole magnet of 4 Tm is placed right after the TT, curving the trajectory of charged particles and allowing their momentum to be measured by the tracking system. The magnetic field is vertical and the magnet can be exploited in both polarities. The field direction, up or down, is regularly switched during data taking periods in order to record approximately the same amount of data in the two conditions. Having data with both magnet polarities permits to assess and cancel left-right detector and reconstruction asymmetries. An example described more in detail in Sec. 2.3 is the so-called cowboy and marine effect arising from misalignments and making the momentum scale depend on the kinematics of the measured track.

1.3.4 The Inner Tracker

Downstream of the magnet are three tracking stations, called T-stations or individually T1, T2 and T3. They are divided into two sub-detectors using each a different technology. The central region is, like the TT, a silicon microstrip detector and is called the Inner Tracker (IT) [47].

As shown in Fig. 1.4, each station of the IT is composed of four boxes in a cross-shaped layout. In each box there are four layers of silicon sensors. The first and last layers (called X-layers) have the microstrips vertically oriented whereas the second one (U-layer) and the third one (V-layer) are inclined by a stereo angle of $+5°$ and $-5°$ respectively. Each layer is composed of seven ladders which comprise one (top and bottom boxes) or two (lateral boxes) sensors as depicted in Fig. 1.5.
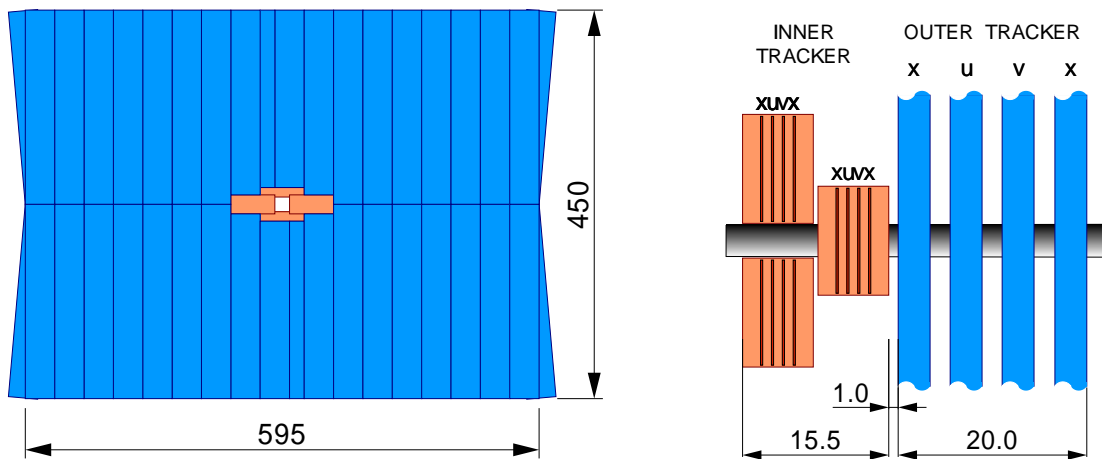
Figure 1.4: Layout sketches of one among the three T-stations. On the left a front view (as seen from the VELO) and on the right a view from above of the central region. The IT is shown in orange and the OT in blue. The dimensions are given in cm.
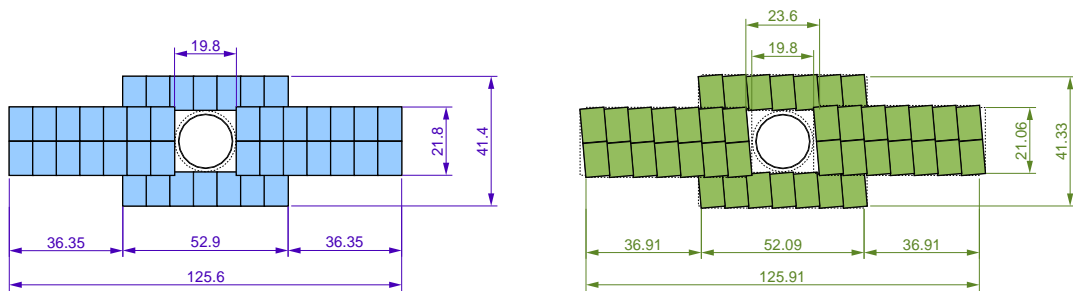
Figure 1.5: The Inner Tracker layout of a vertical layer (left) and a stereo layer (right). Each colour rectangle represents a silicon sensor. The central circle represents the beam pipe. The dimensions are given in cm.

1.3.5   The Outer Tracker

The outer region of the T-stations is composed of straw tubes and is called the Outer Tracker (OT) [48]. As shown in Fig. 1.4, the number of detection planes is the same as for the IT. Each detection plane is formed of two layers of straw tubes where the straw tubes in the first layer are shifted with respect to ones in the second layer by half the width of a straw tube in order to provide maximal coverage. Figure 1.6 shows how each detector plane is subdivided into two times seven long modules of type F and two times four short ones of types S1, S2 and S3. The structures which hold the OT layers are called C-frames due to their shape. One OT C-frame supports two consecutive vertically separated half-layers (for instance the left halves of the X1 and U layers of the first OT station are mounted on one C-frame).
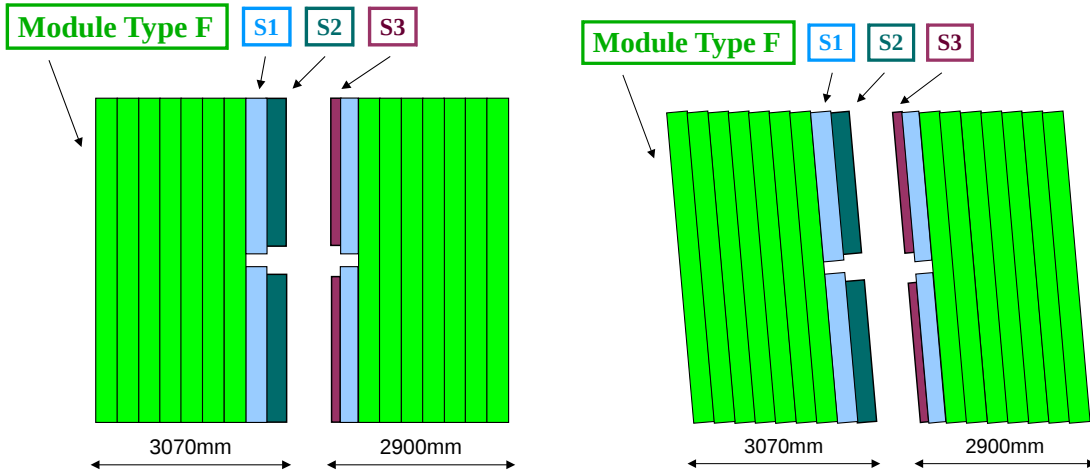
Figure 1.6: The Outer Tracker layout of a vertical layer (left) and a stereo layer (right).

1.3.6 The Ring Imaging Cherenkov detectors

A first Ring Imaging CHerenkov (RICH1) detector is located between the VELO and TT detectors. It uses an aerogel and a gas volume of C_4F_{10} to produce Cherenkov radiation measured by photo-multipliers. The Cherenkov photons are detected with Hybrid Photon Detectors (HPDs) that combine vacuum photo-multiplier tubes with silicon pixels being placed at the anodes. A second RICH detector (RICH2) is situated between the T-stations and the calorimeters. The RICH2 detector uses another gas (CF_4) covering a higher kinematic range to identify charged particles with momenta up to 150 GeV/c. The purpose of these two detectors is to identify charged particles by measuring their velocity that depends on the angle of the Cherenkov light cone. A delta-log-likelihood is calculated from the information of the full RICH system between the probability that the particle is a pion and the probability that the particle is a kaon (PIDK), proton (PIDp), electron (PIDe) etc.

1.3.7 The calorimeters

There are two layers of calorimetry [49]: first the electromagnetic calorimeter (ECAL) and secondly the hadronic one (HCAL). They both use scintillators, interleaved with lead and iron plates for the electromagnetic and hadronic calorimeter, respectively. In addition, there is a Pre-Shower (PS) in front of the electromagnetic calorimeter and a Scintillator Pad Detector (SPD) even further upstream. The PS has a longitudinal segmentation which allows the discrimination of the large background in the electron trigger originating from charged pions. The purpose of the SPD is to discriminate yet another type of background, coming from very high transverse energy π^0 particles, which worsen as well the electron trigger efficiency. The PS represents a total radiation length of 2 X_0 and the main electromagnetic calorimeter of 25 X_0. The HCAL has a thickness of 5.6 interaction lengths. Since the calorimeters are heavily used

in the first stage of the trigger, their design has been tuned to a good compromise between energy resolution and trigger efficiency.

1.3.8 The muon chambers

The last sub-detectors of the LHCb experiment are the muon chambers. The first layer is placed between the RICH2 and the calorimeters, the other four are located downstream of the calorimeters. The used technology is multi-wire proportional chambers except for the central region made of triple-GEM detectors. The last four layers of muon chambers are shielded firstly by the calorimeter system and secondly by interleaved iron shields which have a total thickness of 20 nuclear interaction lengths.

1.3.9 The trigger

In average only around 1% of the pp collisions contain a pair of b quarks of which around 15% fly into the geometrical acceptance of LHCb. Hence a trigger system [50] is deployed to efficiently select such events and limit the amount of data written to disk. The LHCb trigger is composed of three stages namely Level-0 (L0), High Level Trigger 1 (HLT1) and High Level Trigger 2 (HLT2). The first stage is purely analogue and exploits mostly information from the muon chambers and the calorimeters. As shown in Fig. 1.7, this first stage lowers the rate from the initial 40 MHz to 1 MHz. The HLT1 and HLT2 stages reconstruct the events using a 29'000 CPU computer farm and select 5'000 events per second by applying kinematic and PID cuts on the tracks as well as cuts on the reconstructed vertices. Each step is in addition divided into so-called trigger lines which are specific sets of selection criteria on which the trigger may fire.

1.3.10 Data taking at LHCb

First proton-proton (pp) collisions were recorded in December 2009 at the LHC injection centre-of-mass energy of $\sqrt{s} = 900$ GeV. These data led to the very first physics publication of the LHCb collaboration measuring K_s^0 and Λ production [51]. During the year 2010, a total integrated luminosity of 36 pb^{-1} was recorded at $\sqrt{s} = 7$ TeV. In 2011 and 2012 the LHCb experiment recorded 1.0 fb^{-1} at $\sqrt{s} = 7$ TeV and 2.0 fb^{-1} at $\sqrt{s} = 8$ TeV, respectively, resulting in a total integrated luminosity of slightly above 3 fb^{-1}. The average number of pp collisions in the recorded events, called pileup, is approximately 1.8 for 2011 data and 2.1 for 2012 data.

1.3.11 LHCb simulation framework

A dedicated framework called Gauss [52] was developed by the LHCb collaboration to produce simulated samples also referred to as *Monte Carlo* (MC) samples. Gauss includes a generator and a simulation phase. The generator phase mainly relies on the Pythia [53] and EvtGen [54]
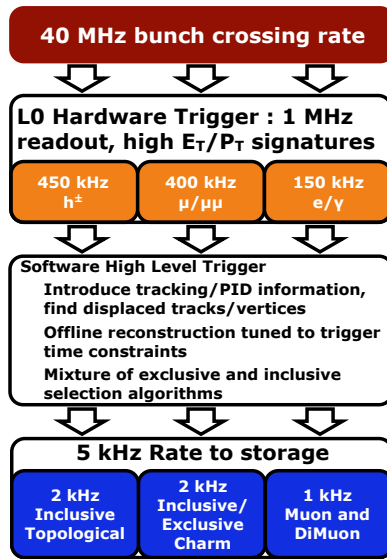
Figure 1.7: Schematic description of the LHCb trigger.

packages and the simulation phase uses Geant4 [55, 56]. The generation phase uses as input so called *decay description files* (also called *DecFiles*) that indicate which is the wanted decay.

For the different physics analyses at LHCb, official MC samples are produced by a dedicated working group. The different sets of conditions reproducing the detector description, data taking, triggering and selection are specifically named. Simulation samples reproducing 2011 data as reconstructed in real time are called *MC11*. The conditions for MC samples reproducing the 2011 and 2012 data reprocessed during early 2013 with the latest versions of the tracking and selection algorithms are called *MC2011* and *MC2012* respectively.

1.3.12   Tracking at LHCb

Most of the information used in the techniques and analysis hereafter comes from the tracking system of the LHCb detector. This system is composed of the three tracking sub-systems which are the VELO, the TT and the T-stations (including the IT and the OT). As a first step, each of these sub-systems performs an independent track segment search. In a second step, VELO segments are both linked to segments from the T-stations in order to form so-called long tracks (L) and to segments from the TT to form so-called downstream tracks (D). If VELO or T-station track segments are not linked to any other sub-detector track segment they remain as they are and are called VELO tracks and T tracks respectively. Hits in the TT located within a certain search window are later attached to long tracks or VELO tracks. Long tracks that have attached TT hits remain called long tracks but VELO tracks that have attached TT hits are called upstream tracks. As a last step, all clones are eliminated by deleting tracks that have too many common hits. A schematic view of the different track type combinations reconstructed
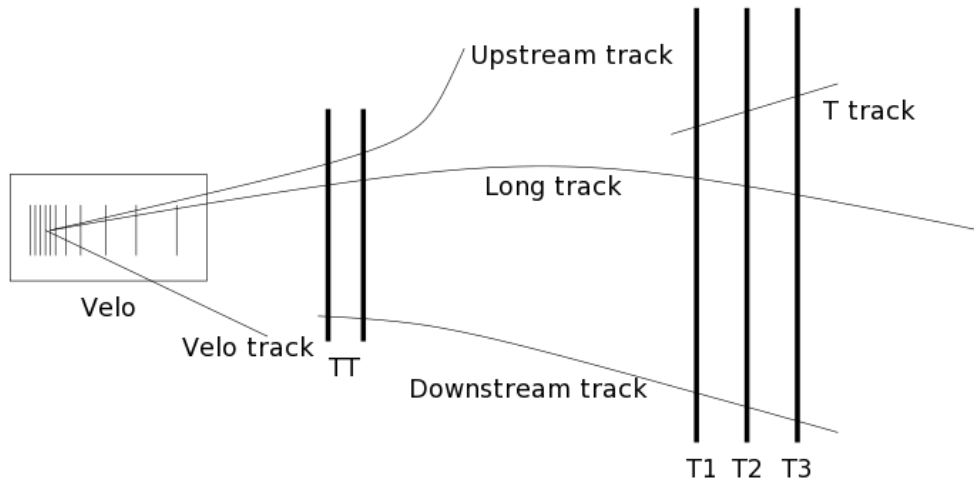
Figure 1.8: Track types reconstructed at LHCb.

at LHCb is shown in Fig. 1.8. Only long or downstream tracks have their momentum measured since they are the only track types which are measured on both sides of the magnet. Therefore only long and downstream tracks are used in most analyses at LHCb.

A quantity that estimates the quality of a reconstructed track is the track χ^2 divided by the number of degrees of freedom (track χ^2/ndf). It is calculated as the sum of the squares of the distances between the track (being an ideal curve) and the track measurements divided by the squares of the measurement uncertainties. It can be computed for a track composed of either one or several track segments. When it is computed for only the VELO track segment, it is usually called the VELO χ^2/ndf of a track. For long tracks, a quantity called match χ^2/ndf is also used to measure how well the VELO and T-station track segments match. It is defined as the total track χ^2/ndf minus the sum of the T-track segment χ^2/ndf and the VELO+TT track segment χ^2/ndf.

1.3.13 Event stripping

After having been fully reconstructed, all events at LHCb undergo the so-called stripping procedure which applies a loose selection and divides the data into around ten different streams. Only the stripped data are directly available to the physicists of the LHCb collaboration. However the raw event data as recorded by the experiment remain stored and are regularly reprocessed with the latest version of the reconstruction algorithms and the stripping selections. Each set of selection cuts applied by the stripping, the so-called stripping lines, targets a specific decay channel or set of decay channels. There are almost 1'000 distinct stripping lines at LHCb.

Data recorded in 2011 was first processed with version 17b of the stripping. During the year 2012, version 20 of the stripping was used to process data collected at that time as well as

reprocess the previously collected data from 2011. Therefore most analyses based on 2011 data use events from *Stripping 17b* and the analyses based on both data sets collected in 2011 and 2012 usually use *Stripping 20*.

1.4 Contributions of this research work

This section describes specifically the contributions I made to the detector exploitation and to various physics analyses. It is organised in chronological order, which coincides by chance with a certain logical order. In addition to the elements below I also served as a teaching assistant for courses in various EPFL and UNIL, bachelor and master programs, I was trained to be a Silicon Tracker piquet and performed several weeks of data-taking shifts, I regularly attended courses of the doctoral cycle *CUSO* and a two-week summer school at Fermilab (USA) and I gave several oral presentations at international conferences on high energy physics [57–64].

First half of 2010: V^0 production measurements

The topic of my master thesis [65] defended in February 2010 was Λ and K_S^0 production measurements at LHCb with the very first data recorded in 2009 at a centre-of-mass energy of $\sqrt{s} = 900$ GeV. During the first few months of my thesis I continued working on this subject by processing recorded and simulated data sets and performing studies on the track type compositions and on primary vertex related effects. My work contributed to the thesis of Matthias Knecht [66] as well as the very first physics publication of the LHCb collaboration [51].

Late 2010 to early 2012: track-based software alignment

In autumn 2010 I started to work on the software alignment described in Chapter 2. A new technique using vertex and mass constraints had just been implemented into the LHCb framework and I started to tune and use it to align the tracking spectrometer of the LHCb detector (TT, IT and OT). The knowledge of the physical position of individual detector elements was improved and a better understanding of the alignment technique itself was gained.

A large fraction of the data recorded in 2010 suffered from a quality issue due to a TT operating temperature change. This was tackled with a set of per-period alignments that I provided using the alignment technique I just got familiar with (see Section 2.4.1). Many 2010 data analyses at LHCb needed these corrected per-period alignments to obtain high precision momentum and mass measurements. Especially the mass measurements of the b hadrons [4] and of the $X(3872)$ meson [67] based on the 2010 data set heavily relied on these alignment constants and the corresponding momentum scale calibration.

Between the end of 2011 and early 2012 an article was written by Wouter Hulsbergen, Olivier Schneider and myself about the developed alignment technique using vertex and mass constraints which has been published in *Nuclear Instruments and Methods A* [68].

Late 2011 to early 2013: Λ_b^0, Ξ_b^- and Ω_b^- mass measurements

Close to the end of 2011 I joined the effort to measure the masses of the Λ_b^0, Ξ_b^- and Ω_b^- baryons using the full data set recorded in 2011. Rapidly I took over many responsibilities including the application of the momentum scale in the fit of the decay chain, the fit of the mass distributions, the estimation of the systematic uncertainties, the evaluation of the statistical significance as well as the production of the Ω_b^- simulated sample. The results of this analysis were published early 2013 in *Physical Review Letters* [40].

In addition I performed a preliminary search for the Ξ_b^0 baryon. First in the decay $\Xi_b^0 \to J/\psi\,\Xi(1530)^0$ using the data collected in 2011. Later I extended the search to the non-resonant part of the decay by looking more generally at $\Xi_b^0 \to J/\psi\,\Xi^-\pi^+$ and I added the data recorded during the year 2012. The outcome of the second search is an observation with statistical significance above five standard deviations. However more time would have been needed to fully carry out and publish this analysis.

Early 2013 to mid 2013: b-hadron lifetime measurements

During the publication process of the b-baryon mass measurements I got involved in a large analysis aiming at the measurement of the lifetimes of several b hadrons. My contribution was to process both real and simulated data samples of $\Lambda_b^0 \to J/\psi\,\Lambda$ and $B^0 \to J/\psi\,K_S^0$ with the so-called downstream tracking in order to remove lifetime biasing requirements from the VELO. In parallel I also refitted the primary vertices with all final state tracks from the b candidates explicitly removed. For simulated events I applied the VELO online tracking algorithm used in the trigger in order to assess effects arising from the slight difference between the VELO online and offline algorithms. The lifetime measurements were published in early 2014 [41].

Mid 2013 to early 2014: Ξ_b^- and Ω_b^- lifetime measurements

Taking advantage of the expertise gained from the b-hadron lifetime measurements I started a new analysis with the goal of measuring the lifetimes of Ξ_b^- and Ω_b^- using the full 3.0 fb^{-1} data set recorded in 2011 and 2012. This was mainly an individual effort, which is leading to a publication in the first half of 2014 [69].

2 Alignment

2.1 Software alignment procedure

Particle detectors like the ones at the LHC target a spatial resolution for tracks at the micrometer level. However, the size of such detectors is generally of several meters. Hence a physical alignment of the tracking sub-detectors with enough precision cannot be guaranteed at the installation of the individual parts. The state of the art technique is to install the detector parts with a millimeter precision, ensure them not to move during operation and only afterwards measure their exact position. These measurements, called software alignment, exploit data recorded by the detector itself. Whenever the word alignment is used hereafter, software alignment is implied.

In the absence of matter and magnetic field, tracks of charged particles are perfectly straight lines. This knowledge can be exploited to measure and correct for potential misalignments of tracking detector parts with respect to others. When matter or a magnetic field are present, the procedure becomes more complicated since a charged particle can be scattered or its trajectory curved depending on the momentum. However, it is still possible to measure and correct for misalignments using scattering corrections and extrapolations based on the knowledge of the magnetic field.

One way to quantify the misalignments is to first calculate track residuals, which are the distances separating a track, being an ideal curve, from its associated hits. Computing a χ^2 as the sum of χ^2 contributions from each residual, one can find a condition where it is minimal and which corresponds to the optimal alignment of all detector elements [70]. The χ^2 contribution for a track n with parameters x is given by

$$\chi_n^2 = \sum_{i=1}^{H} \left(\frac{m_i(a) - h_i(x_n)}{\sigma_i} \right)^2 \tag{2.1}$$

where H is the total number of hits, m_i is the position of hit i, a are the alignment parameters, σ_i is the measurement error on m_i and h_i is the position of the track closest to hit i. The expression of the track χ^2 contributions given in Eq. 2.1 can also be written in a vector and matrix form as

$$\chi_n^2 = \left(\frac{m(a) - h(x_n)}{\sigma} \right)^T V^{-1} \left(\frac{m(a) - h(x_n)}{\sigma} \right) \tag{2.2}$$

where V is the track covariance matrix which is usually diagonal and $(m-h)/\sigma$ is a vector with the H components $(m_i - h_i)/\sigma_i$. The set of alignment parameters a corresponds to the spatial degrees of freedom which are used to describe the position and the orientation of each detector element. Usually Cartesian coordinates (Tx, Ty, Tz) and three rotation angles around the axes of the Cartesian system (Rx, Ry, Rz) are used.

The alignment parameters a are common to all tracks in the considered sample and the track parameters x of a certain track n can be expressed as a function of these alignment parameters $x_n = x_n(a)$. With this expression, the alignment procedure is reduced to the problem of finding the condition where the sum of all track χ^2 contributions is minimal with respect to the alignment parameters. This can be expressed with the total derivative as

$$\frac{d\chi^2}{da} \equiv 0 \quad \text{where} \quad \chi^2 = \sum_n \chi_n^2. \tag{2.3}$$

In order to obtain the minimal condition of the total χ^2, the dependence of the χ^2 on the track and alignment parameters is linearly approximated around the initial values x_0 and a_0. The minimum χ^2 condition with new alignment parameters $a = a_0 + \Delta a$ is given by the solution of

$$\frac{d^2\chi^2}{da^2}\bigg|_{a_0} \Delta a = -\frac{d\chi^2}{da}\bigg|_{a_0}. \tag{2.4}$$

Solving this set of equations leads to a minimum limited to the linear approximation. Hence a few iterations are needed to converge to a final solution being the global minimum of the total χ^2. At each step all tracks need to be refitted in order to propagate the alignment parameters to the track parameters ($x_n = x_n(a)$) since the detector elements are displaced. Looking at the total χ^2 at each step provides a good measure of the convergence of the alignment procedure.
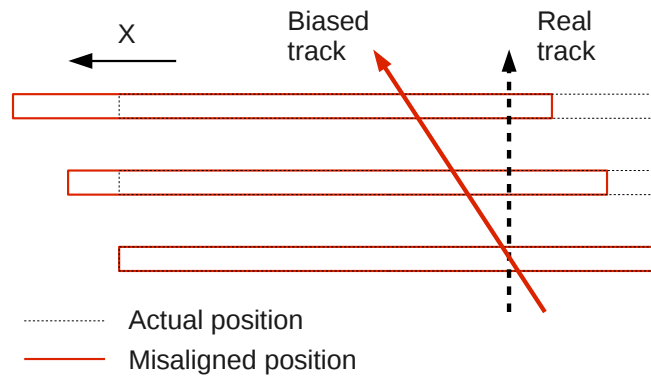
Figure 2.1: Shearing weak mode in a planar tracking detector. What is called the actual position is the physical position where the detector is located and the misaligned position is a position giving the same χ^2 without being physical.

2.1.1 Weak modes and associated challenges

Depending on the geometry of the detector, the software alignment procedure is not sensitive to all degrees of freedom of all detector elements. It is sometimes even possible that a change in a given degree of freedom of one or several detector parts does not change the value of the total χ^2. In this case this degree of freedom is called a weak mode. An illustration of a weak mode in a planar detector is shown in Fig. 2.1.

Understanding which degrees of freedom are sensible to align and which are weak modes represents a difficult challenge in the alignment procedure. Weak modes identified as such are usually not left free in the alignment process. Therefore the position of the detector parts along such degrees of freedom remains known with the precision of the survey performed at the detector installation which is at the millimeter level. Usually such degrees of freedom have a smaller impact on the quality of tracks and the precision of physics measurements than those that are not weak modes. Often it does not represent a large loss not to know with high precision the position of the detector elements along these directions.

2.1.2 Survey contributions

When certain degrees of freedom are not perfect weak modes or are not identified as such, it is very helpful to add other contributions to the total χ^2 which come from the laser survey of the detector parts performed after the installation. Such contributions avoid the position of the detector parts to move too far away from the surveyed position and be placed in physically impossible positions. However it is important to know well the uncertainty on the surveyed values to be used in the χ^2 calculation to leave an appropriate weight to the track residuals and take their contributions into account at the correct level of significance.

2.1.3   Effect of a curvature bias on the invariant mass

Some weak modes can have a direct effect on physics parameters. When the momentum is measured by tracking particles in a magnetic field which gives the curvature of the track, the overall momentum scale is very sensitive to certain weak modes. As an example, the weak modes shown in Fig. 2.2 have a direct effect on the invariant mass of two-track combinations.

In a uniform magnetic field B, the transverse momentum $p_\perp$ in the plane perpendicular to the field is measured from the curvature of the track. This curvature ω is defined as the inverse of the radius R of the track ($\omega = 1/R$). Applying the famous expression of the Lorentz force, the relation between the measured curvature and the transverse momentum is

$$\omega = \frac{QB}{p_\perp}, \tag{2.5}$$

Q being the charge of the particle. As an example, a shearing weak mode like the one on Fig. 2.2 introduces a constant bias in the measured curvature which, for a large curvature radius, does not depend on the momentum of a particle nor its direction:

$$\omega \longrightarrow \omega + \delta_\omega . \tag{2.6}$$
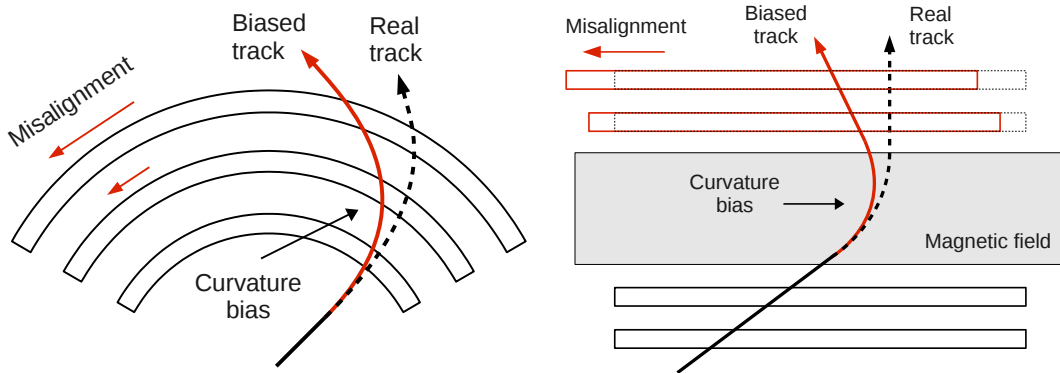
Figure 2.2: Example of a curvature bias in a cylindrical (left) and planar (right) tracking detector.

The invariant mass m computed from two very relativistic daughter particles with masses m_- and m_+ and momenta p_- and p_+ respectively can be approximated by

$$m \approx \sqrt{m_-^2 + m_+^2 + 2p_- p_+ (1 - \cos\theta)/c^2}\,, \tag{2.7}$$

where θ is the opening angle between the two tracks of the particles. From Eq. 2.5 and Eq. 2.6 one can compute the change in $p_\perp$ for a certain curvature bias δ_ω at first order in δ_ω/ω:

$$p_\perp \longrightarrow p_\perp \left(1 - \frac{\delta_\omega}{\omega}\right) = p_\perp \left(1 - \frac{\delta_\omega p_\perp}{QB}\right). \tag{2.8}$$

In forward spectrometers, the momentum measurement is dominated by its component perpendicular to the magnetic field, so Eq. 2.8 remains approximately correct when $p_\perp$ is replaced with p. Introducing the curvature bias from Eq. 2.6 into the expression of the invariant mass in Eq. 2.7 for a particle reconstructed with two daughters of charges $Q_- = -e$ and $Q_+ = e$ gives

$$m \longrightarrow \sqrt{m_-^2 + m_+^2 + 2p_- p_+ \left(1 + \frac{\delta_\omega p_-}{eB}\right)\left(1 - \frac{\delta_\omega p_+}{eB}\right)\frac{1 - \cos\theta}{c^2}}. \tag{2.9}$$

Neglecting the terms of order δ_ω^2 results in the expression

$$m \longrightarrow \sqrt{m_-^2 + m_+^2 + 2p_- p_+ \frac{1 - \cos\theta}{c^2} - 2p_+ p_- (p_+ - p_-)\frac{\delta_\omega}{eB}\frac{1 - \cos\theta}{c^2}}. \tag{2.10}$$

The term in δ_ω (the fourth term) being small compared to the expression of the unbiased invariant mass (the first three terms) one can expand the square root into

$$m \longrightarrow m\left(1 - (p_+ - p_-)p_+ p_- \frac{1 - \cos\theta}{m^2 c^2}\frac{\delta_\omega}{eB}\right). \tag{2.11}$$

Eliminating $p_+ p_- (1 - \cos\theta)$ using Eq. 2.7 gives the measured invariant mass at first order in δ_ω / ω:

$$m \longrightarrow m \left(1 - (p_+ - p_-) \frac{m^2 - m_-^2 - m_+^2}{2m^2} \frac{\delta_\omega}{eB} \right), \tag{2.12}$$

which is shifted by a quantity directly proportional to the curvature bias δ_ω and to the momentum difference between the two daughter particles.

2.1.4 Vertex and mass constraints in software alignment

Vertices are very useful for the alignment because they carry additional spatial information as compared to tracks. The knowledge that can be included is that all tracks originating from the vertex must meet in one single point. Hence an additional penalty term can be added into the χ^2 calculation in a similar way than for the tracks. A term like in Eq. 2.1 is computed in which h is replaced by a model where all tracks from the vertex meet in a single point [68].

Furthermore it is possible to turn the previously discussed momentum dependence issue around and use mass information in the alignment procedure to make it sensitive to the related weak modes. As seen previously, the invariant mass resulting from the combination of two daughter particles strongly depends on the measured momentum of the daughter tracks and gives a direct dependence on the momentum scale, hence on the associated degrees of freedom. Using very clean samples of secondary reconstructed particles based on two or more charged daughter particles gives a hint on the residual misalignment. Constraining the invariant mass to its known value, by adding yet another penalty term to the χ^2 calculation proportional to the square of the mass residual ($m_{\mathrm{reco}} - m_{\mathrm{true}}$), makes the whole procedure sensitive to the weak modes related to momentum measurements.

2.2 Application to the LHCb tracking detectors

At LHCb the alignment is performed in three steps. First the VELO sensors are aligned on their own, secondly the tracking planes upstream and downstream of the magnet (TT, IT and OT) are aligned with respect to the VELO, lastly all remaining detector parts (RICH, calorimeters, muon chambers) are aligned with respect to the tracking systems. The coordinate system at LHCb has a z axis along the beam line pointing from the VELO towards the calorimeters, a vertical y axis pointing upwards and an x axis perpendicular to the other two, forming a right-handed Cartesian coordinate system. All tracking detectors and their orientation in the coordinate system of LHCb are schematically depicted in Fig. 2.3.
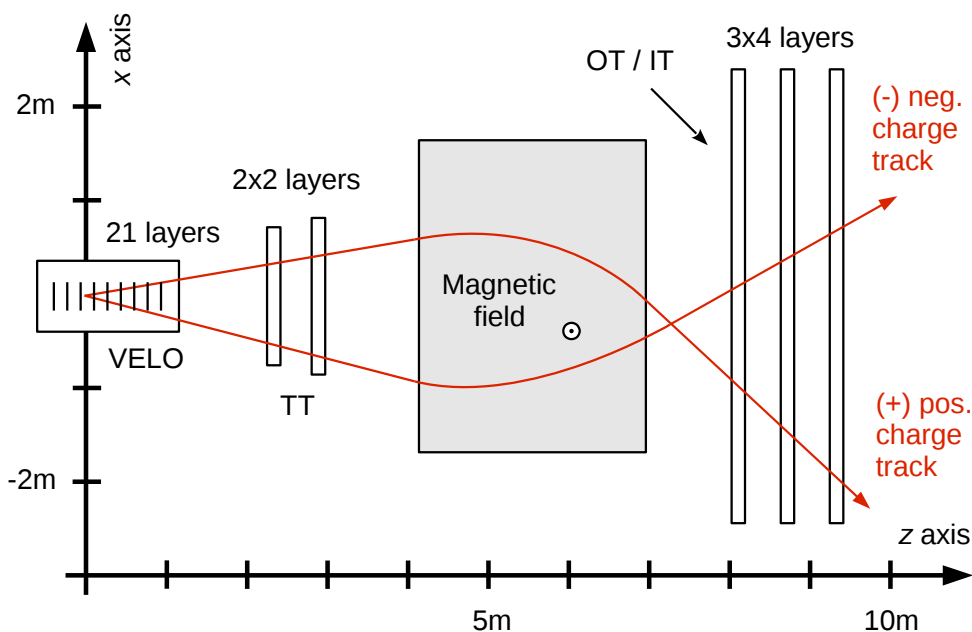
Figure 2.3: Schematic view from the top of the LHCb tracking system.

2.2.1 VELO alignment

The first step of the alignment procedure at LHCb is the standalone VELO alignment [71]. A global reference is needed with respect to which all other detector elements can be aligned and this has been chosen to be a module of the VELO consisting of one ϕ- and one R-sensor that have their position fixed. Both sensors have to be fixed to provide a three dimensional point in space which is needed for an absolute reference. The initial values of all alignment constants, used in the first iteration of the alignment, are given by the coordinates from the laser survey conducted during and just after the detector installation.

In August and September 2008 controlled beam dumps on a target located a few hundred metres upstream of the LHCb experiment provided a high illumination of the detector with almost parallel tracks. These first recorded data, called hereafter TED data as a reference to the Transfer line External beam Dump, were used to get a preliminary data-based alignment. However in such data all tracks are parallel to the beam line which leaves the translation degrees of freedom along z (Tz) unconstrained.

The latest alignment starts from the alignment constants obtained with TED data and uses real pp collisions as well as collisions between protons and residual gas in the beam pipe (called beam-gas collisions). In the pp collisions the primary vertex (PV) information is used by applying a vertex constraint based on the PV and the tracks it is made of. This helps to link the left and right VELO halves since both contribute to measure each PV. Overlap tracks, i.e. tracks that have hits in VELO sensors from both halves, are also selected with priority in order to align the halves with respect to each other.

Besides the nominal pp collisions there are also beam-gas collisions and so-called satellite collisions, happening at ±700 mm around the targeted interaction point. The satellite collisions are collisions between a bunch of protons that is meant to collide and a bunch from the opposite beam that arrives 5 ns later. This is possible due to the fact that the proton acceleration in the LHC is performed by RF cavities that allow a minimal bunch spacing of 2.5 ns. Exploiting data containing these additional collisions helps reducing the Rz-twist weak mode which is a rotation of the VELO modules around Rz that is directly proportional to the z coordinate of the modules. Such a twist has a strong effect on the impact parameter (IP) measurements of the tracks.

The fact that the VELO halves are physically moved each time a new run starts at the LHC implies that the stability of its position needs to be monitored. This is done by looking at the average x, y and z coordinates of the PVs reconstructed independently with each half. The discrepancies between the averages show that during a whole year of data taking the VELO halves are closed into the same position with a precision of ±5 μm. This is remarkable, knowing that the VELO is opened and closed several hundred times by 3 cm.

With this alignment technique, the VELO sensor positions are known with a precision of 5 μm along Tx and Ty and of 200 μrad around Rz. This permits a track resolution of around 4 μm and a PV resolution of (13.0, 12.5, 68.5) μm along (x, y, z).

2.2.2 Global alignment

Once the VELO elements are aligned they are frozen and the other tracking detectors are aligned with respect to the VELO. This procedure is called the global alignment or the alignment of the spectrometer. To perform it, a set of approximately 250'000 tracks from 100'000 pp collision events is selected. There are three categories of selected tracks defined in Table 2.1. The categories emphasize important requirements for tracks that are useful for the alignment. It is necessary that all tracks leave many hits in all detector elements, that they are of good quality (low track χ^2/ndf), that they have high momentum and that a large fraction are overlap tracks, i.e. tracks that pass through two neighbouring detector elements.

Simulation and data are both used to determine the degrees of freedom that are left free in the alignment procedure [72]. A certain degree of freedom is included into the alignment if there is enough sensitivity to make the procedure converge well after a reasonable number of iterations, typically ten. To test the convergence in simulation, misalignments for a certain degree of freedom are manually introduced into the constants from which the alignment procedure starts. If the alignment is able to correct for these misalignment and determine the actual simulated position of the detector elements from the simulated tracks, then it is assumed that it makes sense to include this degree of freedom. The convergence of the alignment on real data is also used to confirm these decisions.

Table 2.1: Selection of tracks and primary vertices being used in the alignment of the TT, IT and OT tracking detectors. The overlap tracks in Category 1 need to have hits in at least two different boxes of IT or OT in the same layer (hence it includes purely IT, purely OT and IT+OT overlap tracks).

Category 1: overlap tracks	
p	$30-200$ GeV/c
Track χ^2/ndf	< 5
Match χ^2/ndf	< 5
VELO χ^2/ndf	< 5
Track type	Long
IT hits	> 4
VELO R hits	> 5
VELO ϕ hits	> 5
Require overlap	True

Category 2: tracks with many IT hits	
p	$50-200$ GeV/c
Track χ^2/ndf	< 5
Match χ^2/ndf	< 5
VELO χ^2/ndf	< 5
Track type	Long
IT hits	> 8
VELO R hits	> 5
VELO ϕ hits	> 5

Category 3: long tracks with many VELO hits	
Track χ^2/ndf	< 5
Match χ^2/ndf	< 5
VELO χ^2/ndf	< 5
Track type	Long
VELO R hits	> 13
VELO ϕ hits	> 13

Cuts on primary vertices	
χ^2/ndf	< 10
Tracks	> 5
Long tracks	> 2
x coordinate	$[-5; 5]$ mm
y coordinate	$[-5; 5]$ mm
z coordinate	$[-200; 200]$ mm

Table 2.2: Degrees of freedom left free in the global alignment procedure.

Detector element	Number of elements	Degree(s) of freedom
IT box	$3 \times 4 = 12$	Tx Tz Rz
IT layer	$12 \times 4 = 48$	Tx Tz
IT ladder	$48 \times 7 = 336$	Tx Rz
OT C-frame	$3 \times 2 \times 2 = 12$	Tx
OT layer	$12 \times 2 = 24$	Tz
OT module	$24 \times 2 \times 9 = 432$	Tx Rz
Whole TT	1	Tz
TT layer	$2 \times 2 = 4$	Tz
TT module	280	Tx Rz

The best alignment precision that one can obtain for TT, IT and OT is along the Tx axis. This is due to the fact that all three tracking sub-detectors have their sensors vertically oriented (along y), hence there is only a small pitch along x between the microstrips or the straw tubes. For the same reason, the only angular degree of freedom that can sensibly be aligned is Rz. Tracks with large polar angles permit to constrain the Tz degree of freedom but only for large elements that are highly illuminated. The degrees of freedom which are left free, i.e. are aligned, are summarised in Table 2.2.
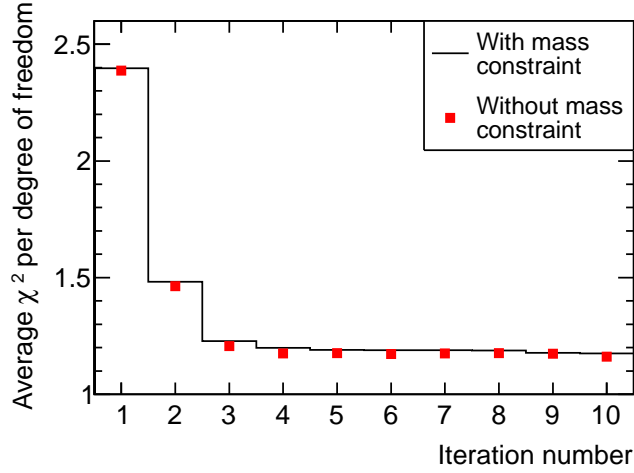
Figure 2.4: Convergence of the global alignment procedure.

As shown in Fig. 2.4, the alignment of the TT, IT and OT converges within less than ten iterations. Each iteration needs approximately 6800 s of computing time with a 2.8 GHz Xeon processor.

Very little sensitivity along Ty can be obtained with the standard method described above. An innovative technique using data recorded without magnetic field is applied [73]. VELO tracks are extrapolated to the TT, IT and OT and corresponding hits are searched within a window of a few mm around the expected position. The distribution of the found hits gives a measure of the edges of the sensitive areas of each detector element. Fitting these distributions, the position along y of each element is extracted.

2.2.3 $J/\psi \to \mu^+\mu^-$ and $D^0 \to K^-\pi^+$ mass constraints

The vertex and mass constraints described in Sec. 2.1.4 are applied using the abundantly reconstructed decays $J/\psi \to \mu^+\mu^-$ and $D^0 \to K^-\pi^+$. However, it seems that the mass constraint using $D^0 \to K^-\pi^+$ performs slightly better due to its kinematic asymmetry and to the fact that at LHCb it is reconstructed with less background. Around 13'000 primary vertices and around 85'000 decays are selected in the 100'000 events needed for the alignment. Figure 2.5 shows how the mass resolution is improved by more than 40% when a mass constraint is applied in the alignment.

As previously described, a strong dependence of the invariant mass on the difference between the momenta of two daughters appears when the detector is misaligned along a direction perpendicular to the magnetic field. This can happen at LHCb in the form of a global shearing along the degree of freedom Tx which is precisely perpendicular to the magnetic field. This shearing is centred around the interaction point in the VELO and translates approximately into a global shift of IT and OT along x. A mass constraint helps the alignment as demonstrated in Fig. 2.6.
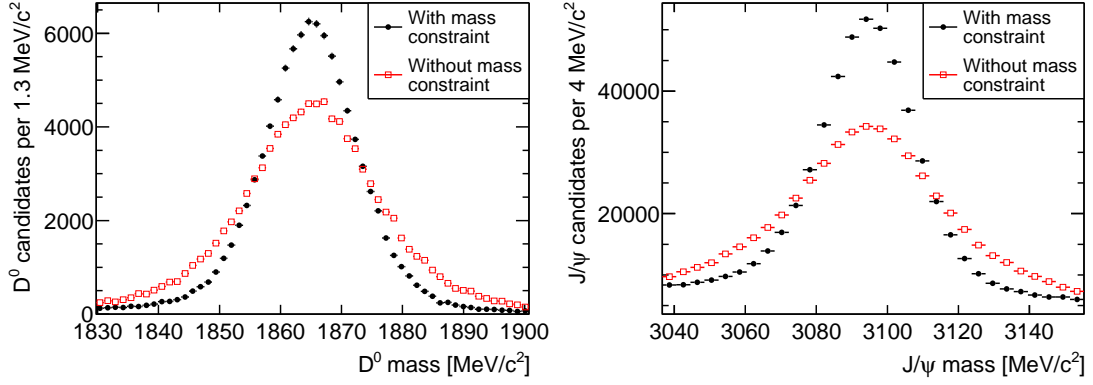
Figure 2.5: Invariant mass of reconstructed $D^0 \rightarrow K^- \pi^+$ (left) and $J/\psi \rightarrow \mu^+ \mu^-$ (right) decays using an alignment without (red squares) or with (black dots) D^0 mass constraint. The reconstructed D^0 decays belong to a different sample than those used as input for the alignment.
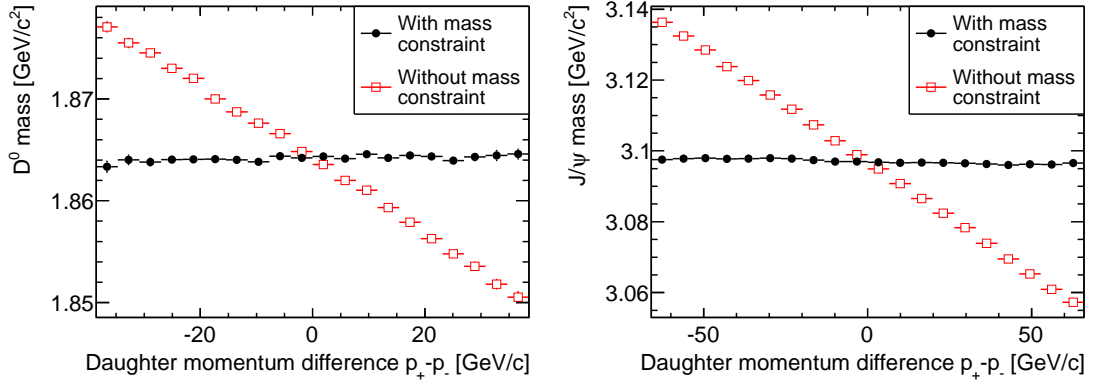
Figure 2.6: Average reconstructed $D^0 \rightarrow K^- \pi^+$ (left) and $J/\psi \rightarrow \mu^+ \mu^-$ (right) invariant masses as a function of the momentum difference between the two daughter particles using an alignment without (red squares) and with (black dots) D^0 mass constraint. The reconstructed D^0 decays belong to a different sample than those used as input for the alignment.

Using the slope s of the average mass as a function of the daughter momentum difference $(p_+ - p_-)$ from Fig. 2.6 and combining it with Eq. 2.12 one can compute the curvature bias δ_ω:

$$\delta_\omega = \frac{2meBs}{m^2 - m_-^2 - m_+^2} \tag{2.13}$$

In both the D^0 and the J/ψ case the curvature bias from the alignment without mass constraint equals $\delta_\omega = eB \times 0.40 \times 10^{-3}\ c \cdot \text{GeV}^{-1}$. This gives confidence that the bias indeed comes from

27
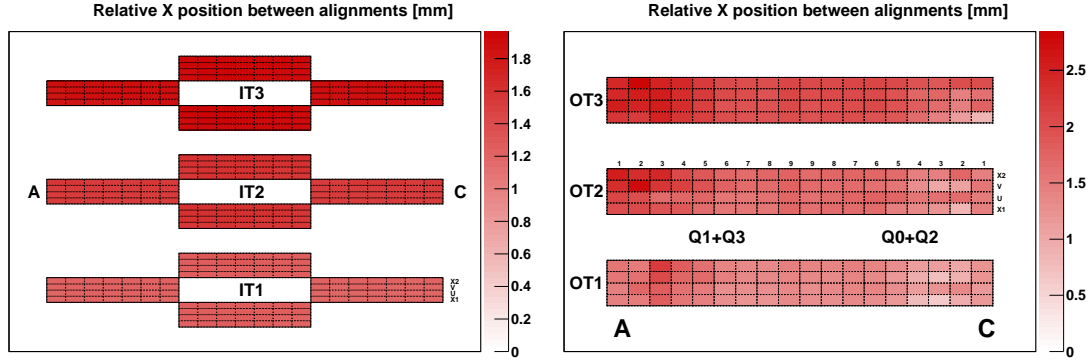
Figure 2.7: Difference along Tx of the IT (left) and the OT (right) between an alignment with and without D^0 mass constraint. Each rectangle corresponds to an IT ladder or an OT module and the colour code represents the difference in the absolute position of the element in the two alignments. One observes a clear shearing pattern where the difference in Tx is proportional to the z coordinate.

a single curvature bias. A study performed in Ref. [74] gives a relation between the curvature bias and an expected misalignment of the T-stations along Tx with respect to the VELO:

$$\frac{\delta_\omega}{eB} \frac{1}{\Delta \text{Tx}} = (2.20 \pm 0.05) \times 10^{-7} \, [c \cdot \mu\text{m}^{-1} \cdot \text{GeV}^{-1}]. \tag{2.14}$$

The computation gives 1.8 mm which is perfectly consistent with the difference between the alignment with and without mass constraint as illustrated on Fig. 2.7.

2.3 Momentum scale calibration

After the alignment, a so-called momentum scale calibration is performed [4, 40, 75]. Its purpose is to calibrate the momentum measurement for each track using well known resonances reconstructed at LHCb. It is needed because the alignment as well as the knowledge of the magnetic field are not perfect. The alignment is made only for certain degrees of freedom and can not take into account deformations, i.e. small discrepancies between the software detector description and reality. The magnetic field has been measured in many thousand points using a highly sensitive probe but there is still room for improvement. Especially the knowledge of the global position and orientation of the magnetic field is limited to the mm level.

The procedure of the momentum scale calibration is iterative. At each step an abundant resonance (often $J/\psi \to \mu^+ \mu^-$) is reconstructed and a factor $(1 - \alpha)$ is computed by which the momenta of the final state particle need to be multiplied to shift the average of the

reconstructed mass to the central value given by the Particle Data Group (PDG) [1]. The computation is performed at first order using the approximation derived in Ref. [75]:

$$\alpha = \frac{\Delta m \cdot m}{f - m^2} \quad \text{with} \quad f = m_+^2 + m_-^2 + \frac{p_-}{p_+} \cdot m_+^2 + \frac{p_+}{p_-} \cdot m_-^2 \tag{2.15}$$

where m is the average reconstructed invariant mass, Δm is the difference between m and the PDG mass and $m_\pm$ and $p_\pm$ are respectively the mass and the momentum in the laboratory frame of the daughter particles. After the computation all final state particles have their momenta multiplied by the $(1 - \alpha)$ factor and the process starts again.

Once the procedure converged, the momentum scale is applied to the final state particles of many other resonances in order to verify the consistency. An estimate of the uncertainty on the α parameter is usually made from the spread of the remaining α computed using Eq. 2.15 for several other resonances. The final value of $(1 - \alpha)$ is applied to all stable particles in each analysis to ensure their momentum to be as accurately known as possible.

2.4 Alignment experience and performance

2.4.1 The TT operating temperature issue

Close to the end of the 2010 run it was noticed that the reconstructed mass of the $J/\psi \to \mu^+ \mu^-$ decays was not stable as a function of the data taking period, as shown in Fig. 2.8. In parallel it was seen that alignments of different data taking periods did not converge to the same constants or that the quality of a certain alignment is not constant like displayed in Fig. 2.9.

The suspect data were found to be runs 81310–81476 which represent 30% of the total integrated luminosity of the 2010 data. It appeared that a change in the operating temperature of the TT during this period had led to significant changes in the physical position of the sensors. The operating temperature was changed from $+5°$ to $-5°$ in runs 81310–81375 and to $-15°$ in runs 81376–81476 before it was set back to $+5°$. The purpose of these changes was to study the reduction at lower operation temperatures of the silicon aging due to radiation damage.

Figure 2.8 uses J/ψ candidates reconstructed with an alignment based on data recorded during a period where the TT operating temperature remained unchanged. Producing the same figure than Fig. 2.8 but excluding all TT information in the reconstruction (but not in the alignment) shows a lower trend as shown on Fig. 2.10. This confirmed the role of the TT in the instabilities of the J/ψ mass.
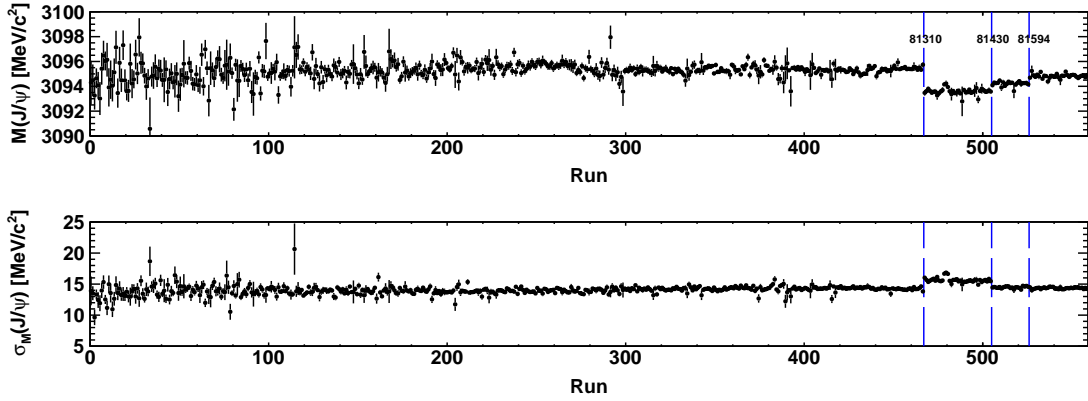
Figure 2.8: Reconstructed mass (top) and mass resolution (bottom) of $J/\psi \to \mu^+\mu^-$ decays as a function of run number in 2010. The vertical lines correspond to changes in the operating temperature of the TT. Points with large error bars correspond to low statistics runs.
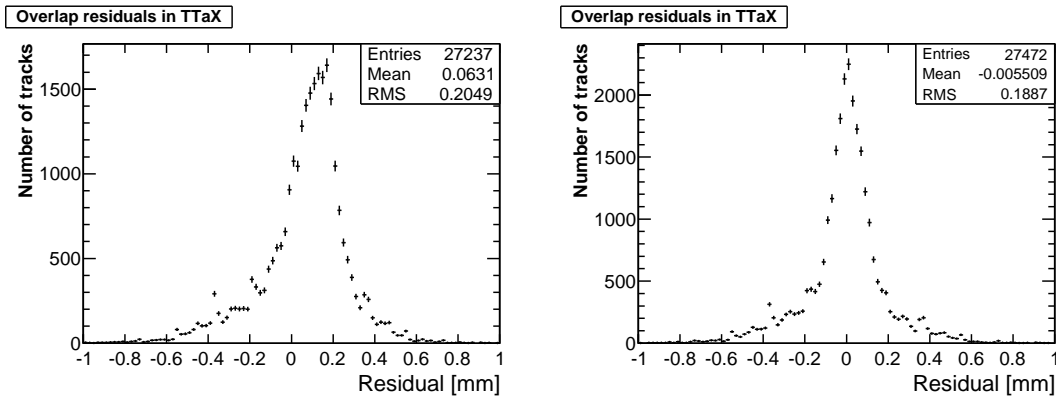
Figure 2.9: Distribution of TT residuals with alignments performed for two different periods (left and right). The same alignment constants are used for both periods, determined with data from the second period (on the right). The two periods differ by the TT operating temperature.

An alignment for each TT operating temperature was produced where only the TT was re-aligned (using the same degrees of freedom described in Table 2.2). To correct for residual steps due to effects that the alignment cannot correct for (non linear deformations, twisting, etc.), the momentum scale calibration was also repeated separately for each TT operating temperature condition. The stability plot of the J/ψ mass with all corrections applied is given in Fig. 2.11. After all corrections the J/ψ mass remains stable within the statistical fluctuations.
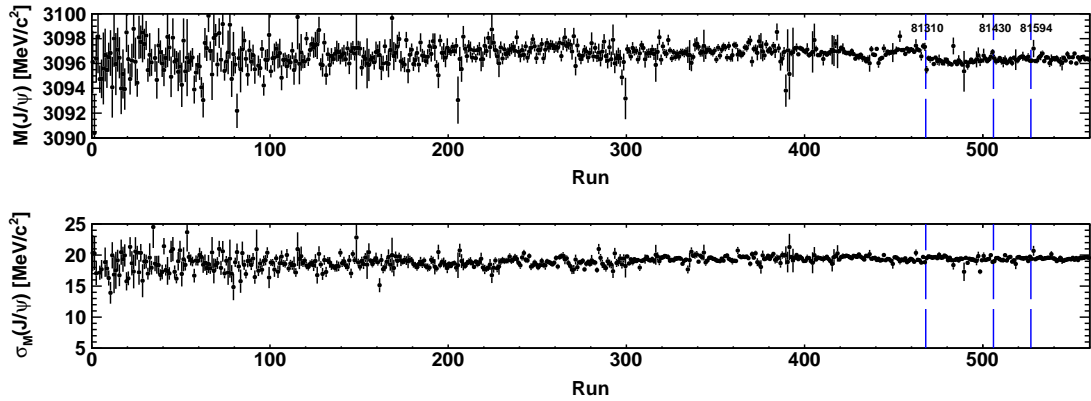
Figure 2.10: Reconstructed mass (top) and mass resolution (bottom) of $J/\psi \to \mu^+\mu^-$ decays as a function of run number in 2010, without use of the TT information. The vertical lines correspond to changes in the operating temperature of the TT.
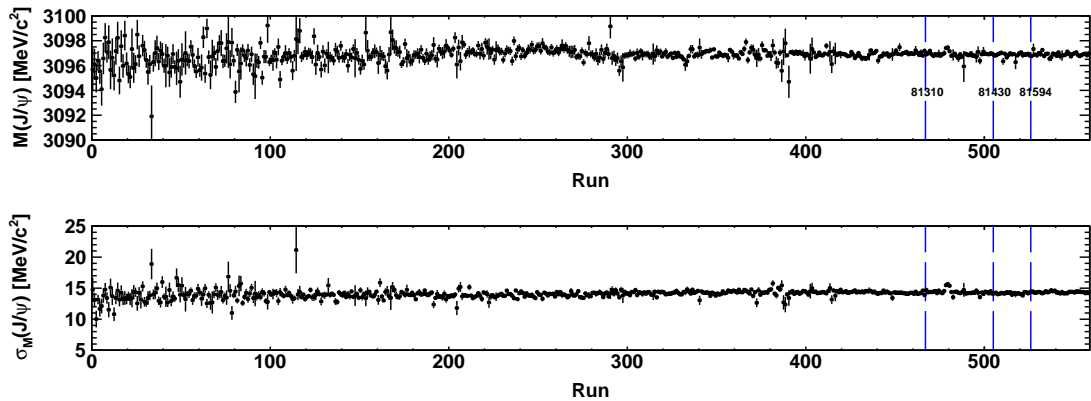
Figure 2.11: Reconstructed mass (top) and mass resolution (bottom) of $J/\psi \to \mu^+\mu^-$ decays as a function of run number in 2010, using the new per-period alignments and the per-period momentum calibrations. The vertical lines correspond to changes in the operating temperature of the TT.

Another effect was also found when studying the reconstructed J/ψ mass as a function of the angle between its decay plane and the direction of the magnetic field, illustrated on Fig. 2.12. The per-period alignment using the $D^0 \to K^-\pi^+$ mass constraint also significantly reduces this dependence which became stronger when the TT was operated at a different temperature.

31
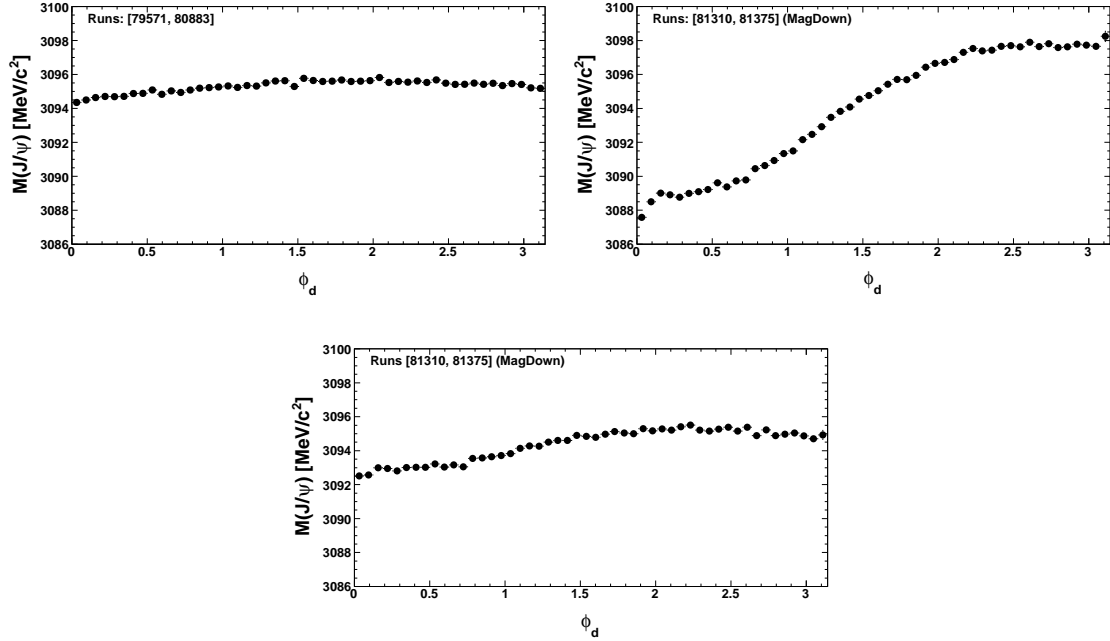
Figure 2.12: Reconstructed $J/\psi \rightarrow \mu^+\mu^-$ mass as a function of the angle between the decay plane and the magnetic field for events before the TT temperature change (top left), events after the TT temperature change (top right) and events after the TT temperature change with the new alignment (bottom).

2.4.2 The particular case of the Tz degree of freedom

Due to the detector geometry, the Tz degree of freedom is weakly constrained in the alignment as compared to other degrees of freedom like Tx. Only the few tracks that form a large angle with the detector planes provide sensitivity along this direction. However the sensitivity is strong enough to make the alignment converge when the Tz degree of freedom is left free for large detector elements like full layers.

Some puzzling results appeared with the first alignments exploiting data from real pp collisions in 2010. There was a discrepancy large enough to be physically impossible between the surveyed values and the alignment constants in the Tz degree of freedom for both TT and the T-stations.

For TTa (TTb) the difference between the z position given by the 2010 alignment procedure and the corresponding position measured during the survey was of 1.5 mm (1.9 mm). This difference is very difficult to explain since the survey has a precision below the mm level and the alignment is expected to perform even better. For 2010 data it was decided to keep the constants from the alignment procedure as reference for the reconstruction. However for 2011 data the Tz degree of freedom for the TT elements was removed from the alignment procedure
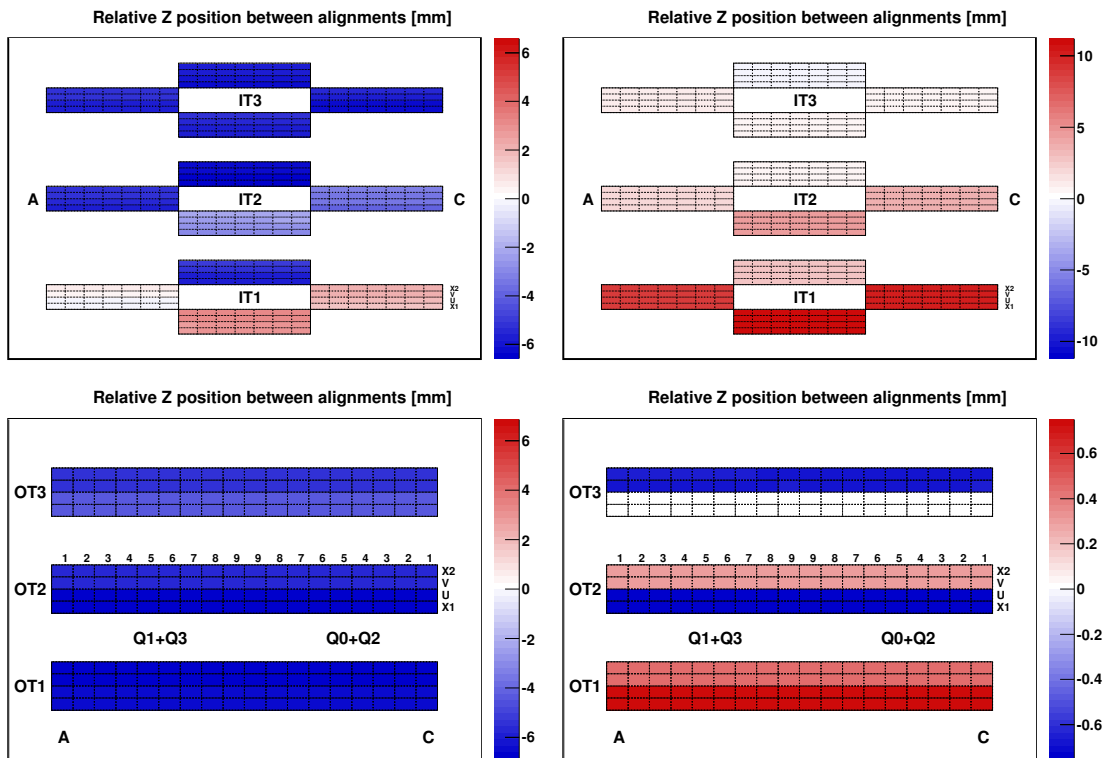
Figure 2.13: Difference in the global position along z between the survey constants and the 2010 alignment constants (left) or 2011 alignment constants (right) for IT (top) and OT (bottom). The layout and colour code are the same as in Fig. 2.7. The two OT layers in OT3 appearing in white in the bottom right plot are the ones constrained to the survey values.

and the constants were fixed to their survey values. In 2012 and for the reprocessing of the 2011 data with *Reco14*, the TT elements were aligned again along the Tz degree of freedom.

In the T-stations there were two effects. First the overall z position of the whole T-system was unstable in the alignment. This was corrected by fixing two OT layers from station T3 to the surveyed z position for the 2011 and 2012 alignments.

A more astonishing result is that the distance between T1 and T3 differs between the alignment result and the surveyed values by more than 10 mm. As shown in Fig. 2.13 it is not a uniform deformation of the detector. The survey having been performed without the presence of the magnetic field, a hypothesis was that detector elements close to the magnet move due to the field. After more than one year a new survey was performed measuring the position of the structure holding the IT boxes and a physical movement of around 5 mm for IT1 was measured when the magnetic field is switched on. This explains part of the observed discrepancy between alignment and survey and shows that the alignment is sensitive along Tz for a relative measure between the T-station layers.

The remaining part of the discrepancy may be explained by the overall VELO z scale, the limited knowledge of the magnetic field map (even though it was partially remeasured in 2011) or the distance between the magnet and the VELO which is fixed in the alignment. No further investigation was undertaken as these differences between the survey and alignment values do not strongly affect the physics measurements.

2.4.3 Global alignment performance with 2010 data

For 2010 data the alignment strategy includes the previously described vertex and mass constraints in addition to the high quality track input. A way to measure the performance of the best alignment constants obtained is to look at the distribution of the so-called biased track residuals for each aligned element, typically a readout-sector (corresponding to a ladder for IT and a module for TT). This biased track residual is the track residual computed for a hit that is included in the track fit, as opposed to the unbiased track residual in which the hit is explicitly removed from the track fit.

The mean of the biased track residual distribution for a sector gives a hint on the remaining local misalignment (a global misalignment of full detector boxes would have no effect). To obtain an average estimate of the local misalignment in a full sub-detector, the means of the biased track residual distributions for all readout-sectors are plotted in a histogram. These histograms are called sector biased residuals and are shown in Fig. 2.14 for IT and TT using the best alignment in 2010. The RMS of these distributions is a good measure of the average remaining local misalignment and is equal to around 15 µm for both silicon trackers, IT and TT.
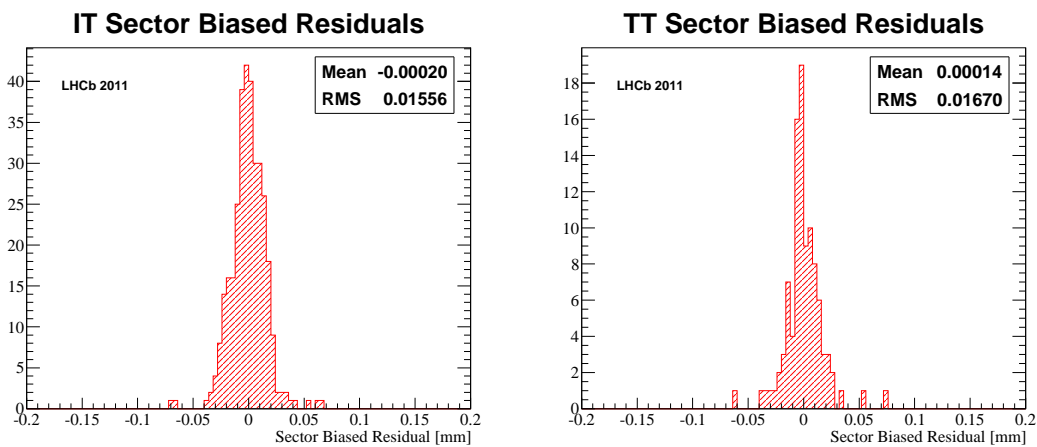
Figure 2.14: Distribution of sector biased residuals for IT (left) and TT (right).

2.4.4 Global alignment for the 2011 and 2012 data sets

The alignment strategy for 2011 and 2012 was to perform several alignments during the year, one for each data taking period. It was decided to use large $D^0 \to K^- \pi^+$ samples as mass constraints. As previously described, the degrees of freedom left free in 2011 and 2012 are the ones described in Table 2.2 with the exception of the Tz degree of freedom for the TT elements. In addition two layers of OT3 are constrained to the surveyed values. The precision of these alignments is comparable to what was obtained with 2010 data.

3 Mass measurements of the Λ_b^0, Ξ_b^-, Ξ_b^0 and Ω_b^- baryons

Using the whole data set recorded in 2011, corresponding to 1.0 fb^{-1} at $\sqrt{s} = 7$ TeV, the masses of the Λ_b^0, Ξ_b^- and Ω_b^- are measured by reconstructing the b baryons in exclusive $b \to J/\psi X$ modes. A search for the $\Xi_b^0 \to J/\psi \, \Xi^- \pi^+$ decay is also performed.

3.1 Data and Monte Carlo samples

The data used for the mass measurements was recorded during the 2011 run, reconstructed using *Reco 12* and stripped with *Stripping 17b*. The total integrated luminosity is 1.0 fb^{-1} of pp collisions with a centre-of-mass energy of $\sqrt{s} = 7$ TeV. Around half of the data was recorded with the magnetic field pointing upwards and the other half with the magnetic field pointing downwards.

Several Monte Carlo (MC) samples were generated as summarised in Table 3.1. All but the Ω_b^- sample were produced officially by the LHCb MC production team. All samples were applied cuts at the generator level in order to remove decays with daughter particles flying outside the LHCb detector acceptance. These cuts require the charged daughter particle tracks to form an angle with respect to the z axis between 10 and 400 mrad and the muons between 5 and 400 mrad. The angle on which the cut is applied is taken at the point where a particle is created, before it flies into the magnet region. The daughter particles of the long-lived hadrons are excluded from these cuts.

The problem for the Ω_b^- is that the generator (Pythia) generates random events of pp collisions which do not necessarily contain the desired hadron. Whenever an event does not contain the hadron, the generated event is discarded and the generation is repeated. The Ω_b^- baryon is generated very rarely as two s quarks and one b quark need to hadronize into a single particle. Hence the computing time becomes dominated by the random generation of events and is too large. The trick used to get around this issue consists of generating Ξ_b^- baryons instead of Ω_b^- baryons, but giving to the Ξ_b^- baryon in the simulation database the mass and the lifetime of the Ω_b^- and forcing it to decay into the wanted decay products ($J/\psi \; \Omega^-$). Applying this trick, by

Table 3.1: Monte Carlo samples used in the analysis. The events have been required to pass acceptance cuts (see text). The event type is a unique LHCb-internal identifier for each decay.

Simulated decay	Event type	Number of events
$\Lambda_b^0 \to J/\psi\,\Lambda$	15144103	8'000'000
$\Xi_b^- \to J/\psi\,\Xi^-$	16145131	4'000'000
$\Xi_b^0 \to J/\psi\,\Xi(1530)^0$	16146141	2'000'000
$\Omega_b^- \to J/\psi\,\Omega^-$	16145132	500'000

writing a dedicated decay description file, and using the official LHCb simulation framework, the sample of Ω_b^- decay was simulated at the local computer cluster at EPFL.

3.2   Stripping and selection

All events passing any trigger line are considered in this analysis. The reconstructed decays are $\Lambda_b^0 \to J/\psi\,\Lambda$, $\Xi_b^- \to J/\psi\,\Xi^-$, $\Xi_b^0 \to J/\psi\,\Xi(1530)^0$ and $\Omega_b^- \to J/\psi\,\Omega^-$ where the daughters are reconstructed in the $J/\psi \to \mu^+\mu^-$, $\Xi(1530)^0 \to \Xi^-\pi^+$, $\Xi^- \to \Lambda\pi^-$, $\Omega^- \to \Lambda K^-$ and $\Lambda \to p\pi^-$ decay modes. At LHCb the most common particles are directly reconstructed in all events with very loose cuts as so-called *Common Particles*. The stripping lines building the b-baryon candidates start from *Common Particles* of the J/ψ, the pions, the kaons and the Λ. The J/ψ candidates are only reconstructed with muons from long tracks that also have hits in the muon stations. The pions and kaons as well as the Λ daugthers are reconstructed as long or downstream tracks.

The fact that both long and downstream tracks are used in the reconstruction implies that several track type combinations are built. The Λ is reconstructed either with two long tracks (LL) or with two downstream tracks (DD). The rare cases of LD or DL candidates are not considered. The bachelor hadron (pion or kaon) from the Ξ^- or Ω^- decay can also be reconstructed as a long or downstream track. Hence the Λ_b^0 candidates are either LL or DD and the Ξ_b^-, Ξ_b^0 and Ω_b^- candidates are reconstructed as LLL, LDD or DDD, where the first letter denotes the track type of the bachelor pion or kaon and the last two the track types of the Λ daughters. The $\Xi(1530)^0$ candidates are built by associating a long track pion with a Ξ^- candidate. When combining the final state tracks into candidates, the stripping algorithm applies the selection summarised in Table 3.2.

Some quantities the stripping requirements are based on need to be defined. First the so-called Impact Parameter (IP) is defined as the closest distance between a track and a vertex, usually a Primary Vertex (PV). The IP χ^2 of a track with respect to a vertex is defined as the difference between the vertex χ^2 of a fit where the considered track is included and the vertex χ^2 of a fit where the track is not included. The best PV with respect to a certain reconstructed track or particle is chosen as the PV that gives the smallest IP χ^2. Each b-baryon candidate

Table 3.2: Requirements of the stripping selection. BPV DLS stands for the decay length significance of the reconstructed particle with respect to the best PV. All mass windows are centered on the PDG mass values [1].

Λ requirements	
Proton p_T	> 500 MeV/c
Pion p_T	> 100 MeV/c
Mass window	± 15 MeV/c^2
Vertex χ^2/ndf	< 20
BPV DLS (not for Λ_b^0)	> 5

Ξ^- or Ω^- requirements	
Pion/kaon p_T	> 100 MeV/c
Pion/kaon IP χ^2	> 9
Mass window	± 30 MeV/c^2
Vertex χ^2/ndf	< 25
BPV DLS	> 5

$\Xi(1530)^0$ requirements	
Mass window	± 150 MeV/c^2
Vertex χ^2/ndf	< 25

b-baryon requirements	
Λ_b^0 vertex χ^2/ndf	< 10
Λ_b^0 mass window	± 500 MeV/c^2
Ξ_b^- vertex χ^2/ndf	< 25
Ξ_b^- mass window	± 300 MeV/c^2
Ξ_b^0 vertex χ^2/ndf	< 25
Ξ_b^0 mass window	± 500 MeV/c^2
Ω_b^- vertex χ^2/ndf	< 25
Ω_b^- mass window	± 500 MeV/c^2

Other requirements	
Pion PIDK	< 5
Kaon PIDK	> -5
All track χ^2/ndf	< 4

is associated with its best PV, assumed to be the proton-proton collision point where it is produced.

After the reconstruction and selection of the candidates by the stripping, the full decay chain is refitted using a fit based on a Kalman filter and implemented in the *DecayTreeFitter* (DTF) tool [76]. The DTF tool also allows to constrain the invariant mass or the origin direction of a reconstructed particle in the decay chain. For the present analysis, the masses of the direct b-baryon decay products are constrained to their PDG value [1] and the b baryons are constrained to originate from their associated PV.

The candidates passing the stripping selection undergo the so-called offline selection which is cut-based and tuned to maximize the signal significance. The offline selection of Ξ_b^- and Ω_b^- is optimized using MC simulated events to mimic the signal, real background events from the mass sidebands and a signal yield estimate based on previous measurements [6, 7, 9] as well as the preliminary LHCb measurement [77]. The yield estimate is used to scale the simulated sample to reproduce the expected value. The quantity that is maximised is $S/\sqrt{S+B}$, where S is the signal yield from a fit with a Gaussian function of the true signal candidates in the scaled simulation and B the background fitted in data and computed in a mass window of ± 30 MeV/c^2 around the simulated mass of the b baryon. Figure 3.1 shows the signal and background distributions of three observables used in the optimization, as well as the chosen cuts.
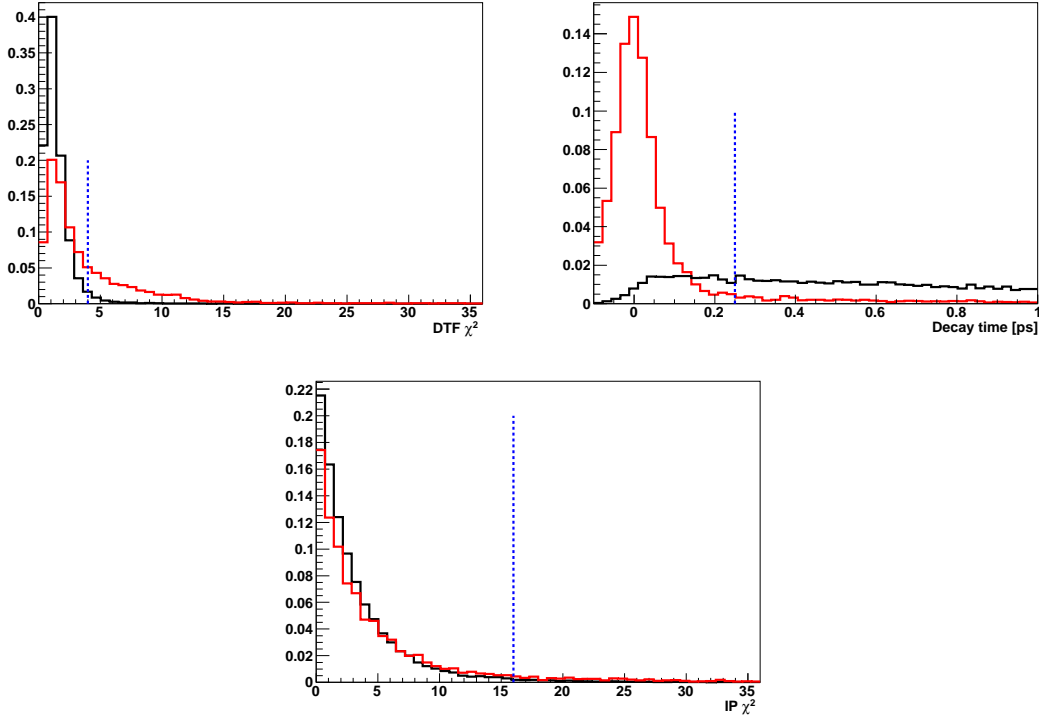
Figure 3.1: DTF χ^2/ndf (top left), decay time (top right) and IP χ^2 distribution of simulated Ξ_b^- signal candidates (black solid line) and Ξ_b^- candidates from sidebands in data (red solid line). All distributions are normalised to unit area. The vertical dotted blue line shows the chosen cut value which maximises the significance as described in the text.

The Λ_b^0 selection is taken from a previous mass measurement analysis [4] performed by the EPFL group, as no large gain in terms of statistical uncertainty is expected from a re-optimization. Because no expectations for the Ξ_b^0 yield exist, the offline selection criteria for the Ξ_b^0 are taken to be identical to the ones for the Ξ_b^- selection. Since only a $\pm 150 \, \text{MeV}/c^2$ mass window is applied to the $\Xi(1530)^0$ candidates in the stripping and no further offline cuts are added, some non-resonant component ($\Xi_b^0 \to J/\psi \, \pi^+ \Xi^-$) might contribute to the Ξ_b^0 signal yield.

The offline selection is summarised in Tables 3.3 and 3.4. Since the topologies of the considered decays are similar, the offline selections differ only slightly.

3.3   Track extrapolation and momentum scale

Many final state tracks, especially downstream tracks, are measured up to several metres away from their origin vertex. Between the origin vertex and the measurement by a tracking detector, a particle looses energy by radiating or interacting with detector material. Thus correcting for these energy losses helps to improve the momentum resolution. Since the exact amount of energy loss is unknown, an average correction is applied to the track when it is extrapolated

Table 3.3: Requirements applied on $\Lambda_b^0 \to J/\psi\,\Lambda$ candidates passing the stripping selection. All mass windows are centered on the PDG mass values [1]. The quantity $\sigma_M^{J/\psi}$ is the per-event estimate of the J/ψ mass uncertainty.

Λ requirements	
Vertex χ^2/ndf	< 20
p_{T}	$> 1000\,\mathrm{MeV}/c$
Proper time significance	> 5
Mass window	$\pm 6\,\mathrm{MeV}/c^2$

Λ_b^0 requirements	
Vertex χ^2/ndf	< 10.0
DTF χ^2/ndf	< 5.0
Decay time	$> 0.3\,\mathrm{ps}$
Mass window	$5470 - 5770\,\mathrm{MeV}/c^2$

J/ψ requirements	
Vertex χ^2/ndf	< 11
Mass window	$\pm 4.2 \times \sigma_M^{J/\psi}$

Table 3.4: Requirements applied on $\Xi_b^- \to J/\psi\,\Xi^-$, $\Xi_b^0 \to J/\psi\,\Xi(1530)^0$ and $\Omega_b^- \to J/\psi\,\Omega^-$ candidates passing the stripping selection. All mass windows are centered on the PDG mass values [1]. The quantity σ_M is the per-event estimate of the b-baryon mass uncertainty.

Λ requirements	
Proper time significance	> 0
Mass window	$\pm 6\,\mathrm{MeV}/c^2$

J/ψ requirements	
Vertex χ^2/ndf	< 10
Mass window	$\pm 4.2 \times \sigma_M^{J/\psi}$

Ξ^- or Ω^- requirements	
Vertex χ^2/ndf	< 10
Proper time significance	> 0
Mass window	$\pm 11\,\mathrm{MeV}/c^2$

b-baryon requirements	
DTF χ^2/ndf	< 4.0
Decay time	$> 0.25\,\mathrm{ps}$
σ_M	$< 14\,\mathrm{MeV}/c^2$
IP χ^2	< 16

Other requirement	
Kaon PIDK	> 5

back to its associated origin vertex using the *TrackMasterExtrapolator* algorithm. The size of the correction depends on the flight distance. This reduces the effect of the energy loss on the measured momenta and therefore on the measured masses, but some uncertainty remains.

The second correction of the measured track momenta is the momentum scale calibration. This correction is performed in a more sophisticated way for 2011 data than that for the 2010 data described in Chapter 2. The overall technique however remains the same, a corrective factor $(1 - \alpha)$ multiplying the measured momentum of each track is computed in a way that measured masses are shifted to their PDG values.

In a first step, an absolute α parameter is obtained by using the K^+ tracks of reconstructed $B^+ \to J/\psi\,K^+$ decays where the J/ψ mass is constrained to its known value. This permits to

Table 3.5: Measured Λ_b^0 and B^0 masses (in MeV/c^2) using $\Lambda_b^0 \to J/\psi \Lambda$ and $B^0 \to J/\psi K_S^0$ decays, after momentum scale calibration, obtained in 2010 data [4] and in 2011 data with *Stripping 17b*. The analysis is performed on the full sample, or on sub-samples split according to magnet polarity ("up", "down"), or to the track types used to reconstruct the Λ or K_S^0 particle ("LL" for long-long, "DD" for downstream-downstream). The first quoted error is the statistical uncertainty. The second quoted error is the leading systematic uncertainty (coming from the momentum scale uncertainty).

	2010 data [4]	2011 data (*Stripping 17b*)
Λ_b^0	$5619.19 \pm 0.70 \pm 0.30$	$5619.53 \pm 0.13 \pm 0.43$
Λ_b^0 (up)	–	$5619.49 \pm 0.20 \pm 0.43$
Λ_b^0 (down)	–	$5619.55 \pm 0.16 \pm 0.42$
Λ_b^0 (LL)	–	$5619.27 \pm 0.21 \pm 0.37$
Λ_b^0 (DD)	–	$5619.64 \pm 0.16 \pm 0.44$
B^0	$5279.58 \pm 0.29 \pm 0.33$	$5279.61 \pm 0.05 \pm 0.46$
B^0 (up)	–	$5279.44 \pm 0.08 \pm 0.47$
B^0 (down)	–	$5279.73 \pm 0.07 \pm 0.47$
B^0 (LL)	–	$5279.48 \pm 0.09 \pm 0.39$
B^0 (DD)	–	$5279.66 \pm 0.07 \pm 0.50$

use an α parameter depending only on a single track and its kinematics. The α parameter is computed in bins of the track slopes $t_x = p_x/p_z$ and $t_y = p_y/p_z$ because α is found to strongly depend on them as shown in Fig. 3.2.

In order to ensure the stability of the momentum scale, the α parameter is given an offset for different periods of data taking between which the running conditions changed. Large samples of $J/\psi \to \mu^+\mu^-$ decays are available, hence the J/ψ mass is used for the period-dependent correction of α. It has been verified that for different data-taking periods, the relative corrections for different decays do not change.

The total α parameter is of the order of $2-3$ per mille and depends, as previously described, on the data-taking period and on the slope of the considered track. To ensure that the momentum scale calibration is accurate over a wide momentum range and for all track types, a cross-check is performed where the residual α parameter is computed for several other resonances including ones reconstructed exclusively with downstream tracks. Figure 3.3 shows the residual α for several resonances after correction with the full calibration procedure described above. In an ideal case, these residual biases should all be compatible with zero. In practice, their absolute values seem to be smaller than 0.3 per mille, hence 0.3 per mille is chosen to be the uncertainty on the α parameter.

To ensure that there is no other bias as a function of the magnet polarity or the final state track type, the Λ_b^0 and B^0 masses are measured and compared to previous results. This study is summarised in Table 3.5 and it shows that all measurements are consistent.
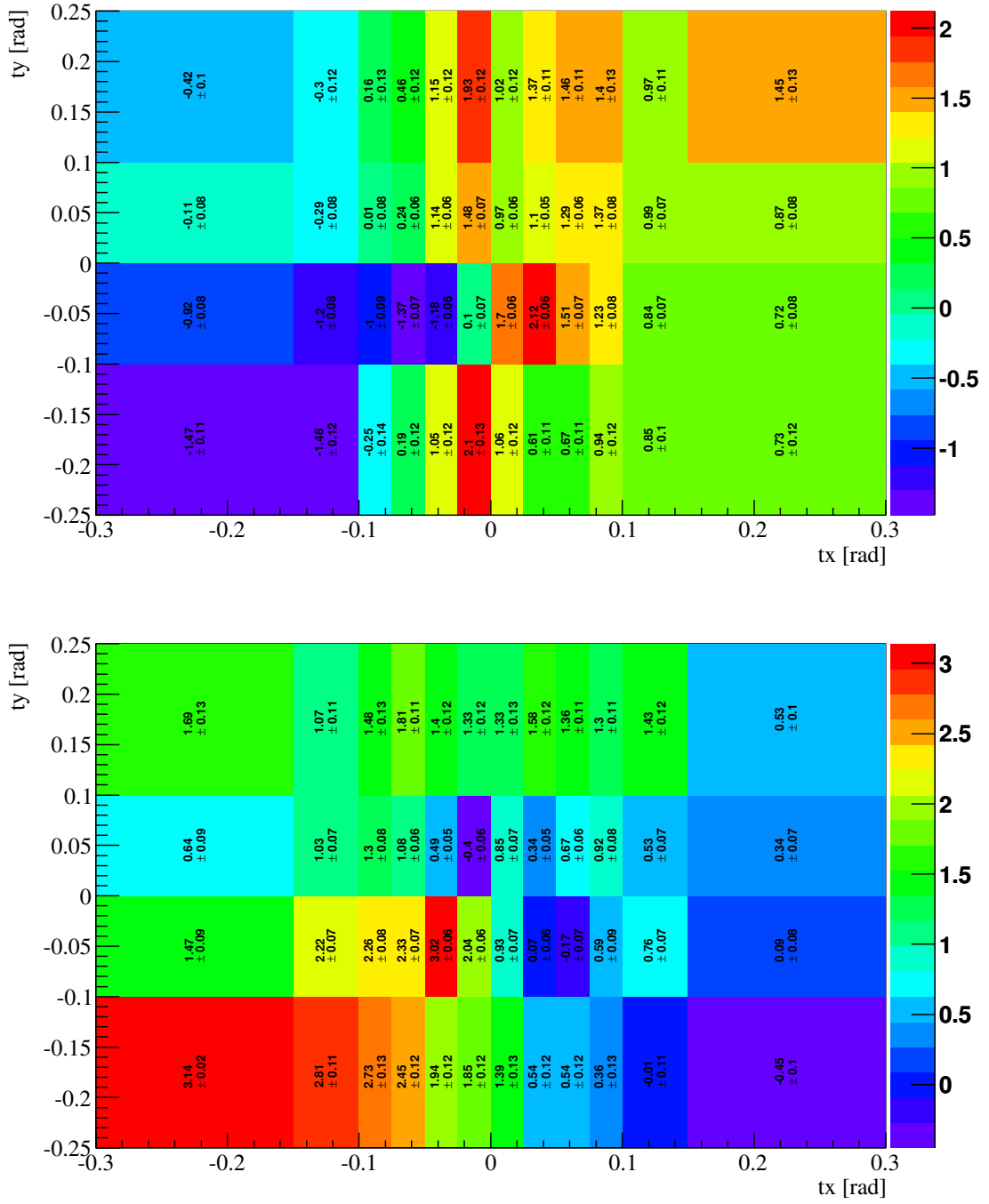
Figure 3.2: Momentum scale correction $\alpha(t_x, t_y, q, \text{polarity})$ in per mille as a function of the track slopes t_x and t_y obtained with kaons from the $B^+ \rightarrow J/\psi K^+$ decay mode for the case where the product of the kaon charge times the magnet field polarity is positive (top) or negative (bottom). To apply the correction each track momentum needs to be multiplied by $1 - \alpha(t_x, t_y, q, \text{polarity})$.
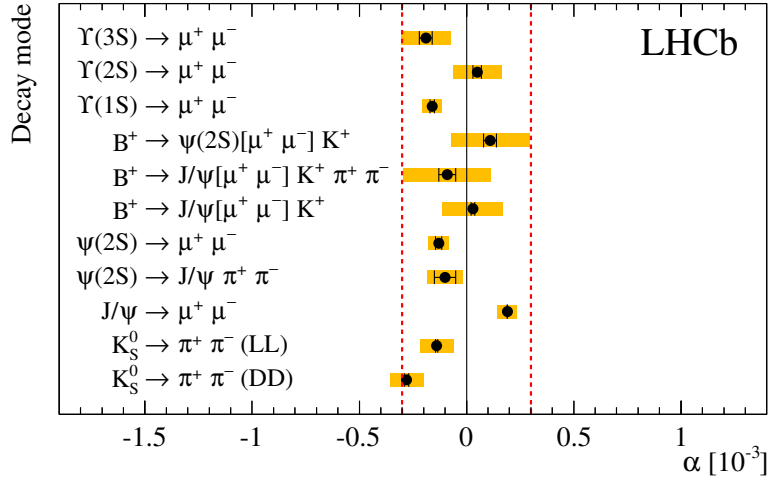
Figure 3.3: Remaining momentum scale bias α, extracted from the reconstructed mass of various decay modes after the full period- and track-slope-dependent calibration procedure described in the text. The black error bars represent the statistical uncertainty whilst the yellow filled areas also include contributions to the systematic uncertainty from the fitting procedure, the effect of QED radiative corrections, and the uncertainty quoted by the PDG [1] on the mass of the decaying meson. The weighted average of all the measurements, ignoring correlations, is $\alpha = -0.06 \pm 0.02$ per mille. The K_S^0 candidates are divided into two categories: K_S^0 candidates built with long tracks (LL) and with downstream tracks (DD).

3.4 Mass fit

The calculation of the b-baryon masses is performed with the *DecayTreeFitter* tool [76] where the masses of all hyperons (Λ, Ξ^- and Ω^-) and of the J/ψ meson are constrained to their PDG values. This helps reducing by a factor two the widths of the reconstructed b-baryon mass distributions. The b-baryon candidates are also constrained to originate from their associated PV.

An unbinned maximum likelihood fit is performed on the resulting reconstructed mass distributions. The fit has two components: one for the signal and one for the background. The signal component is a single (double) Gaussian function for Ξ_b^-, Ξ_b^0, Ω_b^- (Λ_b^0) and the background component is an exponential function. The mean of the Gaussian function is left free and in the case of the Λ_b^0 the two means are constrained to have the same free value. The width(s) of the Gaussian function(s) is (are) left free for Ξ_b^- (Λ_b^0). For Ξ_b^0 and Ω_b^-, the Gaussian width is fixed to the one measured with Ξ_b^- multiplied by the appropriate ratio extracted from MC simulated events. The values are fixed to permit the fit to converge despite the limited statistics available. The mass resolutions and ratios obtained from simulation are summarised in Table 3.6.

To try to avoid fixing the width of the Gaussian function describing the Ω_b^- signal component, a simultaneous fit of the Ξ_b^- and Ω_b^- is performed where both widths are left free but their ratio

Table 3.6: Monte Carlo mass resolutions and their ratios. The uncertainties are statistical.

Decay mode	σ_M^{MC} (MeV/c^2)	$\sigma_M^{\text{MC}}/\sigma_{M(\Lambda_b^0)}^{\text{MC}}$	$\sigma_M^{\text{MC}}/\sigma_{M(\Xi_b^-)}^{\text{MC}}$
$\Lambda_b^0 \to J/\psi\,\Lambda$	8.38 ± 0.13	1	
$\Xi_b^- \to J/\psi\,\Xi^-$	8.86 ± 0.06	1.057 ± 0.017	1
$\Xi_b^0 \to J/\psi\,\Xi(1530)^0$	8.17 ± 0.15	0.975 ± 0.025	0.922 ± 0.020
$\Omega_b^- \to J/\psi\,\Omega^-$	8.16 ± 0.08	0.974 ± 0.020	0.921 ± 0.012

Table 3.7: Results of the fits to the invariant mass distributions of Fig. 3.4. The quoted uncertainties are statistical.

Decay mode	Signal yield	Mass (MeV/c^2)	Width (MeV/c^2)
$\Lambda_b^0 \to J/\psi\,\Lambda$	6870 ± 110	5619.53 ± 0.13	$\sigma_1 = 6.37 \pm 0.46$ $\sigma_2 = 12.5 \pm 1.3$ $f_1 = 1 - f_2 = 0.58 \pm 0.11$
$\Xi_b^- \to J/\psi\,\Xi^-$	111 ± 12	5795.76 ± 0.88	7.77 ± 0.70
$\Xi_b^0 \to J/\psi\,\Xi(1530)^0$	$3.2^{+2.4}_{-1.7}$	5790.6 ± 4.3	7.16 (fixed)
$\Omega_b^- \to J/\psi\,\Omega^-$	19.1 ± 4.8	6046.0 ± 2.2	7.16 (fixed)

fixed to the corresponding value in simulation. The result of this fit gives a larger statistical uncertainty on the mass measurement (0.89 MeV/c^2 and 2.3 MeV/c^2 instead of 0.88 MeV/c^2 and 2.2 MeV/c^2 for Ξ_b^- and Ω_b^- respectively). The contribution to the systematic uncertainty due to the fixed width of the Gaussian function describing the mass distribution of the Ω_b^- signal is ten times smaller than the statistical uncertainty, as shown in Section 3.6. Therefore the total uncertainty is larger in the case of a simultaneous fit and this option is abandoned.

The fit ranges are 5.5–5.75 GeV/c^2, 5.6–6.0 GeV/c^2, 5.6–6.0 GeV/c^2 and 5.8–6.3 GeV/c^2 for Λ_b^0, Ξ_b^-, Ξ_b^0 and Ω_b^- respectively. The four mass distributions and the result of the fits are shown on Fig. 3.4. The values of the signal fit parameters are given in Table 3.7.

3.5 Likelihood scans and statistical significance

The significances of the Λ_b^0 and Ξ_b^- mass peaks are large and do not need to be estimated. However the Ξ_b^0 and Ω_b^- signals need their significance to be calculated. Fixing the number of signal events to zero and repeating the fit gives a different likelihood ($\mathscr{L}_0$) than when the number of signal events is free ($\mathscr{L}_{\max}$). The log-likelihood difference between the two scenarios is 2.7 and 23 for Ξ_b^0 and Ω_b^- respectively. A naive calculation assuming that the significance is equal to $\sqrt{2\ln(\mathscr{L}_{\max}/\mathscr{L}_0)}$ results in significances of 2.3 σ and 6.5 σ respectively. To illustrate at first sight the significance of each channel, so-called likelihood scans for the number of signal events are given in Fig. 3.5. These scans show the calculated log-likelihood
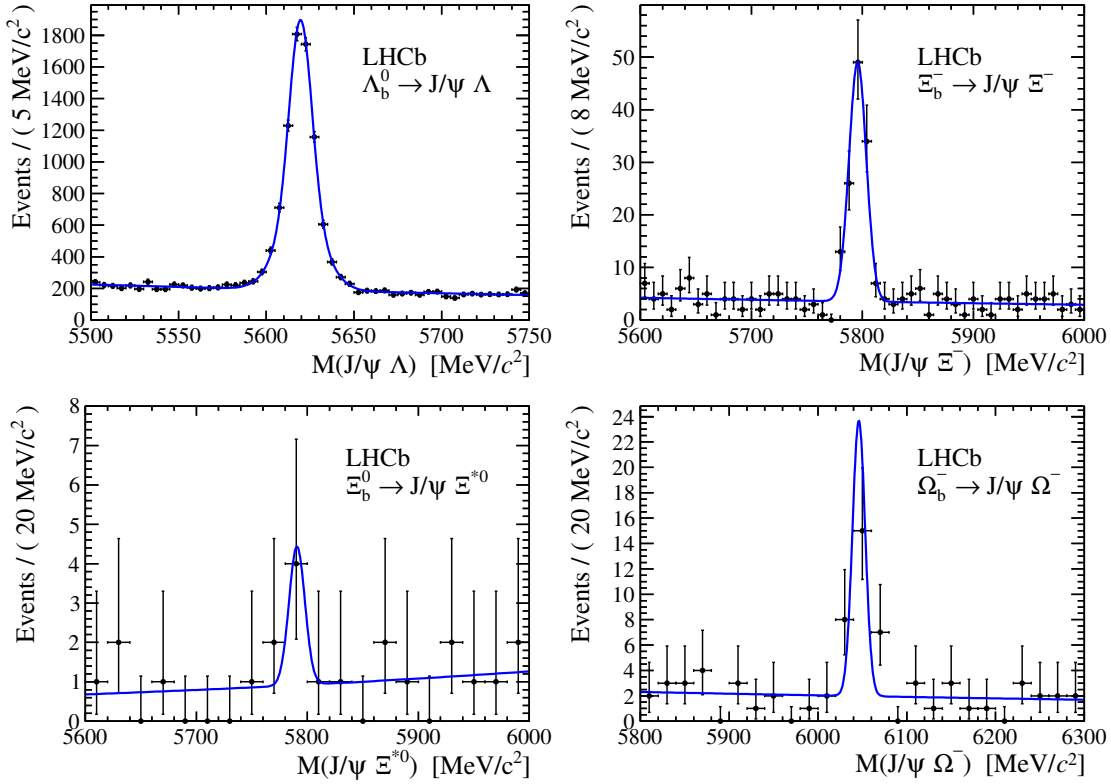
Figure 3.4: Invariant mass distributions of $\Lambda_b^0 \to J/\psi\,\Lambda$, $\Xi_b^- \to J/\psi\,\Xi^-$, $\Xi_b^0 \to J/\psi\,\Xi(1530)^0$, and $\Omega_b^- \to J/\psi\,\Omega^-$ candidates. The results of the unbinned extended maximum likelihood fits are overlaid.
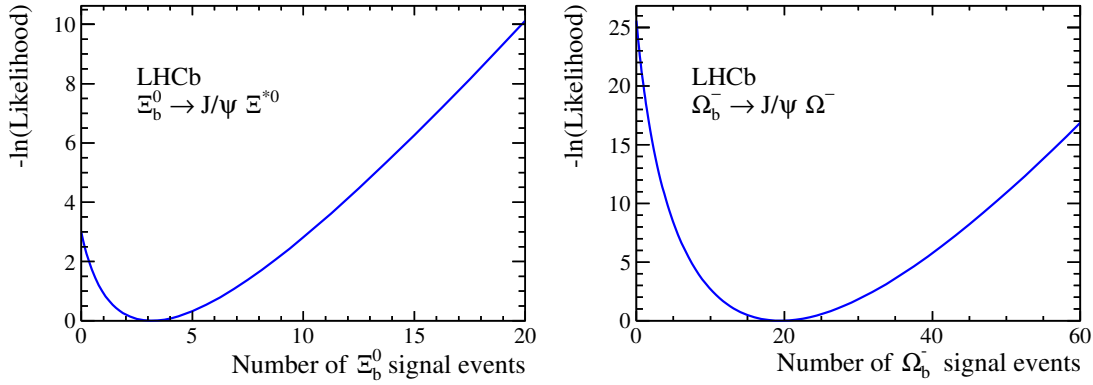
Figure 3.5: Likelihood scan of the number of signal events of Ξ_b^0 (left) and Ω_b^- (right).

of the fit function that has all parameters fixed to the fitted values except the considered parameter which is fixed to each value of the scan.

The significance of the Ξ_b^0 signal, being definitely below 3 σ, is not studied further. However a more complete look is given to the one of the Ω_b^- in order to take into account the *look elsewhere effect* [78].
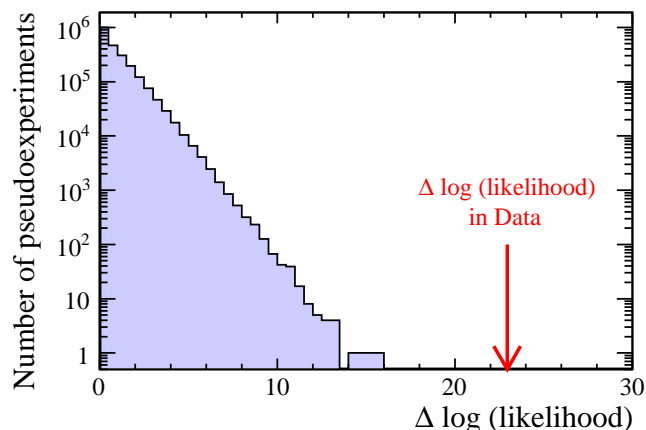
Figure 3.6: The distribution of the negative log-likelihood difference in 2.5 million Ω_b^- pseudo-experiments with background only. The red arrow corresponds to the value observed in data.

Mass distributions are generated using the nominal Ω_b^- fit function as probability density function. The parameters of the fit are fixed to the values fitted in data with the exception of the signal yield kept at zero. These distributions are pseudo-experiments in the sense that they are other possible outcomes that could have been observed in data under the hypothesis that there is no signal to be observed and that the fit function with its parameters perfectly describes the underlying background mass distribution. A total of 2.5 M pseudo-experiments with background only are generated and fitted with the nominal fit model. On Fig. 3.6, the negative log-likelihood difference with respect to the fit with no signal component is plotted and it appears that it never reaches the value observed in data (23). The distribution is exponential and when performing an extrapolation it appears that around one generated distribution out of 10^{10} would reach the log-likelihood difference observed in data. This leads to an estimate of the statistical significance of the observed Ω_b^- signal equal to $6.5\,\sigma$ consistent with the naive calculation.

3.6 Systematic uncertainties

The mass fit is repeated by varying in turn each parameter within its assigned uncertainty. The difference between the measured mass obtained from this fit and the one from the nominal fit is taken as the systematic uncertainty corresponding to the varied parameter. The systematic uncertainties on mass differences are studied in a similar way. A summary of all systematic uncertainties is given in Table 3.8. For the mass differences, only the systematic uncertainties related to the energy loss correction are assumed fully correlated among the different channels. The systematic uncertainty related to the momentum scale is propagated to the mass differences and the other systematic uncertainties are assumed to be uncorrelated.

In the analysis presented here the systematic uncertainty on the Λ_b^0 mass is larger than the systematic uncertainty of the 2010 data result [4]. This is due to the fact that the alignment

Table 3.8: Systematic uncertainties (in MeV/c^2) on the mass measurements and on their differences.

| Source of uncertainty | Systematic uncertainty on | | | | | | |
| | masses | | | | mass differences | | |
	Λ_b^0	Ξ_b^-	Ξ_b^0	Ω_b^-	$\Xi_b^- - \Lambda_b^0$	$\Xi_b^0 - \Lambda_b^0$	$\Omega_b^- - \Lambda_b^0$
Average momentum scale	0.43	0.43	0.31	0.31	0.01	0.12	0.12
Energy loss correction[a]	0.09	0.09	0.09	0.09	< 0.01	< 0.01	< 0.01
Hyperon mass constraint	0.01	0.07	0.06	0.25	0.07	0.06	0.25
Signal model	0.07	0.01	0.09	0.24	0.07	0.12	0.25
Background model	0.01	0.01	0.01	0.02	0.01	0.01	0.02
Quadratic sum	0.45	0.45	0.34	0.47	0.10	0.18	0.37

[a] The systematic uncertainties on the mass values are taken from the value for Λ_b^0 in the studies of Ref. [4] and are assumed to be fully correlated.

strategy changed and fewer degrees of freedom are aligned as described in Chapter 2 leading to a larger uncertainty on the momentum scale.

3.6.1 Momentum scale calibration

An uncertainty of ±0.3 per mille is assigned to the α parameter of the momentum scale as described in Sec. 3.3. By applying an α parameter varied by 0.3 per mille to all final state tracks, recomputing the masses and fitting gives a different mass measurement for each channel. The difference between this value and the nominal measurement is taken as the systematic uncertainty due to the momentum scale.

The limited knowledge of the detector alignment gives a large contribution to the momentum scale uncertainty. Especially the detector length scale, known with a precision of 10^{-3} [79], is expected to heavily contribute. Varying the scale within its uncertainty by manually changing the horizontal and vertical slopes of the tracks by 10^{-3} in the reconstruction shows an average change in α of ±0.13 per mille. This is covered by the uncertainty assigned on α giving confidence in the estimation of this uncertainty.

The systematic uncertainty related to the momentum scale is the largest for all absolute mass measurements. However, this uncertainty largely cancels in mass difference measurements.

3.6.2 Energy loss corrections

Energy lost by radiation and interaction with detector material is compensated in the reconstruction with an average estimate, however there remains an uncertainty. The estimate of the effect on the mass measurements coming from this remaining uncertainty is based on the study performed in Ref. [4] where the energy loss corrections are varied by ±10% in the

reconstruction. In addition these systematic uncertainties are assumed to be fully correlated between the different mass measurements.

3.6.3 Hyperon mass constraint

The mass constraint applied to the J/ψ and hyperon candidates reduces the width of the mass distribution and increases therefore the statistical power of the result. However, there is an uncertainty emerging from the limited knowledge of the masses that are constrained. Especially the Ω^- mass is known with a limited precision which affects the Ω_b^- mass measurement presented here.

The uncertainty on the Λ, Ξ^- and Ω^- masses is propagated analytically to the b-baryon masses. The square of the reconstructed mass m_b as a function of the J/ψ and the hyperon masses ($m_{J/\psi}$ and m_h respectively) and momenta ($\vec{p}_{J/\psi}$ and $\vec{p}_h$ respectively) is given by the expression

$$m_b^2 = m_{J/\psi}^2 + m_h^2 + 2\sqrt{(m_{J/\psi}^2 + p_{J/\psi}^2)(m_h^2 + p_h^2)} - 2\vec{p}_{J/\psi} \cdot \vec{p}_h. \tag{3.1}$$

The expression of the uncertainty on the b-baryon mass $\sigma(m_b)$ as a function of the uncertainty on the hyperon mass $\sigma(m_h)$ depends on the ratio of the energies between the J/ψ ($E_{J/\psi}$) and the hyperon (E_h) as follows:

$$\sigma(m_b) = \left|\frac{\partial m_b}{\partial m_h}\right| \cdot \sigma(m_h) = \frac{m_h}{m_b}\left(1 + \frac{E_{J/\psi}}{E_h}\right) \cdot \sigma(m_h). \tag{3.2}$$

The *sPlot* technique is used to obtain the energy distributions of signal in data and the average value is taken for the calculation. The uncertainty on the J/ψ mass is neglected because the effect is small compared to the one arising from the hyperon mass uncertainty.

An additional study is performed to motivate the use of the hyperon mass constraints in the case of the Ξ_b^- and the Ω_b^-. In the absence of this mass constraint, the resolution of the Gaussian function describing the signal increases from 7.77 MeV/c^2 (7.16 MeV/c^2) to 8.73 MeV/c^2 (7.60 MeV/c^2) for Ξ_b^- (Ω_b^-). Performing the nominal fit on the mass distribution without the hyperon mass constraint in data increases the statistical uncertainty on the measured mass from ± 0.88 MeV/c^2 (± 2.2 MeV/c^2) to ± 1.02 MeV/c^2 (± 2.3 MeV/c^2) for Ξ_b^- (Ω_b^-). In both cases the total uncertainty is larger without the hyperon mass constraint.

3.6.4 Signal modeling

For each b baryon, one or more alternative signal models are used in the fit and the maximal change in the measured mass is taken as the systematic uncertainty on the signal model.

One alternative model is to constrain each of the two Gaussian functions used in the fit of the Λ_b^0 mass distribution to describe either the LL or the DD component. The mean of both Gaussian functions is forced to be the same and both widths are left free. The change in the measured mass with respect to the nominal fit is less than 0.01 MeV/c^2. Another model which is the sum of two *Crystal Ball* functions [80] is used to take into account the radiative tail from the J/ψ decay which might propagate to the invariant Λ_b^0 mass. The mean is again set to the same value for both components and all other parameters left free. The expected change from MC studies is 0.05 MeV/c^2 and the one measured in data is 0.07 MeV/c^2. Hence the uncertainty on the signal model for the Λ_b^0 channel is taken to be 0.07 MeV/c^2.

In the case of the Ξ_b^- baryon, the fit is repeated once with the sum of two Gaussian functions with common mean and free width and once with a single *Crystal Ball* function with all parameters left free. The change between the mass fitted with these functions and the nominal one is less than 0.01 MeV/c^2.

The largest uncertainty on the Ξ_b^0 and Ω_b^- signal models comes from the uncertainty on the fixed width of the Gaussian function. As previously described, the width is the product of the Ξ_b^- width and the appropriate width ratio extracted from simulation. Hence to compute the uncertainty on the fixed width, both contributions from the uncertainty on the Ξ_b^- width as well as the uncertainty on the ratio from simulation are summed in quadrature. The uncertainty contribution from the Ξ_b^- width is taken as the statistical error on the Ξ_b^- width given by the fit multiplied by the appropriate width ratio. Since the ratios are almost identical for Ξ_b^0 and Ω_b^-, this contribution is the same for both and equals ± 0.64 MeV/c^2. The uncertainty due to the ratio extracted from simulation is estimated by calculating the fixed width using the Λ_b^0 instead of the Ξ_b^-. By multiplying the measured Λ_b^0 width in data and the appropriate MC ratio, the calculated Ω_b^- and Ξ_b^0 widths vary by less than 10% with respect to the Ξ_b^- case. Therefore the ratio is assumed to be known with a precision of 10%. Changing the ratio by 10% leads to a change in the fixed width of ± 0.72 MeV/c^2 in both cases. The total uncertainty on the fixed width is therefore ± 0.96 MeV/c^2. Finally the effect of the uncertainty on the fixed width on the mass measurement is computed. This is done by varying the fixed width by $+$ and $-$ its error and taking the largest difference in the measured mass with respect to the nominal value as the systematic uncertainty related to the signal model.

3.6.5 Background modeling

For all channels the same alternative background model, a linear function instead of an exponential one, is used. The fitted mass is only changed by a negligible amount of less than 0.01 MeV/c^2. In order to also take into account the effect on the background estimate of the

fitting range, the latter is changed to 5.65–5.95 GeV/c^2, 5.4–6.2 GeV/c^2 and 5.90–6.20 GeV/c^2 for Ξ_b^-, Ξ_b^0 and Ω_b^- respectively. The change in the fitted mass value is taken as the systematic uncertainty related to the background model.

The background in the Ω_b^- mass distribution seems to present a slight excess in the lower third. To quantify the effect of this excess, an *ARGUS* function [81] that has all parameters left free is added to the background model in the fit. The difference between the mass obtained with this alternative function and the nominal result is added as a contribution to the systematic uncertainty on the Ω_b^- mass.

3.7 Results

The final results of the absolute mass measurements for the significantly observed b baryons are

$$M(\Lambda_b^0) = 5619.53 \pm 0.13 \text{ (stat)} \pm 0.45 \text{ (syst) MeV/}c^2,$$
$$M(\Xi_b^-) = 5795.8 \pm 0.9 \text{ (stat)} \pm 0.4 \text{ (syst) MeV/}c^2,$$
$$M(\Omega_b^-) = 6046.0 \pm 2.2 \text{ (stat)} \pm 0.5 \text{ (syst) MeV/}c^2.$$

These are the most precise mass measurements of these weakly decaying b-baryons to date. The Λ_b^0 measurement is in good agreement with the world average [1] and the Ξ_b^- is in agreement with the world average [1] at the 1.9 σ level. The Ω_b^- measurement is in agreement with the CDF measurement [7] and in disagreement with the D0 one [9]. Excluding the Ω_b^- mass measurement from D0 yields a new world average improved by a factor almost 20. A visual summary of all experimental determinations of the Λ_b^0, Ξ_b^- and Ω_b^- baryons is given in Fig. 3.7.

Each of the three mass measurements is in good agreement with the corresponding most precise theoretical prediction given in Table 1.3. The total uncertainties of the LHCb measurements are smaller than the uncertainties of the most accurate theoretical predictions. The mass differences with respect to the measured Λ_b^0 mass, in which the systematic uncertainties largely cancel, are

$$M(\Xi_b^-) - M(\Lambda_b^0) = 176.2 \pm 0.9 \text{ (stat)} \pm 0.1 \text{ (syst) MeV/}c^2,$$
$$M(\Omega_b^-) - M(\Lambda_b^0) = 426.4 \pm 2.2 \text{ (stat)} \pm 0.4 \text{ (syst) MeV/}c^2.$$
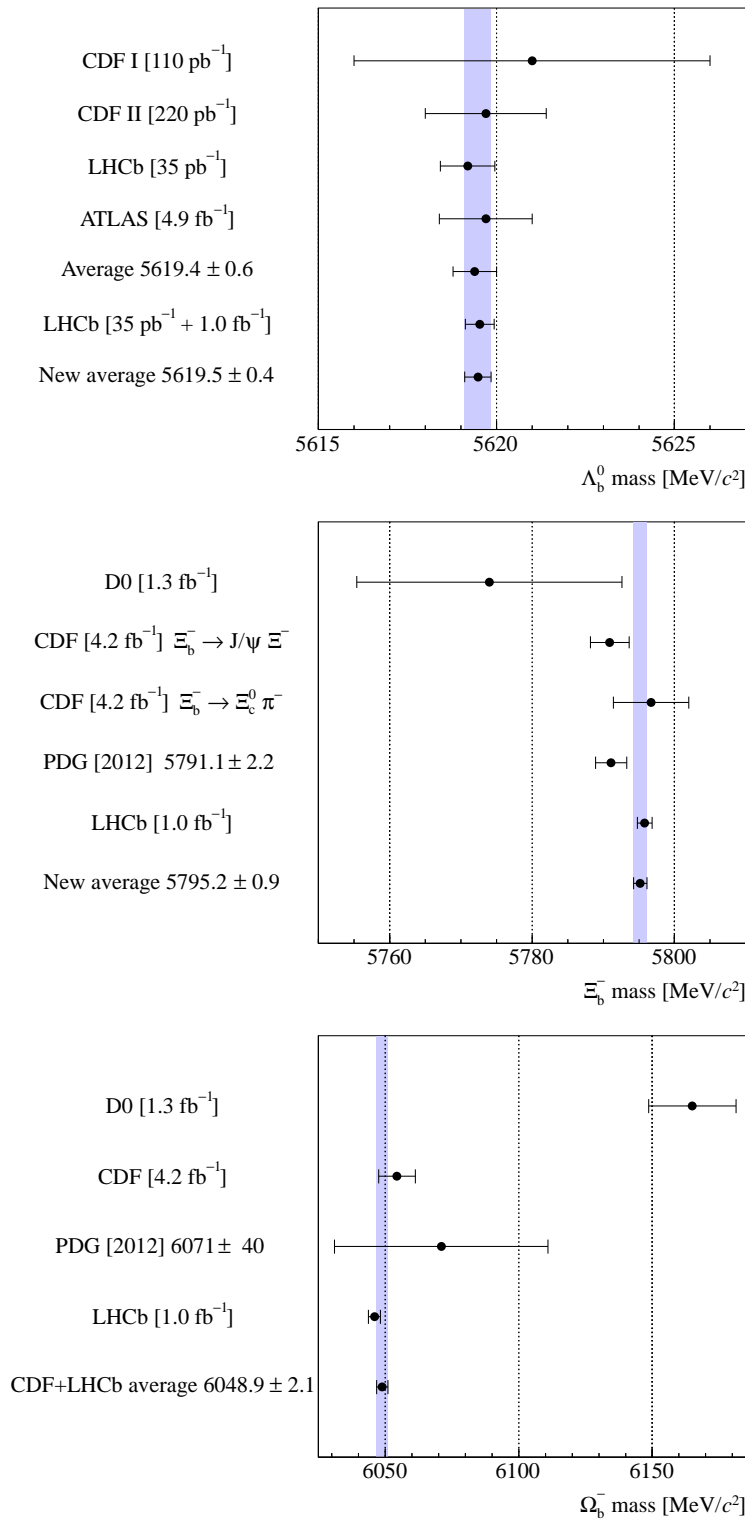
Figure 3.7: Measurements of the Λ_b^0 (top left), Ξ_b^- (top right) and Ω_b^- (bottom) masses. The new averages are performed using the PDG prescription [1] which is a standard weighted least-squares procedure assuming all measurements to be uncorrelated. The Λ_b^0 measurements are reported from Refs. [2–5], the Ξ_b^- measurements from Refs. [1, 6–8] and the Ω_b^- measurements from Refs. [1, 7, 9].

The LHCb mass measurement of the Λ_b^0 baryon performed with data from the 2010 run [4] was $M(\Lambda_b^0) = 5619.19 \pm 0.70\,(\text{stat}) \pm 0.30\,(\text{syst})\,\text{MeV}/c^2$. The data taking conditions (alignment, momentum scale calibration, etc.) were completely different and independent between the 2010 and 2011 runs. Hence the systematic uncertainties, with the exception of the one related to the energy loss corrections, are assumed to be totally uncorrelated. The weighted average of the 2010 result with the 2011 one is

$$M(\Lambda_b^0) = 5619.44 \pm 0.13\,(\text{stat}) \pm 0.38\,(\text{syst})\,\text{MeV}/c^2.$$

The $\Xi_b^0 \to J/\psi\, \Xi(1530)^0$ decay mode is seen in 2011 data with a significance of approximately $2.3\,\sigma$ and the Ξ_b^0 mass and its difference with respect to the Λ_b^0 mass are measured to be

$$
\begin{aligned}
M(\Xi_b^0) &= 5790.6 \pm 4.3\,(\text{stat}) \pm 0.3\,(\text{syst})\,\text{MeV}/c^2, \\
M(\Xi_b^0) - M(\Lambda_b^0) &= 171.1 \pm 4.3\,(\text{stat}) \pm 0.2\,(\text{syst})\,\text{MeV}/c^2.
\end{aligned}
$$

This result is more precise and in good agreement with the published CDF measurement using $\Xi_b^0 \to \Xi_c^+ \pi^-$ [8] that yields $5787.8 \pm 5.0\,(\text{stat}) \pm 1.3\,(\text{syst})\,\text{MeV}/c^2$ and with their preliminary result [42, 43] of $5791.6 \pm 5.0\,(\text{stat}) \pm 0.73\,(\text{syst})\,\text{MeV}/c^2$.

An article about the Λ_b^0, Ξ_b^- and Ω_b^- mass measurements was published in the journal *Physical Review Letters* [40]. The Ξ_b^0 result remains unpublished due to the low significance of the signal.

3.8   Observation of $\Xi_b^0 \to J/\psi\, \Xi^- \pi^+$ in the 2011 and 2012 data sets

A preliminary search for the decay $\Xi_b^0 \to J/\psi\, \Xi^- \pi^+$ is performed on the complete data set recorded in 2011 and 2012 corresponding to a total integrated luminosity of $3.0\,\text{fb}^{-1}$. Like in the previous analysis the reconstructed sub-decays are $J/\psi \to \mu^+ \mu^-$ and $\Xi^- \to \Lambda \pi^-$ where the Λ decays into $p\pi^-$. The purpose of this study is to estimate the significance of the signal in order to motivate further studies. No momentum scale calibration is applied in this case and no systematic uncertainties are considered. A full analysis of this decay mode requires more time than available to carry out this thesis.

The candidates are built with version 20 of the stripping. In this version the cut on the invariant $\Xi^- \pi^+$ mass is removed allowing the non-resonant contribution. However, removing this cut increases the amount of combinatorial background by a factor between five and six. Therefore the offline selection used for the mass measurements with 2011 data is tightened. The requirement on the Ξ_b^0 decay time is increased to $> 1.0\,\text{ps}$. In addition it seems that a physics background from the decay $\Lambda_b^0 \to J/\psi\, \Lambda \pi^- \pi^+$ is peaking in the mass distribution. This contribution is removed by requiring the Ξ^- decay length significance to be larger than 3.
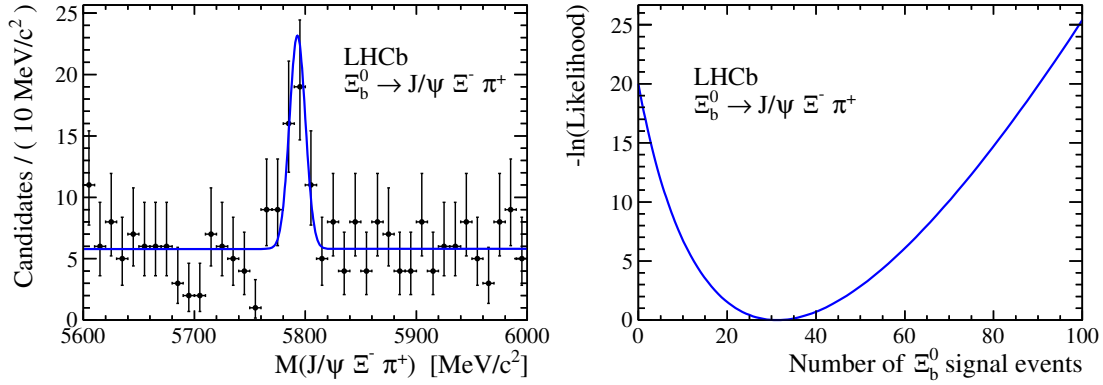
Figure 3.8: Left: Invariant mass distribution of $\Xi_b^0 \to J/\psi\, \Xi^- \pi^+$ candidates reconstructed in the full data set of 3.0 fb^{-1}. The result of the unbinned extended maximum likelihood fit is overlaid. Right: Likelihood scan of the number of Ξ_b^0 signal events.

As for the b-baryon mass measurements, the invariant mass of the Ξ_b^0 candidates is computed by a refit of the whole decay chain where the J/ψ as well as the Ξ^- masses are constrained to their respective PDG averages [1]. An unbinned maximum likelihood fit is performed on the invariant mass distribution where the signal is modeled with a single Gaussian function and the background with an exponential function. The width of the Gaussian function is fixed to the value obtained in the previous analysis. All other parameters are allowed to vary in the fit. Figure 3.8 shows the invariant mass distribution and the overlaid fit result. A list of some fitted variables are given in Table 3.9.

The significance of the Ξ_b^0 signal is obtained with the naive calculation described in Sec. 3.5. The log-likelihood difference between the fit with and without a signal component is found to be 18.0. Hence, from a naive perspective, the significance of the observed Ξ_b^0 signal is 6.0 standard deviations.

Since the momentum scale calibration is not applied, the mean of the fitted Gaussian function is biased by an unknown amount. However, the uncertainty on the mean returned by the fit is meaningful as it will not vary significantly when the momentum scale corrections are applied. Therefore the expected precision of a mass measurement that would be performed with this

Table 3.9: Results of the fit to the invariant mass distribution of Fig. 3.8 (left). The quoted uncertainties are statistical.

Parameter	Value
Signal yield	31 ± 7
Signal mean mass	$[\ldots] \pm 2.0$ MeV/c^2
Signal width	7.16 MeV/c^2 (fixed)
Background yield	232 ± 16

data is ± 2.0 MeV/c^2. If a momentum scale correction is applied, the systematic uncertainty is expected to be of the same order of magnitude than for the mass measurements with 2011 data. Hence the expected total uncertainty on a Ξ_b^0 mass measurement performed with 2011 and 2012 data is significantly lower than the currently most precise determination of the Ξ_b^0 mass by CDF (± 5.1 MeV/c^2) [8].

4 Lifetime measurements of Ξ_b^- and Ω_b^-

The previous chapter describes the significant Ξ_b^- and Ω_b^- signals observed with the first 1.0 fb^{-1} of LHCb data and how the masses of these baryons are measured. The same data is used to measure the lifetimes of several b hadrons [41]. The result of these measurements are

$$
\begin{aligned}
\tau_{B^+ \to J/\psi\, K^+} &= 1.637 \pm 0.004 \text{ (stat)} \pm 0.003 \text{ (syst) ps,} \\
\tau_{B^0 \to J/\psi\, K^{*0}} &= 1.524 \pm 0.006 \text{ (stat)} \pm 0.004 \text{ (syst) ps,} \\
\tau_{B^0 \to J/\psi\, K_S^0} &= 1.499 \pm 0.013 \text{ (stat)} \pm 0.007 \text{ (syst) ps,} \\
\tau_{\Lambda_b^0 \to J/\psi\, \Lambda} &= 1.415 \pm 0.027 \text{ (stat)} \pm 0.006 \text{ (syst) ps,} \\
\tau^{\text{eff}}_{B_s^0 \to J/\psi\, \phi} &= 1.480 \pm 0.011 \text{ (stat)} \pm 0.005 \text{ (syst) ps.}
\end{aligned}
$$

This chapter presents absolute lifetime measurements of the Ξ_b^- and Ω_b^- baryons performed with the full 3.0 fb^{-1} of recorded data. This analysis strongly benefits from the expertise and the techniques elaborated for the above-mentioned b-hadron lifetime analysis with 2011 data. Since the Λ_b^0 is reconstructed in a mode with a topology similar to those of the Ξ_b^- and Ω_b^-, its lifetime is also measured with the same technique as a cross-check of the methodology. The channels in which the b baryons are reconstructed are the same as those of the mass measurements: $\Xi_b^- \to J/\psi\, \Xi^-$, $\Omega_b^- \to J/\psi\, \Omega^-$ and $\Lambda_b^0 \to J/\psi\, \Lambda$ where the daughters are reconstructed in the $J/\psi \to \mu^+\mu^-$, $\Xi^- \to \Lambda\pi^-$, $\Omega^- \to \Lambda K^-$ and $\Lambda \to p\pi^-$ modes.

4.1 Data samples

This analysis is based on the data sets recorded in 2011 and 2012. The total integrated luminosity is 3.0 fb^{-1} of pp collisions with a centre-of-mass energy of $\sqrt{s} = 7$ TeV in 2011 (1.0 fb^{-1}) and $\sqrt{s} = 8$ TeV in 2012 (2.0 fb^{-1}). All events are reconstructed with *Reco14* and pre-selected

Table 4.1: Simulated data samples and conditions. The event type is a unique LHCb-internal identifier for each decay.

Decay	Event type	Generated lifetime	*MC2011* events	*MC2012* events
$\Lambda_b^0 \to J/\psi\, \Lambda$	15144103	1.425 ps	1M	2M
$\Xi_b^- \to J/\psi\, \Xi^-$	16145133	1.567 ps	4M	4M
$\Omega_b^- \to J/\psi\, \Omega^-$	16145134	1.390 ps	4M	4M

with dedicated lines in *Stripping20*.

An essential ingredient to this analysis are the simulated samples. Several million events of the considered decays are generated by the official LHCb simulation production group. Both 2011 and 2012 data taking conditions are simulated and the respective data types are called *MC2011* and *MC2012*. In order to mimic the recorded data, half of the events are simulated with a positive magnet polarity and half with a negative one. The versions of the reconstruction and selection algorithms are the same than for the recorded data samples. A summary of all simulated samples used in this analysis is given in Table 4.1.

4.2   Trigger, stripping and selection

Only events that fire HLT1 lines Hlt1DiMuonHighMass or Hlt1TrackMuon and that fire HLT2 line Hlt2DiMuonDetachedJpsi on signal tracks are considered. The requirement that the signal tracks (rather than other tracks in the event) fire the trigger line is called the *Trigger On Signal* (TOS) requirement. The chosen HLT1 lines require the events to fire either of the two L0 lines L0Muon or L0DiMuon. The requirements of all the L0, HLT1 and HLT2 lines used in this analysis are listed in Table 4.2.

Due to their requirements on the IP χ^2 of some final state tracks and on the decay length significance (DLS) of the b baryon, the two lines Hlt1TrackMuon and Hlt2DiMuonDetachedJpsi have an efficiency which depends on the b-baryon decay time and are therefore called *lifetime biased* lines. On the other hand, the selection criteria of the line Hlt1DiMuonHighMass have no effect on the b-baryon decay-time distribution and this line is therefore called *lifetime unbiased*. The biases due to the trigger requirements mainly affect the events with a low decay time and they are taken into account in the lifetime measurements as described in Sec. 4.3.1.

The stripping lines used in the lifetime analysis are identical to the ones of the mass measurements described in Sec. 3.2. They also bias the measured lifetime, especially for candidates with a long decay time, and this is taken into account with the technique described in Sec. 4.3.2.

After having been pre-selected by the stripping, the events undergo a set of final selection cuts, also called offline selection. The understanding of the quantities on which the requirements are applied improved in the period between the mass and the lifetime measurements. Espe-

Table 4.2: L0 trigger (top), HLT1 (middle) and HLT2 (bottom) requirements. DLS stands for the decay length significance of the J/ψ candidate with respect to the best PV. The scale factor of 0.2 in trigger line Hlt2DiMuonJpsi means that only 20% of the events satisfying the other criteria are randomly selected to fire the line.

L0Muon		L0DiMuon	
SPD hit multiplicity	< 600	SPD hit multiplicity	< 900
Muon p_T	> 1480 MeV/c	Muon1 p_T × Muon2 p_T	$> 1'680'000$ MeV^2/c^2

Hlt1DiMuonHighMass (unbiased)		Hlt1TrackMuon (biased)	
Passed L0Muon or L0DiMuon			
Muons have hits in VELO, T stations and muon chambers			
Muon p_T	> 500 MeV/c	Muon p_T	> 1000 MeV/c
Muon p	> 6000 MeV/c	Muon p	> 8000 MeV/c
Track χ^2/ndf	< 4	Track χ^2/ndf	< 2
J/ψ mass	> 2700 MeV/c^2	Muon IP	> 0.1 mm
		Muon IP χ^2	> 16

Hlt2DiMuonDetachedJpsi (biased)		Hlt2DiMuonJpsi (unbiased, prescaled)	
J/ψ vertex χ^2/ndf	< 25	J/ψ vertex χ^2/ndf	< 25
Track χ^2/ndf	< 5	Track χ^2/ndf	< 5
J/ψ mass window	± 120 MeV/c^2	J/ψ mass window	± 120 MeV/c^2
DLS	> 3	Scale	0.2

cially the extensive effort on the signal optimization of the channel $B_s^0 \to J/\psi K^+ K^-$ used to measure the CP-violating phase ϕ_s [82] contributed to this improved understanding. Hence the present offline selection is slightly revised compared to the one presented in Sec. 3.2. In particular the new understanding of the vertex and IP χ^2 distributions suggests the corresponding cuts to be slightly relaxed.

In order to reduce lifetime biases, a few additional cuts are applied. A bias can result from wrongly-associated primary vertices (PV). Hence the IP χ^2 of the b baryon with respect to the next-best associated PV is required to be larger than 50. The next-best associated PV is defined as the PV that gives the second smallest b-baryon IP χ^2. Another bias results from the geometrical VELO acceptance as seen by the b-baryon daughter particles. This heavily depends on the position of the PV along the z axis. This effect is taken into account by a procedure based on simulated events described in Sec. 4.3.2. However, it is known that the simulation does not generate pp collisions as far from the nominal interaction point as what is actually happening at LHCb. Hence a cut on the z coordinate of the PV associated to the b baryon is applied to ensure the PV to lie within 100 mm around the nominal interaction point ($|z_{PV}| < 100$ mm). This cut removes approximately 6% of the signal candidates.

Table 4.3: Offline selection. The mass windows are centred around the values from the PDG [1]. The track clone distance is the Kullback-Liebler distance to the closest track [10] which helps to remove clone tracks and the DLS is the decay length significance.

Λ	
π/p track clone distance	> 5000
Mass window	± 6 MeV/c^2
DLS (for Λ_b^0 only)	> 3

J/ψ	
Vertex χ^2/ndf	< 16
Mass window	± 60 MeV/c^2

π from Ξ_b^- or K from Ω_b^-	
Track clone distance	> 5000
Kaon PIDK	> 5

Ξ^- or Ω^-	
Vertex χ^2/ndf	< 16
Mass window	± 11 MeV/c^2

Other requirement	
$|z_{PV}|$	< 100 mm

b baryon	
DTF χ^2/ndf	< 4
Best PV IP χ^2	< 25
Next-best PV IP χ^2	> 50

In each event, only a single b-baryon candidate is selected by taking the one with the lowest *DecayTreeFitter* χ^2. The total loss, including signal and background, due to events with multiple candidates not passing this requirement is 0.32% for Λ_b^0, 0.85% for Ξ_b^- and 0.78% for Ω_b^-. All cuts applied in the offline selection are listed in Table 4.3.

4.3   Decay time acceptance

The expression *decay time acceptance* used hereafter refers to the trigger, reconstruction and selection efficiency as a function of the reconstructed decay time. In this analysis the total decay time acceptance is factorized into two independently studied parts: the part coming only from the lifetime-biasing requirements of the trigger lines which affect mostly low values of the decay time, called the *lower decay time acceptance*, and the part coming from all reconstruction and selection effects which has a large impact for high values of the decay time, called the *upper decay time acceptance*. The first is described in Sec. 4.3.1 and the second in Sec. 4.3.2.

In the lifetime fit, the exponential function describing the b-baryon decay time distribution will be multiplied by the two decay time acceptances in order to adequately model the distorted distribution from recorded and reconstructed data.

4.3.1   Lower decay time acceptance

Candidates selected for this analysis did trigger HLT1 line Hlt1DiMuonHighMass (lifetime unbiased) or Hlt1TrackMuon (lifetime biased) or both, and did necessarily trigger HLT2 line Hlt2DiMuonDetachedJpsi (lifetime biased). Hence two categories of samples, according to

which trigger line fired the events, are defined. The first has a lifetime bias only from HLT2 and the second suffers from two lifetimes biases, one from HLT1 and one from HLT2. The definition of the sample categories are:

1. all events that are Hlt1DiMuonHighMass-TOS and Hlt2DiMuonDetachedJpsi-TOS (singly-biased sample),

2. all events that are not Hlt1DiMuonHighMass-TOS but Hlt1TrackMuon-TOS and Hlt2DiMuonDetachedJpsi-TOS (doubly-biased sample).

Simulated events and a lifetime unbiased HLT2 line (Hlt2DiMuonJpsi) are used to determine the trigger efficiency as a function of the reconstructed decay time for each of the two categories. This unbiased HLT2 line is not used directly in this analysis because it is pre-scaled by 20% in data, meaning that only 20% of the events that satisfy the trigger line criteria are randomly selected to be accepted by the line.

The efficiencies are obtained as the ratio of two histograms of the reconstructed decay time. For category 1, the efficiency is defined as the fraction of events passing Hlt2DiMuonDetachedJpsi-TOS amongst all events passing Hlt1DiMuonHighMass-TOS and Hlt2DiMuonJpsi-TOS:

$$\frac{\text{Hlt1DiMuonHighMass \& Hlt2DiMuonJpsi \& Hlt2DiMuonDetachedJpsi}}{\text{Hlt1DiMuonHighMass \& Hlt2DiMuonJpsi}}. \tag{4.1}$$

For category 2, the efficiency is defined as the ratio between the number of events of category 2 and the number of events passing the unbiased HLT1 and HLT2 lines:

$$\frac{\text{!Hlt1DiMuonHighMass \& Hlt1TrackMuon \& Hlt2DiMuonDetachedJpsi}}{\text{Hlt1DiMuonHighMass \& Hlt2DiMuonJpsi}}. \tag{4.2}$$

The latter is not an efficiency properly speaking because it has an arbitrary normalisation. This is not problematic because only the decay time dependence is important for the present analysis, the normalisation being provided directly by the fit. The definitions of the two sample categories can in principle be applied on data samples. However due to the lack of data statistics, simulated signal events are used instead for the nominal results.

Since the online reconstruction algorithms were improved between 2011 and 2012, different histograms are produced for the 2011 and 2012 data taking conditions using the corresponding *MC2011* and *MC2012* samples. No significantly different histograms were obtained for the different final state track type combinations (LL, DD, LLL, LDD and DDD). Hence one single description of the lower decay time acceptance is used for each trigger category and each year of data taking.
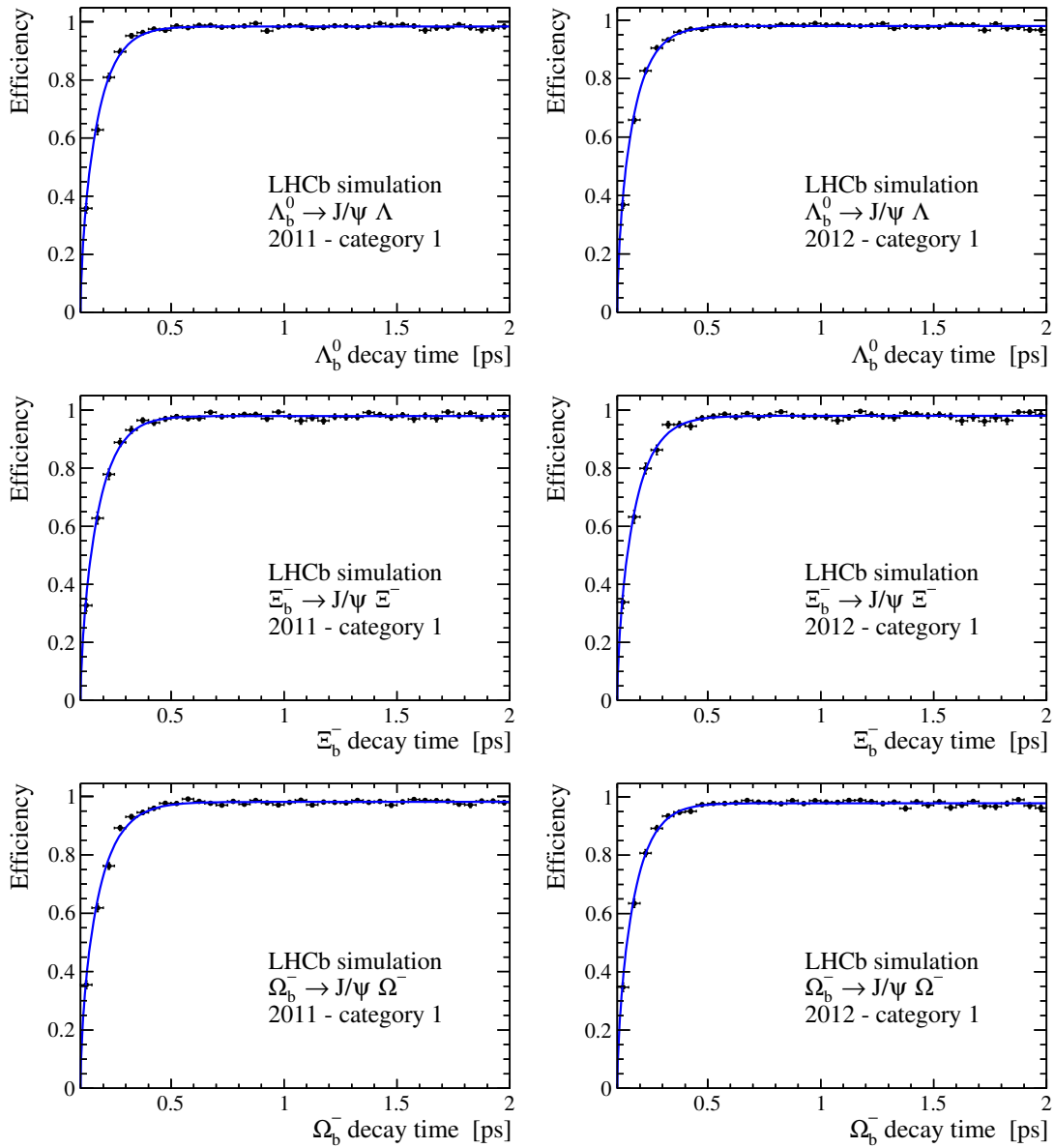
Figure 4.1: Λ_b^0 (top), Ξ_b^- (middle) and Ω_b^- (bottom) lower decay time acceptances for trigger category 1. The acceptance extracted from *MC2011* is on the left and from *MC2012* on the right. The result of the fit described in the text is overlaid.
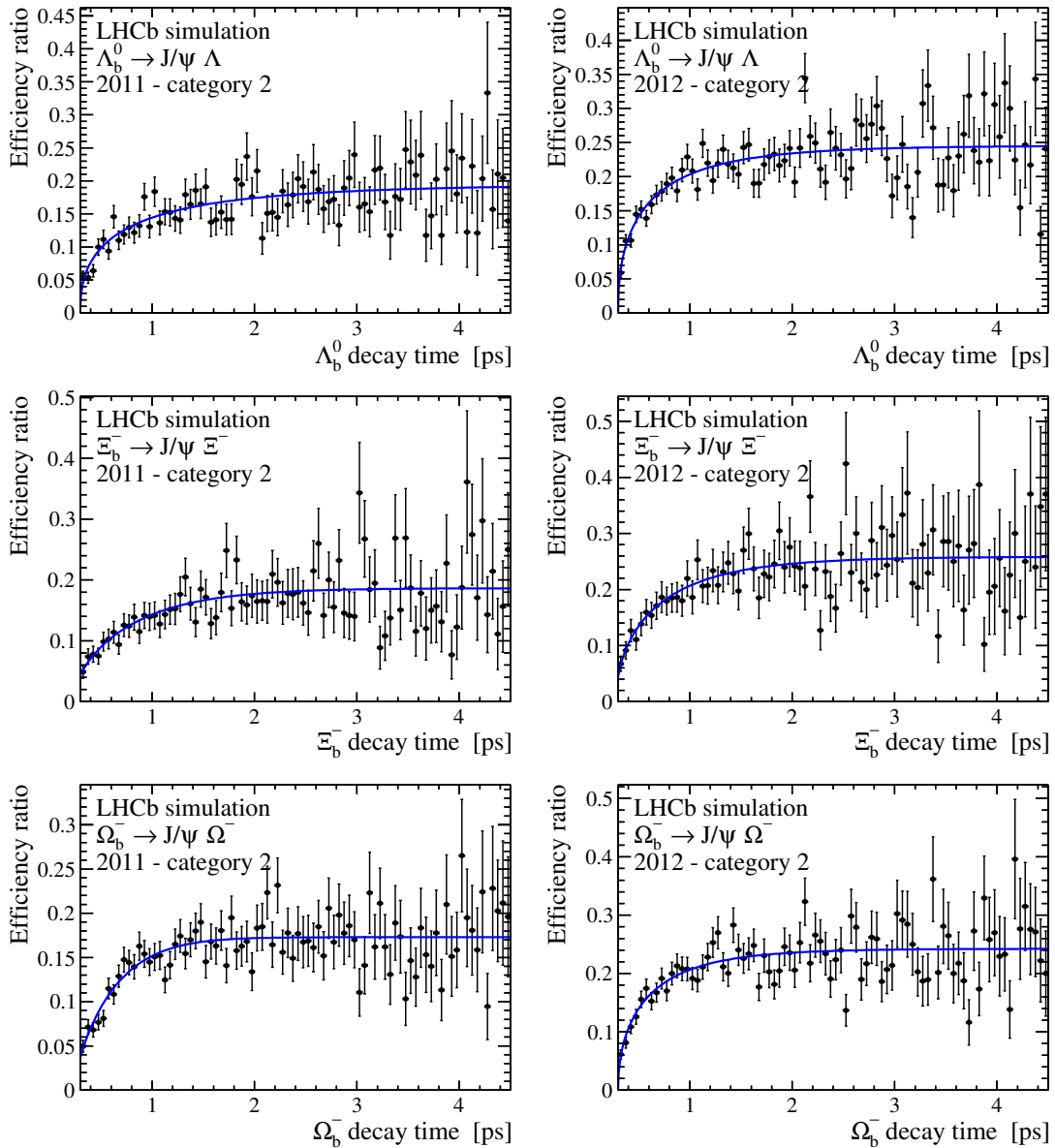
Figure 4.2: Λ_b^0 (top), Ξ_b^- (middle) and Ω_b^- (bottom) lower decay time acceptances for trigger category 2. The acceptance extracted from *MC2011* is on the left and from *MC2012* on the right. The result of the fit described in the text is overlaid.

The acceptance histograms are fitted with a function ϵ that has three free parameters called a, t_0 and n. This acceptance function is defined as

$$\epsilon(t) = \mathrm{Erf}(\, a \cdot (t - t_0)^n \,) \quad \text{where} \quad \mathrm{Erf}(t) = \int_0^t e^{-x^2} dx. \tag{4.3}$$

This function is found to well describe all considered acceptances and has the property of having a continuous derivative. The Λ_b^0, Ξ_b^- and Ω_b^- efficiency histograms with the overlaid fit results are shown in Figs. 4.1 and 4.2 for category 1 and 2 respectively. In the final lifetime fit, the function describing the decay time distribution of the signal is multiplied by the acceptance function corresponding to the category of the fitted events.

4.3.2 Upper decay time acceptance

The reconstruction and selection also have a non-flat efficiency as a function of the reconstructed b-baryon decay time due to the finite detector acceptance and the correlation between selection variables and the decay time. These effects are assumed to be well-described by the simulation since they are mainly of geometrical nature. The trigger also suffers from the detector acceptance since an event needs to be located within the acceptance to trigger. To take this into account but avoid effects from the lifetime biasing trigger requirements, that are described in the previous section, the events used to determine the upper decay time acceptance are required to fire the lifetime unbiased lines Hlt1DiMuonHighMass and Hlt2DiMuonJpsi.

To probe the inefficiencies, simulated events are reconstructed, selected step by step and their decay time distribution fitted with an exponential function at each stage. The hypothesis that the decay time distribution is still well-described by an exponential function after full reconstruction and selection is confirmed by the fit outcome. The difference between the fitted lifetime and the lifetime used in the generation of the simulated samples, here called bias, is reported for each step and shown in Fig. 4.3. The most significant bias appears when final state tracks are required to be reconstructible, i.e. to have trajectories within the geometrical detector acceptance (steps $1-10$ in the figure).

The lifetime bias as a function of the reconstruction, stripping or selection steps for different track type combinations are shown in Fig. 4.4 (Λ_b^0), Fig. 4.5 (Ξ_b^-) and Fig. 4.6 (Ω_b^-). It appears that the lifetime biases differ significantly for the different track type combinations. The biases are especially strong if the final state hadron tracks are of the long type.
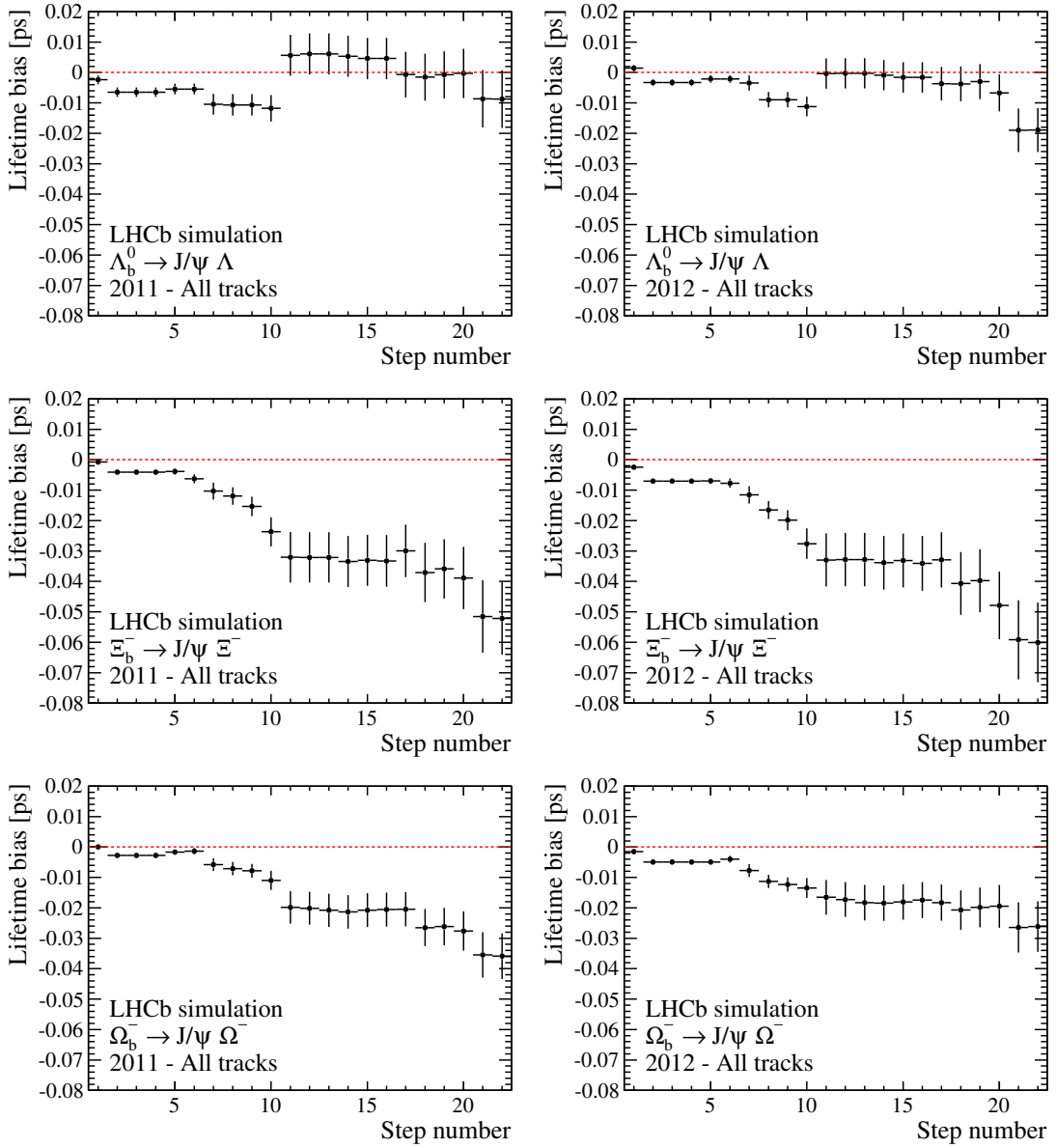
Figure 4.3: Λ_b^0 (top), Ξ_b^- (middle) and Ω_b^- (bottom) lifetime bias for *MC2011* (left) and *MC2012* (right) signal candidates reconstructed with all track combinations. Steps 1 to 11 show the effects of the reconstruction and the stripping. Steps 12 to 20 are obtained by successively applying the offline selection criteria. Steps 21 to 23 show the effect of the unbiased trigger lines. The detailed description of each step is given in Appendix A. Similar plots for each track type combination are shown in Figs 4.4, 4.5 and 4.6.
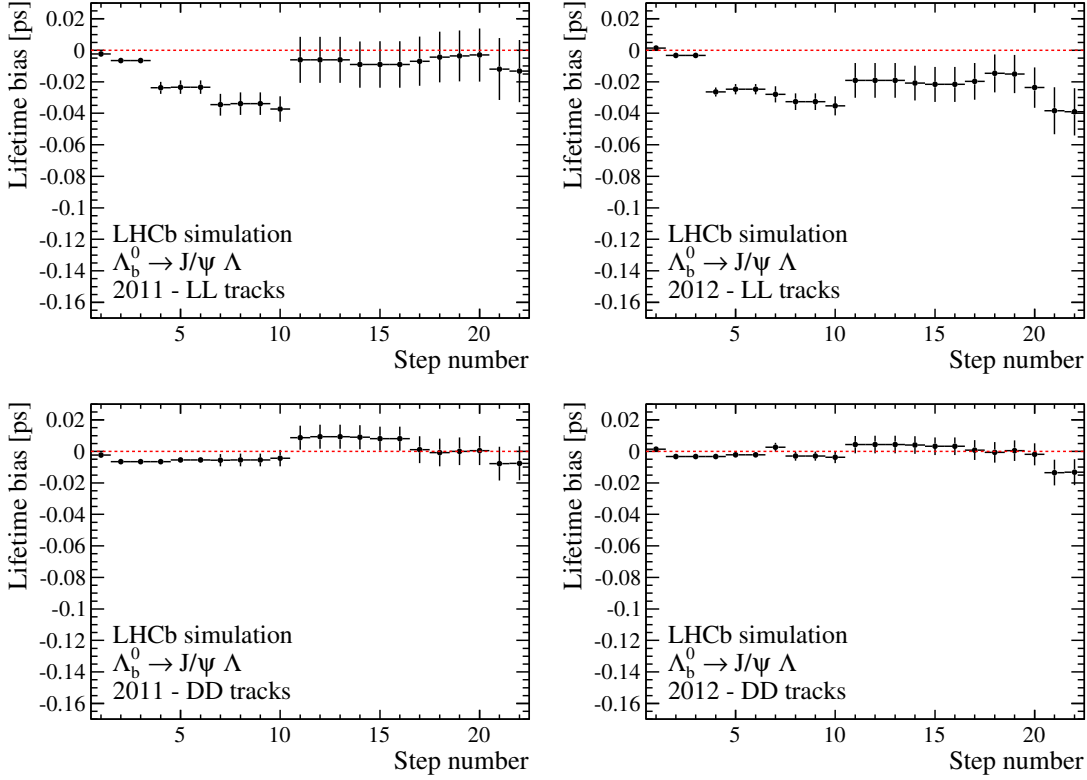
Figure 4.4: Λ_b^0 lifetime bias for *MC2011* (left) and *MC2012* (right) candidates reconstructed with LL (top) and DD (bottom) track combinations. Steps 1 to 11 show the effects of the reconstruction and the stripping. Steps 12 to 20 are obtained by successively applying the offline selection criteria. Steps 21 to 23 show the effect of the unbiased trigger lines. The detailed description of each step is given in Appendix A.

The upper decay time acceptance is found to be well described by a linear function. Therefore a slope parameter β is defined and the efficiency is modeled with the function $(1 + \beta t)$ where t is the reconstructed decay time. The β parameter is obtained by fitting the decay time distribution of fully reconstructed and selected events from simulation. The events are fitted with the function $(1 + \beta t) \cdot \exp(-t/\tau_{\text{True}})$ where τ_{True} is the lifetime used in the simulation. Separate β parameters are obtained for 2011 and 2012 data. The fits on simulated data of the β parameter for each decay mode and each year of data taking are shown in Fig. 4.7. The linear description of the decay time acceptance seems to be a good model.

Figure 4.5: Ξ_b^- lifetime bias for *MC2011* (left) and *MC2012* (right) candidates reconstructed with LLL (top), LDD (middle) and DDD (bottom) track combinations. Steps 1 to 11 show the effects of the reconstruction and the stripping. Steps 12 to 20 are obtained by successively applying the offline selection criteria. Steps 21 to 23 show the effect of the unbiased trigger lines. The detailed description of each step is given in Appendix A.

Figure 4.6: Ω_b^- lifetime bias for *MC2011* (left) and *MC2012* (right) candidates reconstructed with LLL (top), LDD (middle) and DDD (bottom) track combinations. Steps 1 to 11 show the effects of the reconstruction and the stripping. Steps 12 to 20 are obtained by successively applying the offline selection criteria. Steps 21 to 23 show the effect of the unbiased trigger lines. The detailed description of each step is given in Appendix A.

Figure 4.7: Distribution of the reconstructed decay time t in *MC2011* (left) and *MC2012* (right) after the re-weighting for the track type combination abundances. The superimposed blue solid curves are the results of fits with the function including a description of the upper decay time acceptance $(1 + \beta t) \cdot \exp(-t/\tau_{\text{true}})$, where τ_{true} is the generated lifetime and β the only free parameter in the fit. The gray dashed curve is the function without the acceptance, i.e. $\exp(-t/\tau_{\text{true}})$. Below the decay time distributions are shown the pull distributions of the fits including the acceptance description.

Table 4.4: Relative abundances (in %) of the different combinations of track types for signal events. The quoted uncertainties are purely statistical.

	LL or LLL	LDD	DD or DDD
Λ_b^0 MC	21.3 ± 0.2	–	78.7 ± 0.2
Λ_b^0 data	27.2 ± 0.7	–	72.9 ± 0.7
Ξ_b^- MC	6.5 ± 0.2	51.0 ± 0.4	42.5 ± 0.4
Ξ_b^- data	10.1 ± 2.5	56.6 ± 4.6	33.0 ± 4.3
Ω_b^- MC	7.2 ± 0.1	54.5 ± 0.3	38.3 ± 0.3
Ω_b^- data	16 ± 7	67 ± 11	18 ± 8

Because the upper decay time acceptance seems to behave differently for the different track type combinations, the abundances of these combinations are studied in simulation and in data. The fractions of each type in both simulation and data are given in Table 4.4. The results in *MC2011* and *MC2012* are identical within the statistical uncertainty, therefore only one number is given.

It appears that the abundance of certain combinations is low which makes the computation of individual β parameters difficult (ten times more simulation statistics would be needed to achieve the same level of precision as for a unique β parameter). Therefore the differences in abundances between simulation and real data are taken into account by re-weighting the simulated candidates to reproduce the track type combination abundance observed in data. Re-weighting for this abundance affects the β parameter by less than 20% of its assigned uncertainty which has a relatively weak effect on the measured lifetimes. The values of the β parameters obtained with re-weighted events from the simulated samples are given in Table 4.5. The β values differ significantly for Λ_b^0, Ξ_b^- and Ω_b^- but are consistent within statistical uncertainties between *MC2011* and *MC2012*.

The same function used to fit the β parameters is used in the lifetime fit of the data to describe the upper decay time acceptance. However the β parameter remains fixed to the values obtained from simulated events and the τ_{True} is replaced by the fitted signal lifetime parameter.

Table 4.5: β values (in ps^{-1}) for simulated Λ_b^0, Ξ_b^- and Ω_b^- decays. The quoted uncertainties are of statistical nature due to the finite size of the MC simulated samples. The fits giving these results are shown in Fig. 4.7

	2011	2012
Λ_b^0	$(-1.0 \pm 4.6) \times 10^{-3}$	$(-6.1 \pm 3.5) \times 10^{-3}$
Ξ_b^-	$(-13.1 \pm 4.8) \times 10^{-3}$	$(-20.2 \pm 5.0) \times 10^{-3}$
Ω_b^-	$(-23.3 \pm 3.5) \times 10^{-3}$	$(-19.3 \pm 3.9) \times 10^{-3}$

4.4 Decay time resolution

The reconstruction of the decay time, like for the mass, has a non-zero resolution. In the fit this effect is taken into account by convolving the exponential function modeling the signal and background decay time distributions with a Gaussian function. The width of this Gaussian function is fixed in the final fit and taken from simulated events by performing a fit with a Gaussian function of the distribution of the difference between the reconstructed decay time and the simulated one ($t_{\mathrm{Reco}} - t_{\mathrm{True}}$). Figure 4.8 shows the distribution of this difference for all three channels and both years of data taking as well as the fit. It appears that a fit with the sum of two Gaussian functions better describes the resolution. However, as shown in Sec. 4.6, using one or two Gaussian functions does not affect the lifetime result at all. Therefore it is decided to use only a single Gaussian in order to keep the procedure as simple as possible. A list of the obtained values for the different channels and periods of data taking is given in Table 4.6. The systematic uncertainties on these values and their propagation to the final results are discussed in Sec. 4.6.

Table 4.6: Gaussian decay time resolution (in fs) obtained from simulation for the three channels and both data taking conditions. The quoted uncertainties are statistical, due to the finite size of the generated samples.

	2011	2012
Λ_b^0	45.8 ± 0.3	47.5 ± 0.2
Ξ_b^-	47.2 ± 0.3	49.1 ± 0.4
Ω_b^-	46.2 ± 0.2	48.6 ± 0.3
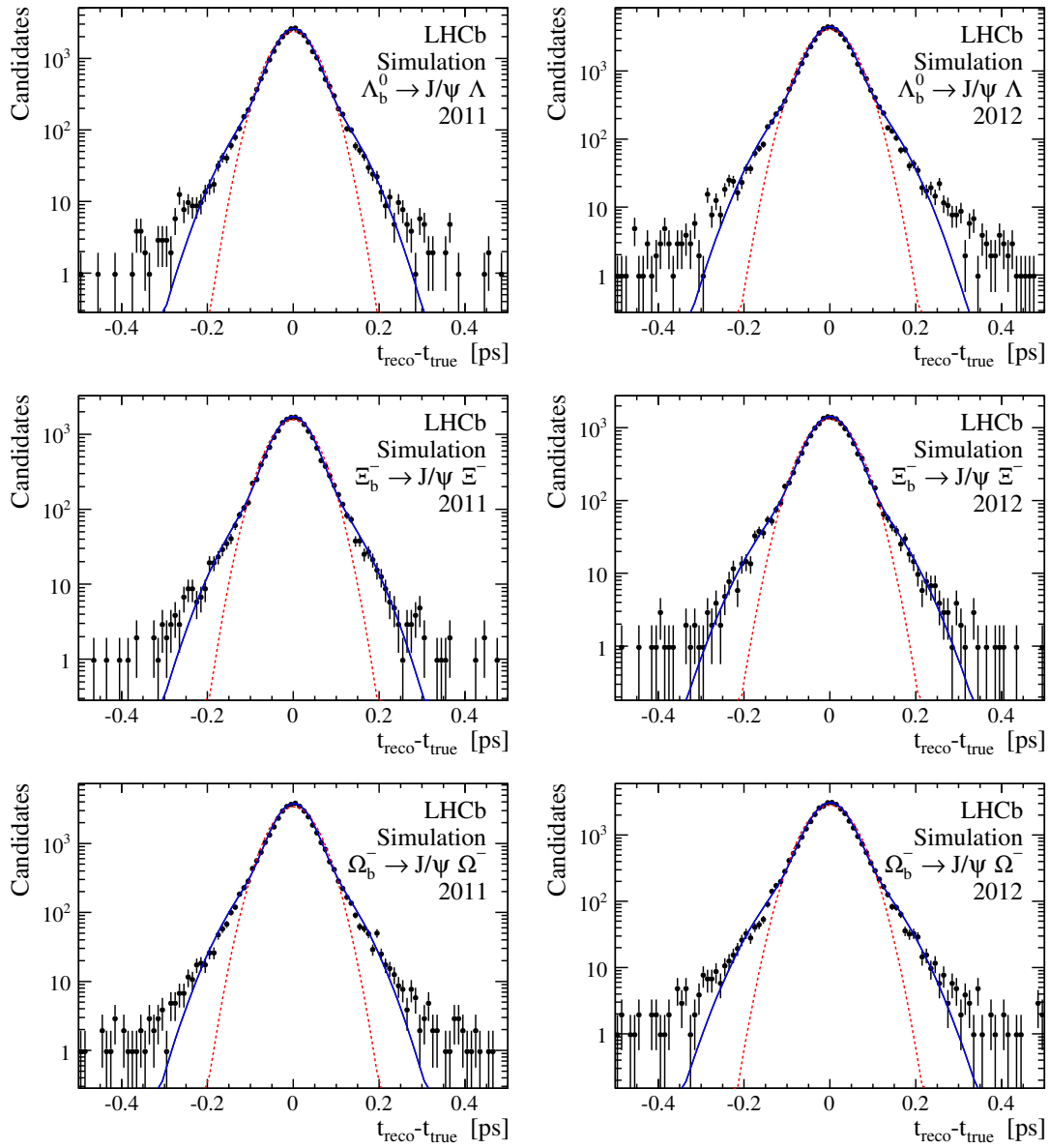
Figure 4.8: Distribution for Λ_b^0 (top), Ξ_b^- (middle) and Ω_b^- (bottom) of the difference between the reconstructed and generated decay time in *MC2011* (left) and *MC2012* (right). The results of a fit with one Gaussian function (red dashed line) and a fit with the sum of two Gaussian functions (blue solid line) are overlaid.

4.5 Lifetime fit

During the setup of the fit, the evaluation of the systematic uncertainties and all sanity cross-checks, the values of the fitted Ξ_b^- and Ω_b^- lifetimes were kept *blinded*. This means that the lifetime result given by the fit remains hidden until the last step of the analysis in order to avoid a bias from the person carrying out the measurements.

The b-baryon mass and decay time distributions are simultaneously fitted with a two-dimensional extended unbinned maximum likelihood fit. For the calculation of the b-baryon mass, the whole decay tree chain is refitted with the masses of the J/ψ and the primary hyperon (Λ for Λ_b^0, Ξ^- for Ξ_b^- and Ω^- for Ω_b^-) constrained to their respective PDG values [1]. The decay time is also computed with a full refit of the decay tree chain and, in addition, a full refit of the associated PV from which all final state tracks of the candidate are explicitly removed. In the decay time calculation the b baryon is constrained to originate from its associated PV but no mass constraint is applied on any daughter.

The use of two different decay chain fitters for the invariant mass and decay time calculations seems to be the optimal choice. Indeed the mass constraints applied in the decay chain fit for the invariant mass lower the resolution by a factor two, strongly increasing the discrimination between signal and background. However, if these mass constraints were applied in the decay time computation, they would induce a strong correlation between the decay time and the mass. Therefore the mass constraints are only used for the invariant mass calculation and are not used for the decay time. By using this approach, no significant correlation between decay time and mass is observed.

In the fit, the events are split into four categories corresponding to all possible combinations of data taking periods (2011 and 2012) and trigger categories (singly-biased and doubly-biased). Therefore eight free parameters for the yields of signal and background in each category are determined.

In the mass distribution the signal is described with a single (double) Gaussian function for Ξ_b^-, Ω_b^- (Λ_b^0) with different mean values for data recorded in 2011 and in 2012. The widths and the yield fraction between the two Gaussian functions in the Λ_b^0 case are common for all categories and left free. The mass background is described with a single exponential function. The fit ranges for the mass distribution are 5500–5750 MeV/c^2 for Λ_b^0, 5600–6000 MeV/c^2 for Ξ_b^- and 5800–6300 MeV/c^2 for Ω_b^-.

The signal in the decay time distribution is modeled with an exponential function convolved with a Gaussian function that has a fixed width for each data taking period as explained in Sec. 4.4. This convolution is multiplied by the lower and upper decay time acceptances which are determined from simulation as described in Secs. 4.3.1 and 4.3.2 respectively. Two (three) exponential functions convolved as well with the Gaussian resolution function are used to describe the decay time distribution of the background component for Ξ_b^-, Ω_b^- (Λ_b^0). These functions all have one free parameter in the exponent and their relative yields are left free in

Table 4.7: Fitted parameters for the Λ_b^0, Ξ_b^- and Ω_b^- signals. The quoted uncertainties are purely statistical. The central values of the measured masses are meaningless since no momentum scale calibration is applied.

	$\Lambda_b^0 \to J/\psi\,\Lambda$	$\Xi_b^- \to J/\psi\,\Xi^-$	$\Omega_b^- \to J/\psi\,\Omega^-$
Yield	18660 ± 154	313 ± 20	58 ± 8
2011 mass [MeV/c^2]	5621.08 ± 0.13	5798.5 ± 0.9	6051.2 ± 2.4
2012 mass [MeV/c^2]	5621.11 ± 0.09	5799.5 ± 0.7	6048.9 ± 1.4
Mass resolution (1) [MeV/c^2]	6.91 ± 0.23	8.5 ± 0.5	7.5 ± 1.0
Mass resolution (2) [MeV/c^2]	14.8 ± 0.7	–	–
Yield fraction (1)/(2)	0.70 ± 0.05	–	–
Lifetime [ps]	1.451 ± 0.012	$1.55^{+0.10}_{-0.09}$	$1.54^{+0.26}_{-0.21}$

the fit. In order to remove a large fraction of the prompt J/ψ background, the decay time is fitted in the range between 0.3 and 14 ps for all channels.

Finally, a total of eight parameters for the yields, four (six) parameters to model the mass distribution and four (six) parameters to model the decay time distribution are left free in the Ξ_b^-, Ω_b^- (Λ_b^0) fit. The results of the fitted signal parameters are given in Table 4.7. The yields equal approximately three times the yields observed in the mass measurements using 2011 data alone. Asymmetric statistical uncertainties are computed with MINOS [83, 84]. Figures 4.9, 4.10 and 4.11 show the projections of the fit results over the mass and decay time distributions.

To ensure that the signal and background components in the decay time distributions are well described by the fit, the decay time distribution for two mass regions is looked at separately. The signal and background regions are defined in the mass distribution by cuts at three σ around the measured mass. The results are also shown in Figs. 4.9, 4.10 and 4.11.

It appears that the Ξ_b^- and Ω_b^- distributions are well described. In the case of the Λ_b^0, a difference between the background description in the lower and upper mass sidebands is seen in the region from 1 to 4 ps. This might be due to the $B^0 \to J/\psi\,K_s^0$ background that is not taken into account in the fit. Since the Λ_b^0 lifetime measurement is only a cross-check, this shortcoming is not investigated further.
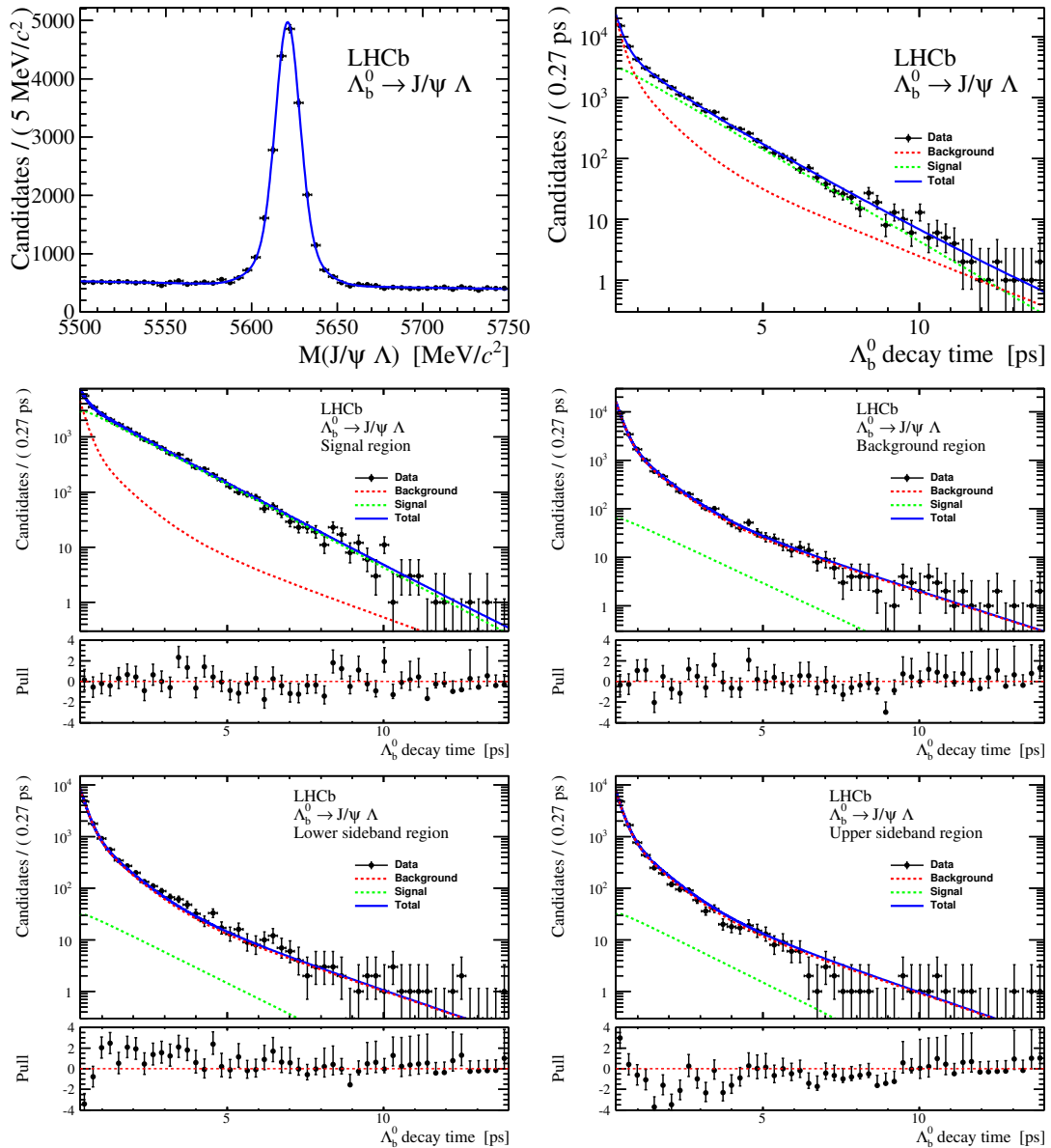
Figure 4.9: Top: invariant mass (left) and decay time (right) distributions of $\Lambda_b^0 \to J/\psi \Lambda$ candidates. The result of the two-dimensional unbinned extended maximum likelihood fit is overlaid. Middle and bottom: distributions and fit projections of the Λ_b^0 decay time in the signal mass region (middle left), the background mass region (middle right), the lower mass sideband (bottom left) and the upper mass sideband (bottom right). The pulls of the fit are shown below the distributions.
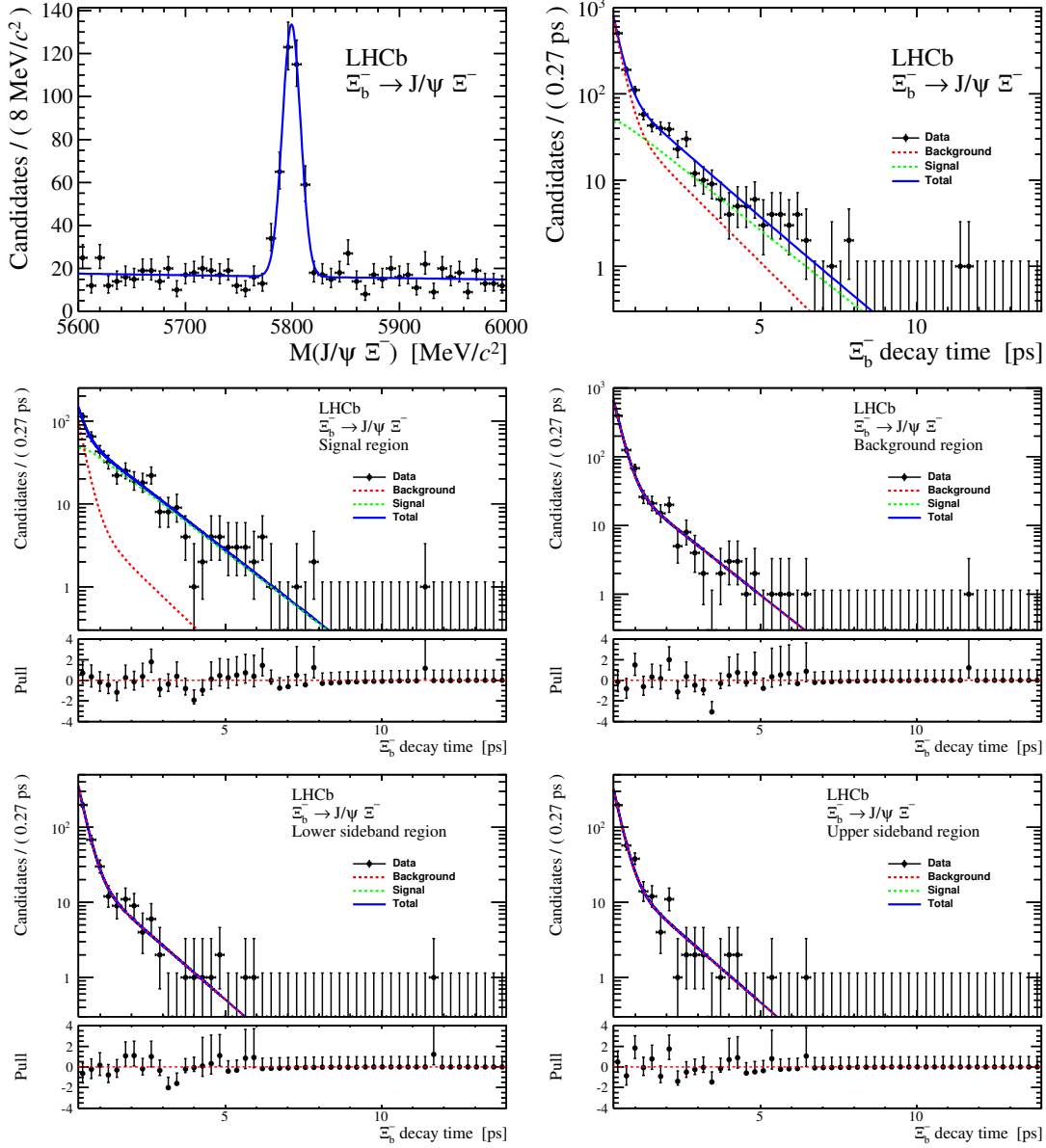
Figure 4.10: Top: invariant mass (left) and decay time (right) distributions of $\Xi_b^- \to J/\psi\,\Xi^-$ candidates. The result of the two-dimensional unbinned extended maximum likelihood fit is overlaid. Middle and bottom: distributions and fit projections of the Ξ_b^- decay time in the signal mass region (middle left), the background mass region (middle right), the lower mass sideband (bottom left) and the upper mass sideband (bottom right). The pulls of the fit are shown below the distributions.
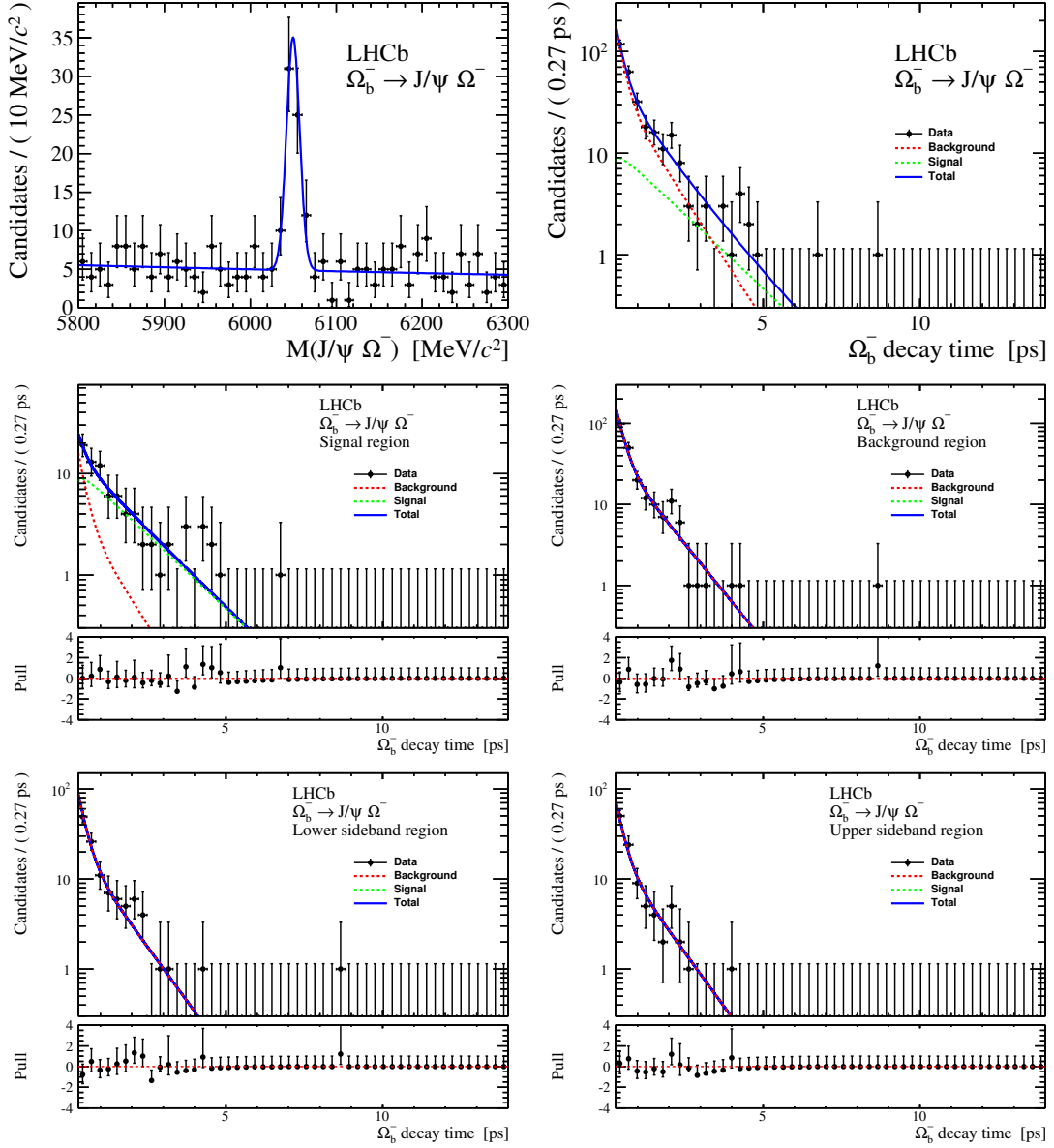
Figure 4.11: Top: invariant mass (left) and decay time (right) distributions of $\Omega_b^- \to J/\psi\,\Omega^-$ candidates. The result of the two-dimensional unbinned extended maximum likelihood fit is overlaid. Middle and bottom: distributions and fit projections of the Ω_b^- decay time in the signal mass region (middle left), the background mass region (middle right), the lower mass sideband (bottom left) and the upper mass sideband (bottom right). The pulls of the fit are shown below the distributions.

4.6 Systematic uncertainties

Unless specified otherwise, the systematic uncertainties are assessed by performing an alternative lifetime fit where one parameter or part of the model is varied and taking the difference between its lifetime result and the nominal fit result. The total systematic uncertainty is the quadratic sum of all individual contributions. A summary of the systematic uncertainties is given in Table 4.8.

4.6.1 Upper decay time acceptance

The upper decay time acceptance is described with a linear function of slope β. A first uncertainty on the β parameter is of statistical nature and arises from the finite size of the simulated samples. A second contribution takes into account the accuracy with which the simulation describes this acceptance. The cause of a non-zero β parameter is the reconstruction and selection efficiencies which depend mostly on the geometrical description of the system. It is assumed that this description is at most wrong by $\pm 50\%$ in the LHCb simulation. Hence the contribution to the β parameter uncertainty due to the difference between simulation and data is taken as half its value. The total uncertainty on the β parameter is the quadratic sum of these two contributions.

As described in Sec. 4.3.2, the β parameter is obtained from simulated events after a re-weighting which reproduces the track type combination abundance observed in data. A check was performed by computing the β parameter without the re-weighting and it appears that the difference between the two results are well contained within the uncertainty assigned to β.

The systematic uncertainty on the lifetime measurement due to the limited knowledge of the upper decay time acceptance is taken as the maximum difference between the result from a fit where the β parameters are varied within their uncertainty and the nominal fit result. The two β parameters for 2011 and 2012 are assumed to be fully correlated and are varied together.

Table 4.8: Summary of systematic uncertainties on the lifetime measurements in fs.

Source	$\Lambda_b^0 \to J/\psi\,\Lambda$	$\Xi_b^- \to J/\psi\,\Xi^-$	$\Omega_b^- \to J/\psi\,\Omega^-$
Upper decay time acceptance	10.2	29.0	45.0
Lower decay time acceptance	6.2	9.9	6.5
Signal modeling	3.1	5.9	11.4
Combinatorial background modeling	1.0	3.0	3.0
Physics backgrounds	1.1	0.1	11.1
Detector length scale	0.3	0.3	0.3
Quadratic sum	12.4	31.4	48.3

Since this is the leading contribution to the total systematic uncertainty, a study testing the statistical robustness of this result is performed and described in Sec. 4.7.

4.6.2 Lower decay time acceptance

Simulated events are also used to describe the lower decay time acceptance. Since this copes with the efficiency of the trigger, other channels triggering on the same lines and having similar decay topologies can be used as an alternative. The trigger lines considered here heavily rely on the muons and the J/ψ. Another decay abundantly reconstructed at LHCb with a J/ψ decaying to $\mu^+\mu^-$ and which is similar to the ones considered in this analysis is $B^0 \to J/\psi\,K_S^0$. As illustrated in Fig. 4.12, the same efficiency histograms as for the different channels and categories are therefore made using real data from this channel. For each bin of the histograms the mass distribution is fitted to extract the signal yields. An alternative fit including the acceptance function obtained from these histograms from data instead of the nominal ones from simulation is performed and the difference between its result and the nominal lifetime result is assigned as the systematic uncertainty arising from the imperfect knowledge of the lower decay time acceptance.

A second uncertainty related to the lower decay time acceptance arises from the limited size of the simulated samples. This propagates to the uncertainty on the fitted parameters of the acceptance function. The associated systematic uncertainty is therefore assessed by varying in turn these parameters within their statistical uncertainty and by taking the largest observed shift in the fitted lifetime. The total systematic uncertainty due to the limited knowledge of the lower decay time acceptance is the quadratic sum of both contributions described here.
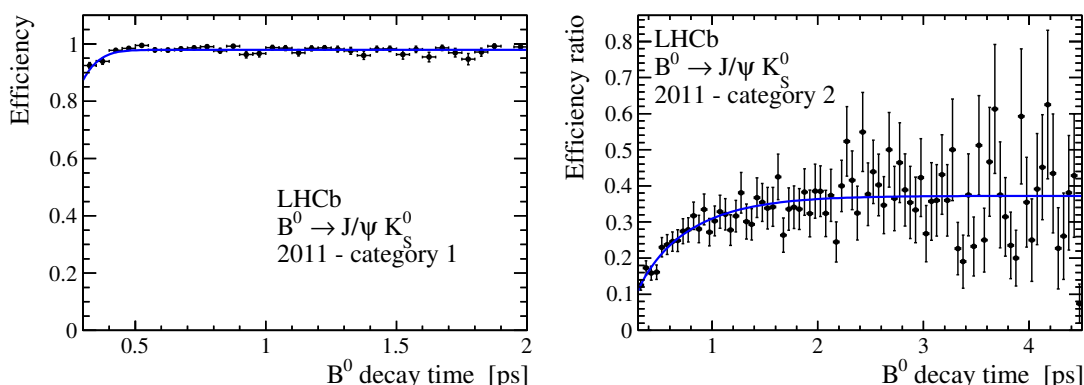
Figure 4.12: $B^0 \to J/\psi\,K_S^0$ lower decay time acceptances from 2011 data. The acceptance for trigger category 1 (2) is on the left (right). The result of the fit described in the text is overlaid.

4.6.3 Signal modeling

Decay time description:

The decay time resolution is fixed in the fit to values extracted from simulation. The values are varied by $\pm10\%$ which makes the lifetime fit result vary by less than 0.1 fs. In another check, the single Gaussian function is replaced with a double Gaussian where both widths and the yield ratio are fixed to values extracted from simulation. In this case again the variation of the fitted lifetime is smaller than 0.1 fs. These two contributions are negligible compared to the ones due to the mass description of the signal.

Mass description:

For the Ξ_b^- and Ω_b^- fits the single Gaussian describing the signal in the mass distribution is replaced with the sum of two Gaussian functions. The ratio between the widths and the yields of the two Gaussian functions are fixed to the values obtained from simulated events. The Λ_b^0 signal is alternatively fitted with the sum of two *Crystal Ball* functions [80] instead of two Gaussian functions. All parameters of the two *Crystal Ball* functions are left free but are common to the trigger and data taking period categories with the exception of the central values which are different for 2011 and 2012 data.

It appears that with the alternative signal mass model the fitted Ω_b^- lifetime changes more than the ones of the Ξ_b^- and Λ_b^0 baryons. To verify that the origin of this change is not due to a statistical fluctuation a toy study is performed. In this study around 2'000 two-dimensional (mass and decay time) toy distributions are generated using the nominal fit model and parameters. Fitting with both the nominal fit and the alternative fit, it appears that the shift observed in data is expected. A more complete description of this pseudo-experiment based study is given in Sec. 4.7.

4.6.4 Combinatorial background modeling

Decay time description:

The two (three) exponential functions describing the decay time distribution of the combinatorial background are replaced with three (two) exponential functions. They are still convolved with the Gaussian resolution function and all their parameters left free. The change in the fitted lifetime is of 0.7 fs for Λ_b^0 and 3.0 fs for both Ξ_b^- and Ω_b^-. It is again assumed that the relatively large changes for Ξ_b^- and Ω_b^- compared to the change of the Λ_b^0 are due to the limited statistics of the former two channels.

Mass description:

Instead of an exponential function, a linear function is used to describe the combinatorial mass background. This alternative fit shifts the lifetime result by 0.7 fs for Λ_b^0, 0.1 fs for Ξ_b^- and 0.4 fs for Ω_b^-. In another alternative fit, the mass background is separately modeled for events from the 2011 and from the 2012 data samples with one exponential function for each year. The change in lifetime is 0.1 fs for Λ_b^0, 0.3 fs for Ξ_b^- and 0.2 fs for Ω_b^- this time.

Once again a toy study with more than 2'000 generated mass and decay time distributions is performed. It shows that in all cases the fitted lifetime shifts observed in data are as expected.

The total systematic uncertainty assigned to the combinatorial background modeling is taken as the quadratic sum of the largest contribution from the decay time modeling and the largest contribution from the mass modeling.

4.6.5 Physics backgrounds

A certain number of $\Omega_b^- \to J/\psi\,\Omega^-$ decays might be reconstructed as $\Xi_b^- \to J/\psi\,\Xi^-$ (or vice-versa) if the bachelor kaon (pion) is misidentified as a pion (kaon). To assess this background the reconstruction of each channel is performed on simulation samples of the other. The reconstructed physics background candidates are required to match the simulated decay in order to avoid combinatorial background. Around 0.24 Ω_b^- decays are expected to be reconstructed as Ξ_b^- and around 3.0 Ξ_b^- decays as Ω_b^- in the full 3.0 fb^{-1} data set and over the full mass range considered in the fit. The mass and decay time distributions from simulation scaled to the yields expected in 3.0 fb^{-1} of data are shown in Fig. 4.13.

The cross-feed background between Ξ_b^- and Ω_b^- are not strongly peaking in the mass distributions and are therefore mostly assigned to combinatorial background in the fit. To estimate the potential lifetime bias, the nominal fit is performed on two simulated samples: one containing and one not containing this physics background component. The difference between the two fits is assigned as a systematic uncertainty due to the fact that these physics backgrounds are not taken into account in the fit.

It can also happen that $B^0 \to J/\psi\,K_S^0$ decays are reconstructed as $\Lambda_b^0 \to J/\psi\,\Lambda$ due the misidentification of a charged kaon as a proton. Since the Λ_b^0 lifetime measurement is only a cross-check of the methodology, the effect of this background is taken from the study of the Λ_b^0 lifetime with only 2011 data [41]. In this analysis it has been shown that this is the major physics background in $\Lambda_b^0 \to J/\psi\,\Lambda$ and the bias is of 1.1 fs which we assign as the related systematic uncertainty.

4.6.6 Detector length and momentum scales

The overall length of the VELO detector is known up to a relative precision of 2.2×10^{-4} [41]. The lifetime being proportional to the distance measurement, this number is directly taken as the relative systematic uncertainty due to the imperfect knowledge of the detector length scale.
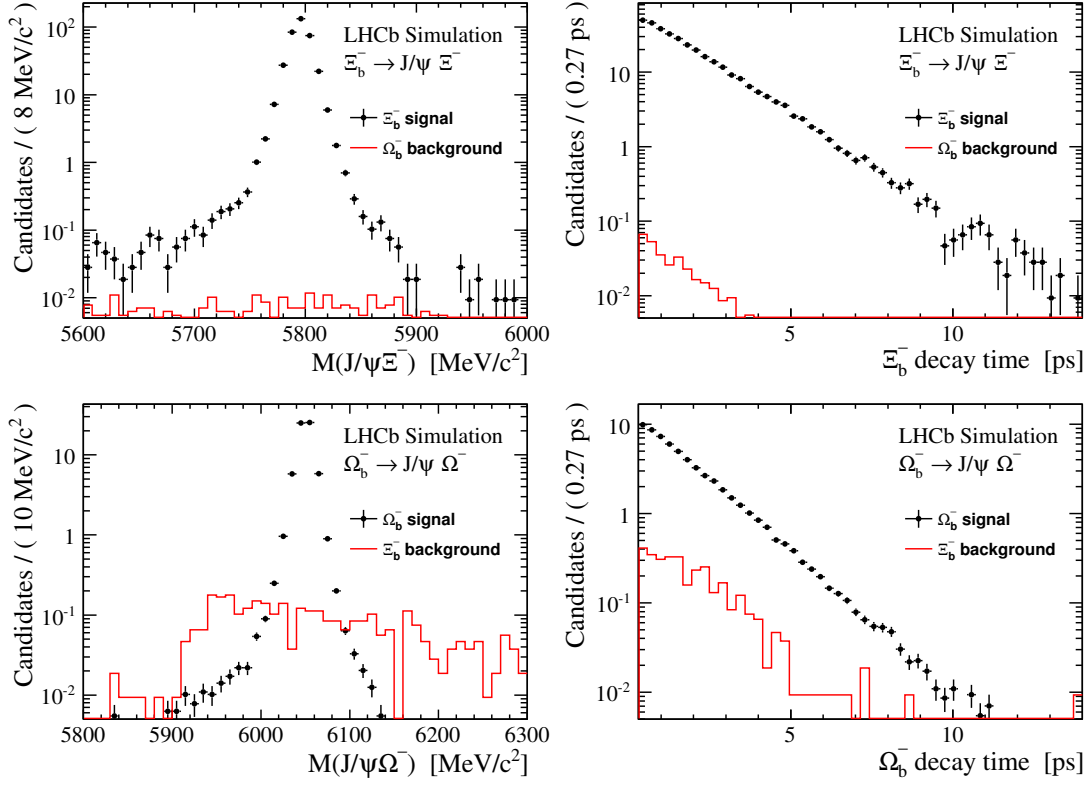
Figure 4.13: Distribution of the invariant mass (left) and the decay time (right) of reconstructed Ξ_b^- (top) and Ω_b^- (bottom) decays in both Ξ_b^- and Ω_b^- simulated samples. All samples are scaled to the corresponding yield expected in the 3 fb^{-1} of data. Considering the full mass range, around 0.24 Ω_b^- baryons are reconstructed as Ξ_b^- and 3.0 Ξ_b^- baryons as Ω_b^- to be compared to the 313 Ξ_b^- and 58 Ω_b^- signal candidates in data.

In the calculation of the decay time, the momentum scale only contributes at second order. Indeed the decay time t is computed as

$$t = \frac{d}{\beta \gamma c} = \frac{dm}{p} \tag{4.4}$$

where d is the measured distance of flight, m the measured mass and p the measured momentum. The first order momentum dependence is contained both in m and p and therefore cancels. A study performed for the lifetime measurements of different b-hadrons [41] shows that without applying the momentum scale calibration, the measured lifetime is biased by less than 0.1 fs, which is negligible.

4.7   Checks with pseudo-experiments

Approximately 2'000 pseudo-experiments were generated in the form of two-dimensional mass-decay time distributions for both the Ξ_b^- and Ω_b^- channels. The function used in the fit and the parameters returned by the nominal fit on data are used as the probability density function for the generation.

In order to assess a bias from the fit model, the generated distributions are fitted with the nominal fit function. The distribution of the difference between the lifetime fit result and the value used in the generation, i.e. the measured lifetime in data, is shown on Fig. 4.14. It appears that in both cases the mean of this distribution is consistent with zero and that the width is consistent with the statistical uncertainty of the lifetime measurement. Therefore confidence is gained that the fit model is appropriate and does not bias the result.

To take the check one step further, the so-called pull distribution is studied. It is defined as

$$
\begin{cases}
\dfrac{\tau_{\text{gen}} - \tau_{\text{fit}}}{\sigma_\tau^+} & \text{if} \quad \tau_{\text{fit}} \le \tau_{\text{gen}} \\[2ex]
\dfrac{\tau_{\text{fit}} - \tau_{\text{gen}}}{\sigma_\tau^-} & \text{if} \quad \tau_{\text{fit}} > \tau_{\text{gen}}
\end{cases}
\tag{4.5}
$$

where τ_{gen} is the generated lifetime, τ_{fit} is the fitted lifetime and $\sigma_\tau^\pm$ are the positive and negative statistical uncertainties returned by the fit. Figure 4.15 shows this distribution for the Ξ_b^- and Ω_b^- pseudo-experiments and the result from a fit with a Gaussian function is overlaid. The distribution is well-described with the Gaussian function, hence the asymmetric statistical uncertainties returned by MINOS are appropriate.
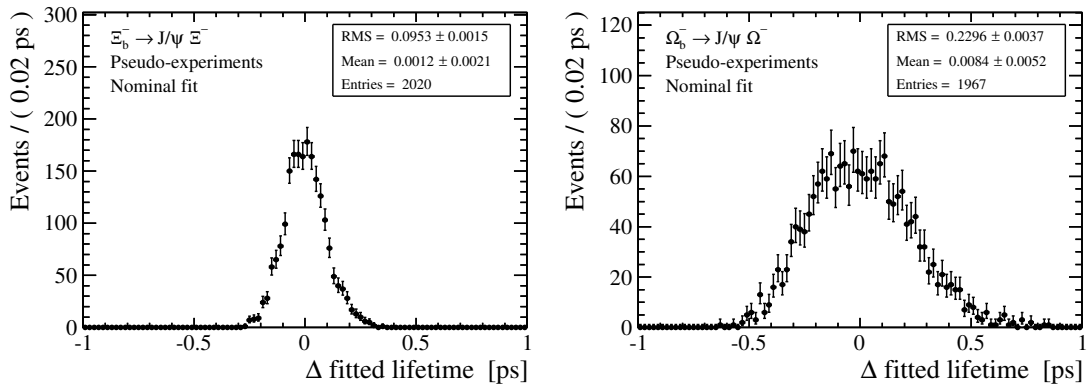
Figure 4.14: Difference between the lifetime fitted with the nominal fit and the value used in the generation of the pseudo-experiments for Ξ_b^- (left) and Ω_b^- (right). The means are consistent with zero and the widths are consistent with the statistical uncertainties of the final result.
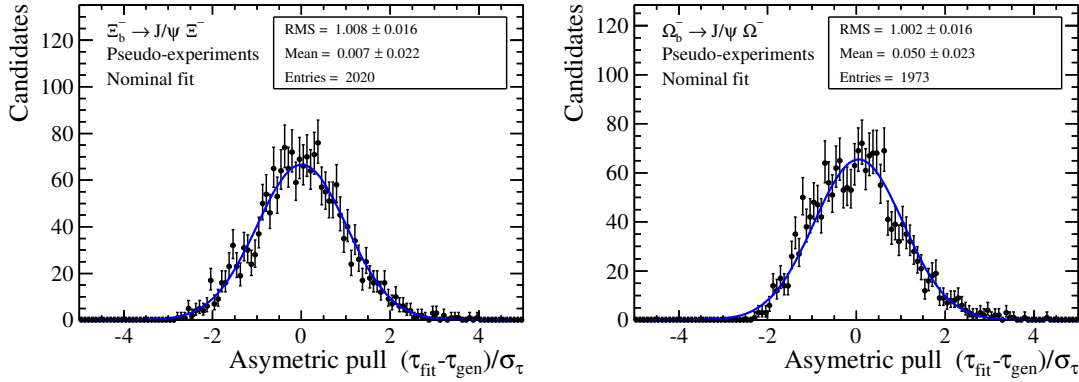
Figure 4.15: Asymmetric pull distribution of the fit on pseudo-experiments for Ξ_b^- (left) and Ω_b^- (right). The result of a fit with a Gaussian function is overlaid. The widths of the distributions are compatible with one.

Since the statistical power of the data sample is weak a pseudo-experiment study is performed to assess if the assigned systematic uncertainties are statistically robust. The same 2'000 generated distributions are fitted with all alternative fits. It appears that in all cases the average difference with respect to the nominal fit is consistent with the assigned systematic uncertainty.

The limited knowledge of the upper decay time acceptance is the origin of the largest contribution to the systematic uncertainty. Hence the differences between the fit with the varied β parameter and the nominal fit are shown in Figs 4.16 and 4.17. It appears that the average shifts observed in the pseudo-experiments are in agreement with the values assigned to the uncertainties related to the upper decay time.

4.8   The fully downstream alternative

As can be seen in Table 4.8, the uncertainty on the upper decay time acceptance is the largest contribution to the total systematic uncertainty. Figures 4.4, 4.5 and 4.6 show that the bias due to the upper decay time acceptance is the largest for track type combinations involving long tracks. The associated systematic uncertainty being proportional to this bias (50% of the β parameter) could be strongly reduced by using only downstream tracks and converting the long tracks into downstream ones whenever possible.

Due to missing TT hits and the lower efficiency of the downstream tracking, the efficiency for Ξ_b^- and Ω_b^- of reconstructing a final state long track as a downstream track is approximately 50%. Therefore around 87.5% of the LLL track type combinations (representing $\sim 10\%$ of the statistics) and around 50% of the LDD track type combinations (representing $\sim 55\%$ of the statistics) would be lost. In total the yield would decrease by around 8.75% + 27.5% = 36.25% and therefore the statistical uncertainty would increase by $\sim 25\%$.

Figure 4.16: Difference between the Ξ_b^- lifetime fitted with the nominal fit and the Ξ_b^- lifetime fitted with a fit where beta is subtracted (left) or added (right) its assigned uncertainty. The mean of the shift is consistent with the assigned systematic uncertainty of 29.8 fs.
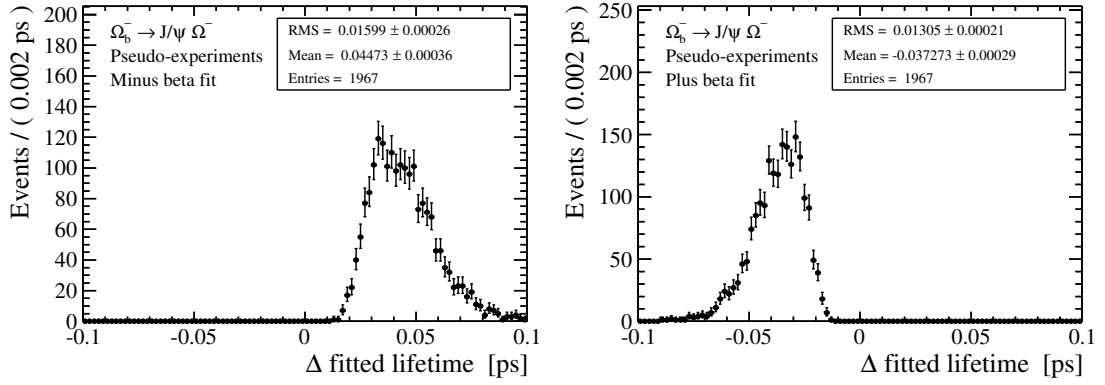
Figure 4.17: Difference between the Ω_b^- lifetime fitted with the nominal fit and the Ω_b^- lifetime fitted with a fit where beta is subtracted (left) or added (right) its assigned uncertainty. The mean of the shift is consistent with the assigned systematic uncertainty of 55.4 fs.

The precision of the lifetime measurements is strongly limited by statistics. The Ξ_b^- having a lower statistical uncertainty is the channel whose total uncertainty would benefit the most from an improvement of the systematic uncertainty. Assuming the extreme case in which the whole systematic uncertainty would come from the upper decay time acceptance and would decrease to zero by the use of only downstream tracks, the total uncertainty would change from ± 0.100 (stat) ± 0.030 (syst) $= \pm 104$ (tot) ps to ± 0.125 (stat) ± 0.000 (syst) $= \pm 0.125$ (tot) ps. This result is worse than the initial one and justifies the use of all track types.

4.9 The Λ_b^0 cross-check

Using the same techniques as for Ξ_b^- and Ω_b^-, the Λ_b^0 lifetime is measured to be

$$\tau(\Lambda_b^0) = 1.451 \pm 0.012 \text{ (stat)} \pm 0.012 \text{ (syst) ps.}$$

Table 4.9 compares this result with the current PDG world average that contains measurements from ALEPH [85], DELPHI [86], OPAL [87], CDF [88–90], D0 [91, 92] and ATLAS [5] as well as with recent CMS [93] and LHCb [41, 94, 95] measurements. The table also displays the results of sanity cross-checks where the data sample was split according to the year of data taking, the magnet polarity and the track type combinations.

The single most precise determination of the Λ_b^0 lifetime is provided by LHCb [95] where the lifetime ratio between Λ_b^0 and B^0 is measured and combined with the world average of the B^0 lifetime. The high precision of this measurement comes from the fact that the considered decay channels, $\Lambda_b^0 \rightarrow J/\psi\, pK^-$ and $B^0 \rightarrow J/\psi\, \pi^- K^+$, are abundantly reconstructed at LHCb and that the systematic uncertainties partially cancel in the ratio.

The approach of the absolute lifetime measurement using 2011 data presented in Ref. [41] leads to larger statistical uncertainties than what is measured here with the same data set. Indeed

Table 4.9: Comparison between Λ_b^0 lifetime measurements in ps.

Measurement	$\tau(\Lambda_b^0)$	(stat)	(syst)	(tot)
Particle Data Group average [1]	1.429			± 0.024
CMS $\Lambda_b^0 \rightarrow J/\psi\, \Lambda$ (5 fb^{-1}) [93]	1.503	± 0.052	± 0.031	± 0.061
LHCb $\Lambda_b^0 \rightarrow J/\psi\, \Lambda$ (1.0 fb^{-1}) [41]	1.415	± 0.027	± 0.006	± 0.028
LHCb $\Lambda_b^0 \rightarrow J/\psi\, pK^-$ (1.0 fb^{-1}) [94]	1.482	± 0.018	± 0.012	± 0.022
LHCb $\Lambda_b^0 \rightarrow J/\psi\, pK^-$ (3.0 fb^{-1}) [95]	1.476	± 0.009	± 0.009	± 0.013
This measurement (total 3.0 fb^{-1})	1.451	± 0.012	± 0.012	± 0.017
- Only 2011 data (1.0 fb^{-1})	1.415	± 0.019	$\pm 0.012^*$	± 0.022
- 2011 LL combinations	1.427	± 0.037	$\pm 0.012^*$	± 0.039
- 2011 DD combinations	1.411	± 0.023	$\pm 0.012^*$	± 0.026
- Only 2012 data (2.0 fb^{-1})	1.470	± 0.014	$\pm 0.012^*$	± 0.018
- 2012 LL combinations	1.437	± 0.027	$\pm 0.012^*$	± 0.030
- 2012 DD combinations	1.481	± 0.017	$\pm 0.012^*$	± 0.021
- Only magnet up polarity	1.447	± 0.017	$\pm 0.012^*$	± 0.021
- Only magnet down polarity	1.455	± 0.016	$\pm 0.012^*$	± 0.020
- Only LL combinations	1.435	± 0.022	$\pm 0.012^*$	± 0.025
- Only DD combinations	1.457	± 0.014	$\pm 0.012^*$	± 0.018

* The systematic uncertainties on the sub-sample results are naively taken from the total result.

the strategy of the analysis presented in Ref. [41] is to minimize the systematic uncertainties since most of the considered channels are limited by this uncertainty.

The two measured lifetimes based on the data samples from 2011 and 2012 present a difference corresponding to 1.9 standard deviations. This might point towards a strong downward fluctuation of the 2011 data and/or upward fluctuation of the 2012 data. Comparing to the currently most precise measurement based on an independent data set [95], it seems that the measurement from the 2011 data is the one that deviates. The discrepancy of 2.0 standard deviations appearing between the absolute lifetime measurement of Ref. [41] and the measurement from the ratio [95] gives an additional hint that the decay $\Lambda_b^0 \to J/\psi\,\Lambda$ reconstructed with 2011 data presents indeed a downward fluctuation of the lifetime.

An ingredient to the lifetime measurement to which the result is highly sensitive is the description of the decay time acceptance. Hence it is verified that the discrepancy between the 2011 and 2012 results does not depend on the acceptances obtained from simulation. To check this hypothesis for the lower decay time acceptance, the function describing the acceptance in 2011 data is used with 2012 data and the other way around. The results of these fits are identical to the nominal fit results at the 3 fs level, which does not explain the difference.

For the upper decay time acceptance, the 2011 and 2012 samples are split once more according to the track types of the Λ daughters (LL or DD). Since the upper decay time acceptance strongly depends on the track type, the Λ_b^0 lifetime measurements based on these sub-samples show the dependence on the acceptance description. It appears that the fit results are consistent and do not show a systematic trend. Hence it can be concluded that the difference is not due to the description of the decay time acceptance.

In order to check whether the 2011 data suffer from a general systematic bias towards low lifetime values, the Ξ_b^- and Ω_b^- lifetimes are separately fitted in the data sets of 2011 and 2012. The results are shown in Table 4.10 and it appears that the trend of the Λ_b^0 is not confirmed. Further confidence is gained that the 2011 and 2012 discrepancy is indeed of statistical nature.

Overall, all measurements are consistent with each other and with other high precision measurements.

Table 4.10: Comparison, in ps, between Ξ_b^- and Ω_b^- lifetime measurements based on sub-samples of the data.

Measurement	τ	(stat)	(syst)	(tot)
Ξ_b^- lifetime	1.55	$+0.10 \atop -0.09$	± 0.03	± 0.10
- Only 2011 data (1.0 fb^{-1})	1.81	$+0.20 \atop -0.17$	$\pm 0.03^*$	± 0.19
- Only 2012 data (2.0 fb^{-1})	1.39	$+0.12 \atop -0.10$	$\pm 0.03^*$	± 0.11
Ω_b^- lifetime	1.54	$+0.26 \atop -0.21$	± 0.05	± 0.24
- Only 2011 data (1.0 fb^{-1})	1.23	$+0.39 \atop -0.28$	$\pm 0.05^*$	± 0.34
- Only 2012 data (2.0 fb^{-1})	1.68	$+0.35 \atop -0.27$	$\pm 0.05^*$	± 0.31

* The systematic uncertainties on the sub-sample results are naively taken from the total result.

4.10 Results

The lifetimes of the Ξ_b^- and Ω_b^- baryons are measured to be

$$\tau(\Xi_b^-) = 1.55^{+0.10}_{-0.09} \text{ (stat)} \pm 0.03 \text{ (syst) ps,}$$

$$\tau(\Omega_b^-) = 1.54^{+0.26}_{-0.21} \text{ (stat)} \pm 0.05 \text{ (syst) ps.}$$

These are the most precise measurements of these quantities to date. As shown in Table 4.11, both results are in good agreement with the other measurements available from CDF. The measured lifetimes also agree with the theoretical predictions summarized in Table 1.4 except the one presented in Ref. [27]. However this particular prediction suffers from a strong bias towards low lifetime values due to the general effort at this time to accommodate for the unexpectedly low value of the measured Λ_b^0 lifetime. Since the results are still dominated by the statistical uncertainty, more precise measurements will be easy to perform with the data from the second run of the LHC.

Table 4.11: Comparison between the Ξ_b^- and Ω_b^- lifetime measurements from CDF and the ones presented in this thesis. The quoted errors include statistical and systematic uncertainties. All values are given in ps.

Measurement	$\tau(\Xi_b^-)$	$\tau(\Omega_b^-)$
CDF published [7]	1.56 ± 0.26	1.13 ± 0.47
CDF preliminary [42, 43]	1.36 ± 0.15	1.77 ± 0.48
LHCb (this thesis)	1.55 ± 0.10	1.54 ± 0.24

5 Conclusions and outlook

The LHCb experiment at the Large Hadron Collider at CERN was designed to study CP-violation and the c- and b-quark sectors. It recorded its first data from pp collisions in December 2009 at a centre-of-mass energy equal to the LHC injection energy of 450 GeV. During the years 2010 and 2011 it has collected data at a centre-of-mass energy of $\sqrt{s} = 7$ TeV corresponding to a total integrated luminosity of 36 pb^{-1} in 2010 and 1.0 fb^{-1} in 2011. For the run of 2012, the centre-of-mass energy was increased to $\sqrt{s} = 8$ TeV and pp collisions corresponding to a total integrated luminosity of 2.0 fb^{-1} were recorded.

Several software alignments of the tracking stations using $D^0 \to K^- \pi^+$ vertex and mass constraints are performed with the data recorded in 2010. It has been shown that this technique is robust and permits to tackle some problems related to weak modes. The Inner Tracker and Tracker Turicensis detector positions are determined with an average precision of 15 μm. In addition an issue due to different Tracker Turicensis operating temperatures that led to physical movements of the detector is successfully addressed. Solving this problem is crucial to several analyses at LHCb that rely on high precision momentum measurements. The alignments of the detector with data recorded in 2011 and 2012 are cross-checked and their understanding improved. The data of the second run of the LHC is soon to come and the LHCb detector will be aligned with the procedure described here, including vertex and mass constraints.

Very little is known about the baryons containing a b quark. The physics analysis part of this thesis is dedicated to the study and measurement of basic properties of the lightest weakly-decaying b baryons, called Λ_b^0, Ξ_b^-, Ξ_b^0 and Ω_b^- and which contain the dub, dsb, usb and ssb quark combinations respectively.

Using the data recorded in 2011, the masses of the Λ_b^0, Ξ_b^- and Ω_b^- baryons are measured. These measurements are the most precise to date. They are in agreement with the world averages with the exception of the measured Ω_b^- mass which is in agreement with the CDF measurement but not in agreement with the D0 measurement. Since the uncertainties on the Ξ_b^- and Ω_b^- mass measurements are dominated by the statistical contribution, a significant

improvement can be expected from an analysis that would combine both the 2011 and 2012 data.

The Ξ_b^0 baryon is observed in the $\Xi_b^0 \to J/\psi\, \Xi^- \pi^+$ decay mode using the complete data set recorded at LHCb. If this analysis is continued, it can not only lead to a publication of the first observation of this decay channel but also to the most precise determination of the Ξ_b^0 mass to date.

The currently most precise determinations of the Ξ_b^- and Ω_b^- lifetimes are performed using the data recorded in 2011 and 2012 at LHCb. The results are in agreement with the previous measurements from CDF and with most of the few available theoretical predictions. More statistics would not only help improving the statistical uncertainty of the results but also allow a different strategy leading to reduced systematic uncertainties. Therefore a large improvement of these measurements is expected when the data of the second run of the LHC will be analysed.

Theoretical predictions of the quantities measured in this thesis are unprecise yet. Therefore the results presented here provide a unique and valuable input for quantum chromodynamics calculations in the low energy regime. More data at a higher centre-of-mass energy will allow the LHCb experiment to push even further the b-baryon studies. In particular, they will allow a more precise spectroscopy of the qqb systems (where $q = u, d, s$) and might open the door for the first observation of a doubly heavy baryon like the Ξ_{bc}^+ or Ξ_{bc}^0.

A Upper decay time acceptance - step definitions

The steps of progressive reconstruction and stripping used in the study of the upper decay time acceptance in Figs. 4.3–4.6 are defined as follows:

1. No requirement

2. Muons have VELO hits

3. Bachelor has VELO hits (LLL, LDD) or no requirement (DDD) or no requirement (Λ_b^0)

4. Λ daughters have VELO hits (LL, LLL) or no requirement (DD, LDD, DDD)

5. Muons reconstructible as long tracks

6. Bachelor reconstructible as long (LLL, LDD) or downstream (DDD) track or no requirement (Λ_b^0)

7. Λ daughters reconstructible as long (LL, LLL) or downstream (DD, LDD, DDD) tracks

8. Muons reconstructed as long tracks

9. Bachelor reconstructed as long (LLL, LDD) or downstream (DDD) track or no requirement (Λ_b^0)

10. Λ daughters reconstructed as long (LL, LLL) or downstream (DD, LDD, DDD) tracks

11. Full candidate is reconstructed and selected by the stripping

The steps of progressive offline selection are:

12. All track clone distances > 5000 and no track key duplicate

13. Kaon PIDK > 5 (Ω_b^-) or no requirement (Λ_b^0, Ξ_b^-)

14. J/ψ vertex $\chi^2/\mathrm{ndf} < 16$

15. Hyperon vertex $\chi^2/\mathrm{ndf} < 16$

16. J/ψ mass within ± 60 MeV/c^2 window

17. Ξ^- or Ω^- mass within ± 11 MeV/c^2 window or no requirement (Λ_b^0)

18. Λ mass within ± 6 MeV/c^2 window and (for Λ_b^0 only) Λ DLS > 3

19. DTF $\chi^2/\mathrm{ndf} < 4$

20. b-baryon IP $\chi^2 < 25$

21. L0 triggered

22. Unbiased HLT1 triggered

23. Unbiased HLT2 triggered

Bibliography

[1] Particle Data Group, J. Beringer *et al.*, *Review of particle physics*, Phys. Rev. **D86** (2012) 010001 and 2013 partial update for the 2014 edition.

[2] CDF collaboration, F. Abe *et al.*, *Observation of $\Lambda_b^0 \to J/\psi\,\Lambda$ at the Fermilab proton antiproton collider*, Phys. Rev. **D55** (1997) 1142.

[3] CDF collaboration, D. Acosta *et al.*, *Measurement of b hadron masses in exclusive J/ψ decays with the CDF detector*, Phys. Rev. Lett. **96** (2006) 202001, `arXiv:hep-ex/0508022`.

[4] LHCb collaboration, R. Aaij *et al.*, *Measurement of b-hadron masses*, Phys. Lett. **B708** (2012) 241, `arXiv:1112.4896`.

[5] ATLAS collaboration, G. Aad *et al.*, *Measurement of the Λ_b^0 lifetime and mass in the ATLAS experiment*, Phys. Rev. **D87** (2013) 032002, `arXiv:1207.2284`.

[6] D0 collaboration, V. Abazov *et al.*, *Direct observation of the strange b baryon Ξ_b^-*, Phys. Rev. Lett. **99** (2007) 052001, `arXiv:0706.1690`.

[7] CDF collaboration, T. Aaltonen *et al.*, *Observation of the Ω_b^- baryon and measurement of the properties of the Ξ_b^- and Ω_b^- baryons*, Phys. Rev. **D80** (2009) 072003, `arXiv:0905.3123`.

[8] CDF collaboration, T. Aaltonen *et al.*, *Observation of the Ξ_b^0 baryon*, Phys. Rev. Lett. **107** (2011) 102001, `arXiv:1107.4015`.

[9] D0 collaboration, V. Abazov *et al.*, *Observation of the doubly strange b baryon Ω_b^-*, Phys. Rev. Lett. **101** (2008) 232002, `arXiv:0808.4142`.

[10] M. Needham, *Clone track identification using the Kullback-Liebler distance*, LHCb-2008-002.

[11] S. Glashow, *Partial-symmetries of weak interactions*, Nucl. Phys. **22 (4)** (1961) 579.

[12] S. Weinberg, *A model of leptons*, Phys. Rev. Lett. **19 (21)** (1967) 1264.

[13] A. Salam, *Elementary particle physics: relativistic groups and analyticity*, proceedings of the 8th Nobel symposium (1968) 367.

Bibliography

[14] F. Englert and R. Brout, *Broken symmetry and the mass of gauge vector mesons*, Phys. Rev. Lett. **13 (9)** (1964) 321.

[15] P. Higgs, *Broken symmetries and the masses of gauge bosons*, Phys. Rev. Lett. **13 (16)** (1964) 508.

[16] G. Guralnik, C. Hagen, and T. Kibble, *Global conservation laws and massless p articles*, Phys. Rev. Lett. **13 (20)** (1964) 585.

[17] ATLAS collaboration, G. Aad *et al.*, *Observation of a new particle in the search for the Standard Model Higgs boson with the ATLAS detector at the LHC*, Phys. Lett. **B716** (2012) 1, arXiv:1207.7214.

[18] CMS collaboration, S. Chatrchyan *et al.*, *Observation of a new boson at a mass of 125 GeV with the CMS experiment at the LHC*, Phys. Lett. **B716** (2012) 30, arXiv:1207.7235.

[19] M. Karliner, B. Keren-Zur, H. Lipkin, and J. Rosner, *The quark model and b baryons*, Annals Phys. **342** (2009) 2, arXiv:0804.1575.

[20] E. E. Jenkins, *Model-independent bottom baryon mass predictions in the* $1/N_c$ *expansion*, Phys. Rev. **D77** (2008) 034012, arXiv:0712.0406.

[21] D. Ebert, R. Faustov, and V. Galkin, *Masses of heavy baryons in the relativistic quark model*, Phys. Rev. **D72** (2005) 034026, arXiv:hep-ph/0504112.

[22] J. P. Day, W. Plessas, and K.-S. Choi, *Universal constituent-quark model for baryons*, arXiv:1205.6918.

[23] X. Liu *et al.*, *Bottom baryons*, Phys. Rev. **D77** (2008) 014031, arXiv:0710.0123.

[24] J.-R. Zhang and M.-Q. Huang, *Heavy baryon spectroscopy in QCD*, Phys. Rev. **D78** (2008) 094015, arXiv:0811.3266.

[25] R. Lewis and R. Woloshyn, *Bottom baryons from a dynamical lattice QCD simulation*, Phys. Rev. **D79** (2009) 014502, arXiv:0806.4783.

[26] I. I. Bigi, *The QCD perspective on lifetimes of heavy-flavour hadrons*, arXiv:hep-ph/9508408.

[27] H.-Y. Cheng, *A phenomenological analysis of heavy hadron lifetimes*, Phys. Rev. **D56** (1997) 2783, arXiv:hep-ph/9704260.

[28] T. Ito, M. Matsuda, and Y. Matsui, *New possibility of solving the problem of lifetime ratio* $\tau(\Lambda_b^0)/\tau(B_d)$, Prog. Theor. Phys. **99** (1998) 271, arXiv:hep-ph/9705402.

[29] UA1 collaboration, C. Albajar *et al.*, *First observation of the beauty baryon* Λ_b^0 *in the decay channel* $\Lambda_b^0 \to J/\psi\,\Lambda$ *at the CERN proton-antiproton collider*, Phys. Lett. **B273** (1991) 540.

[30] ALEPH collaboration, D. Buskulic *et al.*, *Measurements of the b baryon lifetime*, Phys. Lett. **B357** (1995) 685.

[31] OPAL collaboration, R. Akers *et al.*, *A Measurement of the Lambda(b)0 lifetime*, Phys. Lett. **B353** (1995) 402.

[32] DELPHI collaboration, P. Abreu *et al.*, *Production of strange B baryons decaying into $\Xi^{\mp}$ - $l^{\mp}$ pairs at LEP*, Z. Phys. **C68** (1995) 541.

[33] ALEPH collaboration, D. Buskulic *et al.*, *Strange b baryon production and lifetime in Z decays*, Phys. Lett. **B384** (1996) 449.

[34] DELPHI collaboration, J. Abdallah *et al.*, *Production of Ξ_c^0 and Ξ_b in Z decays and lifetime measurement of Ξ_b*, Eur. Phys. J. **C44** (2005) 299, arXiv:0510023.

[35] CDF collaboration, T. Aaltonen *et al.*, *First observation of heavy baryons Σ_b and Σ_b^**, Phys. Rev. Lett. **99** (2007) 202001, arXiv:0706.3868.

[36] CDF collaboration, T. Aaltonen *et al.*, *Observation and mass measurement of the baryon Ξ_b^-*, Phys. Rev. Lett. **99** (2007) 052002, arXiv:0707.0589.

[37] CMS collaboration, S. Chatrchyan *et al.*, *Observation of a new Ξ_b baryon*, Phys. Rev. Lett. **108** (2012) 252002, arXiv:1204.5955.

[38] LHCb collaboration, R. Aaij *et al.*, *Observation of excited Λ baryons*, Phys. Rev. Lett. **109** (2012) 172003, arXiv:1205.3452.

[39] CDF collaboration, T. Aaltonen *et al.*, *Measurement of the masses and widths of the bottom baryons $\Sigma_b^{\pm}$ and $\Sigma_b^{*\pm}$*, Phys. Rev. **D85** (2012) 092011, arXiv:1112.2808.

[40] LHCb collaboration, R. Aaij *et al.*, *Measurements of the Λ_b^0, Ξ_b^- and Ω_b^- baryon masses*, Phys. Rev. Lett. **110** (2013) 182001, arXiv:1302.1072.

[41] LHCb collaboration, R. Aaij *et al.*, *Measurements of the B^+, B^0, B_s^0 meson and Λ_b^0 baryon lifetimes*, arXiv:1402.2554, to appear in JHEP.

[42] P. Lukens on behalf of the CDF collaboration, *Measurement of b-baryon properties at CDF*, talk at meeting of the American Physical Society (APS), Division of Particles and Fields (DPF), Santa Cruz, USA (Aug. 2013).

[43] CDF collaboration, *Measurement of the properties of the Λ_b^0, Ξ_b^0, Ξ_b^-, and Ω_b^-*, public CDF note 11024 (Dec. 2013).

[44] LHCb collaboration, A. A. Alves Jr. *et al.*, *The LHCb detector at the LHC*, JINST **3** (2008) S08005.

[45] LHCb collaboration, P. R. Barbosa Marinho *et al.*, *LHCb VELO (VErtex LOcator) : Technical Design Report*, CERN-LHCC-2001-011.

[46] LHCb collaboration, R. Antunes Nobrega *et al.*, *LHCb reoptimized detector design and performance : Technical Design Report*, CERN-LHCC-2003-030.

[47] LHCb collaboration, A. Franca Barbosa *et al.*, *LHCb inner tracker : Technical Design Report*, CERN-LHCC-2002-029.

[48] LHCb collaboration, P. R. Barbosa Marinho *et al.*, *LHCb outer tracker : Technical Design Report*, CERN-LHCC-2001-024.

[49] LHCb collaboration, S. Amato *et al.*, *LHCb calorimeters : Technical Design Report*, CERN-LHCC-2000-036.

[50] LHCb collaboration, R. Antunes Nobrega *et al.*, *LHCb trigger system : Technical Design Report*, CERN-LHCC-2003-031.

[51] LHCb collaboration, R. Aaij *et al.*, *Prompt K_S^0 production in pp collisions at $\sqrt{s} = 0.9$ TeV*, Phys. Lett. **B693** (2010) 69, `arXiv:1008.3105`.

[52] M. Clemencic *et al.*, *The LHCb simulation application,* GAUSS*: design, evolution and experience*, J. Phys. Conf. Ser. **331** (2011) 032023.

[53] T. Sjöstrand, S. Mrenna, and P. Skands, *PYTHIA 6.4 physics and manual*, JHEP **05** (2006) 026, `arXiv:hep-ph/0603175`.

[54] D. J. Lange, *The EvtGen particle decay simulation package*, Nucl. Instrum. Meth. **A462** (2001) 152.

[55] Geant4 collaboration, S. Agostinelli *et al.*, *Geant4: a simulation toolkit*, Nucl. Instrum. Meth. **A506** (2003) 250.

[56] Geant4 collaboration, J. Allison *et al.*, *Geant4 developments and applications*, IEEE Trans. Nucl. Sci. **53** (2006) 270.

[57] R. Märki, *Alignment of the LHCb tracking system*, 13th ICATPP Conference on Astroparticle, Particle, Space Physics and Detectors for Physics Applications, Como, Italy (Oct. 2011), LHCb-TALK-2011-255.

[58] R. Märki, *Alignment of the LHCb tracking system*, Astroparticle, Particle, Space Physics and Detectors for Physics Applications **Vol. 7** (2012) 611.

[59] R. Märki, *Heavy flavour spectroscopy at LHCb*, 36th International Conference for High Energy Physics, Melbourne, Australia (July 2012), LHCb-TALK-2012-217.

[60] R. Märki, *Heavy flavour spectroscopy at LHCb*, Proceedings of Science **ICHEP2012** (2012) 252.

[61] R. Märki, *b-baryon mass measurements at LHCb*, Les Rencontres de Physique de la Vallée d'Aoste, La Thuile, Italy (Feb. 2013), LHCb-TALK-2013-037.

[62] R. Märki, *b-baryon mass measurements at LHCb*, Il Nuovo Cimento C **2013-6** (2013) 154.

[63] R. Märki, *b-hadron production and spectroscopy at LHCb*, Windows on the Universe - Rencontres du Vietnam, Quy Nhon, Vietnam (Aug. 2013), LHCb-TALK-2013-231.

[64] R. Märki, *b-hadron production and spectroscopy at LHCb*, LHCb-PROC-2013-053.

[65] R. Märki, *Λ reconstruction and selection efficiency study at LHCb*, Master's thesis, Jan. 2010, http://lphe.epfl.ch/publications/theses-en.php#mast.

[66] M. Knecht, *Commissioning of the LHCb Inner Tracker and measurement of V^0-particle production in pp collisions at* 0.9 TeV, PhD thesis, EPFL thesis n° 5044, Lausanne, Switzerland, July 2011, CERN-THESIS-2011-053.

[67] LHCb collaboration, R. Aaij *et al.*, *Observation of X(3872) production in pp collisions at $\sqrt{s} = 7$ TeV*, Eur. Phys. J. **C72** (2011) 1972, `arXiv:1112.5310`.

[68] J. Amoraal *et al.*, *Application of vertex and mass constraints in track-based alignment*, Nucl. Instrum. Meth. **A712** (2013) 48, `arXiv:1207.4756`.

[69] LHCb collaboration, R. Aaij *et al.*, *Measurement of the Ξ_b^- and Ω_b^- baryon lifetimes*, LHCb-PAPER-2014-010, in preparation.

[70] W. Hulsbergen, *The global covariance matrix of tracks fitted with a Kalman filter and an application in detector alignment*, Nucl. Instrum. Meth. **A600** (2009) 471–477, `arXiv:0810.2241`.

[71] S. Borghi *et al.*, *First spatial alignment of the LHCb VELO and analysis of beam absorber collision data*, Nucl. Instrum. Meth. **A618** (2010) 108.

[72] V. Fave, *Contribution to the alignment of the LHCb tracking system and measurement of the mean lifetimes of $B_{d(s)} \to D_{(s)}\pi$, $D_{(s)} \to KK\pi$*, PhD thesis, EPFL thesis n° 5257, Lausanne, Switzerland, June 2012, CERN-THESIS-2012-160.

[73] F. Dupertuis, *A novel alignment procedure and results for the LHCb Silicon Trcker*, Nuclear Science Symposium and Medical Imaging Conference (NSS/MIC) **2011 IEEE** (2011) 1314.

[74] E. E. Simioni, *New physics from rare beauty*, PhD thesis, Vrije Universiteit, Amsterdam, The Netherlands, 2010, CERN-THESIS-2010-031.

[75] M. Needham, *Momentum scale calibration using resonances*, LHCb-2008-037.

[76] W. D. Hulsbergen, *Decay chain fitting with a Kalman filter*, Nucl. Instrum. Meth. **A552** (2005) 566, `arXiv:physics/0503191`.

[77] LHCb collaboration, *Measurement of the masses of the Ξ_b^- and Ω_b^-*, LHCb-CONF-2011-060.

[78] E. Gross and O. Vitells, *Trial factors for the look elsewhere effect in high energy physics*, Eur. Phys. J. **C70** (2010) 525, arXiv:1005.1891.

[79] LHCb collaboration, R. Aaij *et al.*, *Measurement of the $B_s^0 - \bar{B}_s^0$ oscillation frequency Δm_s in $B_s^0 \to D_s^-(3)\pi$ decays*, Phys. Lett. **B709** (2012) 177, arXiv:1112.4311.

[80] T. Skwarnicki, *A study of the radiative cascade transitions between the Upsilon-prime and Upsilon resonances*, PhD thesis, Institute of Nuclear Physics, Krakow, 1986, DESY-F31-86-02.

[81] ARGUS collaboration, H. Albrecht *et al.*, *Search for hadronic $b \to u$ decays*, Phys. Lett. **B241** (1990) 278.

[82] LHCb collaboration, R. Aaij *et al.*, *Measurement of CP-violation and the B_s^0-meson decay width difference with $B_s^0 \to J/\psi K^+ K^-$ and $B_s^0 \to J/\psi \pi^+ \pi^-$ decays*, Phys. Rev. **D87** (2013) 112010, arXiv:1304.2600.

[83] F. James and M. Roos, *Minuit: A System for Function Minimization and Analysis of the Parameter Errors and Correlations*, Comput. Phys. Commun. **10** (1975) 343.

[84] F. James, *MINUIT: Function Minimization and Error Analysis: Reference Manual*, http://wwwasdoc.web.cern.ch/wwwasdoc/minuit/minmain.html.

[85] ALEPH collaboration, R. Barate *et al.*, *Measurement of the b baryon lifetime and branching fractions in Z decays*, Eur. Phys. J. **C2** (1998) 197.

[86] DELPHI collaboration, P. Abreu *et al.*, *Measurement of the lifetime of b baryons*, Eur. Phys. J. **C10** (1999) 185.

[87] OPAL collaboration, K. Ackerstaff *et al.*, *Measurements of the B_s^0 and Λ_b^0 lifetimes*, Phys. Lett. **B426** (1998) 161, arXiv:hep-ex/9802002.

[88] CDF collaboration, F. Abe *et al.*, *Measurement of Λ_b^0 lifetime using $\Lambda_b^0 \to \Lambda_c^+ l^- \bar{\nu}$*, Phys. Rev. Lett. **77** (1996) 1439.

[89] CDF collaboration, T. Aaltonen *et al.*, *Measurement of the Λ_b^0 lifetime in $\Lambda_b^0 \to \Lambda_c^+ \pi^-$ decays in $p\bar{p}$ collisions at $\sqrt{s} = 1.96$ TeV*, Phys. Rev. Lett. **104** (2010) 102002, arXiv:0912.3566.

[90] CDF collaboration, T. Aaltonen *et al.*, *Measurement of b hadron lifetimes in exclusive decays containing a J/ψ in $p - \bar{p}$ collisions at $\sqrt{s} = 1.96$ TeV*, Phys. Rev. Lett. **106** (2011) 121804, arXiv:1012.3138.

[91] D0 collaboration, V. M. Abazov *et al.*, *Measurement of the Λ_b^0 lifetime using semileptonic decays*, Phys. Rev. Lett. **99** (2007) 182001, arXiv:0706.2358.

[92] D0 collaboration, V. M. Abazov *et al.*, *Measurement of the Λ_b^0 lifetime in the exclusive decay $\Lambda_b^0 \to J/\psi \Lambda$ in $p\bar{p}$ collisions at $\sqrt{s} = 1.96$ TeV*, Phys. Rev. **D85** (2012) 112003, arXiv:1204.2340.

[93] CMS collaboration, S. Chatrchyan *et al.*, *Measurement of the Λ_b^0 lifetime in pp collisions at $\sqrt{s}$ = 7 TeV*, JHEP **07** (2013) 163, `arXiv:1304.7495`.

[94] LHCb collaboration, R. Aaij *et al.*, *Precision measurement of the Λ_b^0 baryon lifetime*, Phys. Rev. Lett. **111** (2013) 102003, `arXiv:1307.2476`.

[95] LHCb collaboration, R. Aaij *et al.*, *Precision measurement of the ratio of the Λ_b^0 to $\bar{B}^0$ lifetimes*, `arXiv:1402.6242`, submitted to Phys. Lett. B.

CURRICULUM VITAE

« leadership, creativity, synthesis »

PERSONAL INFORMATION

Last name :	Märki
First name :	Raphael
Address :	Av. de la Rapille 14
	1008 Prilly
Mobile phone :	+41 78 822 21 38
E-mail address :	raphael.marki@epfl.ch
Marital status :	single
Nationality :	Swiss
Date of birth:	24 June 1986
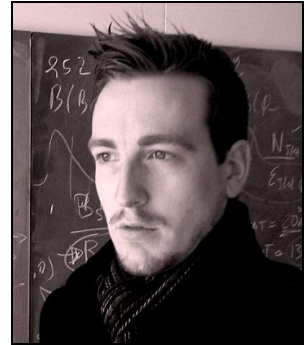
EDUCATION

- 2010-2014 : EPFL; PhD in particle physics on the LHCb experiment at CERN
  « Measurements of *b*-baryon properties at LHCb »
- 2005-2010 : EPFL; Master in physics with specialisation in particle physics
- 2002-2005 : Gymnasium; Maturity with specialisation in « physics and mathematics »
- 1999-2002 : Secundary school; specialisation in « physics and mathematics »
- 1992-1996 : Primary school in Lüdenscheid (Germany)

WORK EXPERIENCE

- 06/2006-12/2009 Fraud assistant at Orange Communications SA at 25 % + supply working (intern and extern, technical and economical fraud detection)
- 09/2008-12/2009 Teaching (C++ programming course and practical works in physics)
- 08/2004-06/2006 Vendor at the Shell gas station in Cheseaux at 30 %
- 06/2002-08/2004 Regular work at Emil Frey SA (IT department)
- 04/2003-06/2004 Teacher for extra lessons to students of age between 10 and 16
- 07/2001-05/2004 Webdesign for small businesses in collaboration with « Administration et Marketing pour Indépendants Services », Yverdon at approximately 10 %
- Summer 2001, 2003 and 2004 Temporary work at Vulliamy SA (2001) and at Editions Atlas (2003 and 2004)

INTERESTS & HOBBIES

- Sports (running, fitness, roller skating, skateboarding), reading, computers, piano

SKILLS

- ***Languages***

  - french and german : mother tongues
  - english : good (IELTS 7.5)
  - spanish : basic knowledge; courses (3 years) and language stay (1 month)

- ***Computer skills***

  - Databases : Access, SQL
  - Programming : C++, Python, Java, Javascript, PHP/MySQL, Bash/Csh
  - Data mining, optimisation, multivariate analysis, IT security and fraud, webdesign

REFERENCES

- M. Ali Benkirane, Director of R. A. and Fraud at Orange Communications SA, +41 78 787 50 65
- M. Daniele Mensi, Fraud Manager at Orange Communications SA, +41 78 787 12 42
- Prof. Olivier Schneider, Full Professor at the LPHE from EPFL, +41 21 693 05 07
- Summary of scientific publications on http://lphe.epfl.ch/rmaerki